Transport of cold atoms in laser fields

Nihal AbdulWahhab

A thesis submitted to the University College London
in partial fulfilment of the requirements for the
degree of Doctor of Philosophy

Department of Physics and Astronomy
University College London
January 2015

Nihal AbdulWahhab

13.01.2015

I, Nihal AbdulWahhab, confirm that the work presented in this thesis is my own. Where information has been derived from other sources, I confirm that this has been indicated in the thesis.

Signed ..... Date.....

Abstract

This thesis describes three experiments with cold rubidium atoms; two experiments explore the so-called ratchet effect while the third investigates the formation and characterisation of a Bose-Einstein condensate. Brownian motors, or ratchets, are devices that rectify fluctuations and generate directed current. Since the second law of thermodynamics states that one cannot extract useful work out of a single thermal bath at equilibrium, ratchets are implemented with cold ^{87}Rb atoms in a 1D $lin \perp lin$ dissipative optical lattice in the presence of an oscillating force which drives the system out of equilibrium.

The first experiment investigates current reversals in a rocking ratchet as observed by varying the driving frequency. As a result of this study, it is found that this kind of current reversal in the frequency domain is determined by dissipation-induced symmetry breaking. This is in agreement with theoretical studies.

The second experiment focuses on the vibrational resonance phenomenon, which is demonstrated experimentally for a system of cold atoms in an optical lattice. In this experiment a high frequency strong driving field was applied in order to renormalise the optical potential. This occurs when the driving frequency is much larger than any characteristic frequency of the system. It was observed that the amplitude of the renormalised potential can be controlled by the high frequency driving field. The renormalisation process was probed by two different methods: by studying the diffusion properties and via the observation of the directed transport. In the first scheme, the renormalisation can be detected by observing the inverse mutual relation between the diffusion exponent and the optical potential depth. In the second scheme, the directed transport is used to probe the potential renormalisation by showing that the atomic velocity can be controlled with a high frequency driving field.

Finally, the third part of this work describes the realisation and characterisation of a Bose-Einstein condensate of rubidium atoms. The associated work included the upgrade of the diode laser system into a MOPA system

with higher power, and setting up and characterising the magnetic trap in which evaporation was performed.

To my family

Acknowledgements

The work presented in this thesis could not have been completed without the guidence, encouragement and support of faculty, friends and family. I take this opportunity to express my deepest appreciation to all people who provided me the possibilty to complete this thesis.
First and foremost I would like to acknowledge with much appreciation my supervisor Prof. Ferruccio Renzoni for supporting and guiding me during these past four years. I also want to thank him for providing me with the opportunity to work within his group. Second, I give a special thank you to Dr. Arne Wickenbrock for helping me with the experiment throughout my PhD. Then I would like to thank the other members of the group who helped me out in one way or the other: Lyubomir Petrov who unfortunately passed away recently, Piyaphat Phoonthong (Boeing), Mukaddes Meliz Metbulut, Philip Christoph Holz, Cosimo Lovecchio, Michal Hemmerling, Soliman Edris, and Yuri Ovchinnikov.
I would like to thank the people working in the physics department workshop. I thank Rafid Jawad who helped to build and fix the electronics of the experiment. Also, I want to say thank you to John Dumper for building all the mechanical parts.
I like to thank the Iraqi government and Babylon University for providing me with a scholarship.
I would like to thank my brother Emad Abdul Wahab for his unlimited help and support. Also, big thanks to my parents for their encouragement and prayers. Finally, I would like to deeply thank my husband Hassanian Almamoori for his endless support and encouragement without which I could not have finished my PhD studies. And all my love goes to my children Ahmed and Yousif.

Contents

List of Abbreviations

AOM	Acousto-Optical Modulator
BEC	Bose-Einstein Condensate
BH	Bi-Harmonic
CCD	Charge-Coupled Device
DF-DAVLL	Doppler Free Dichroic Atomic Vapour Laser Lock
DHP	Divided High Power heatsink
ECDL	External Cavity Diode Lasers
EOM	Electro-Optical Modulator
HF	High Frequency
HWP	Half Wave Plate
LVIS	Low Velocity Intense Source of atoms
MOPA	Master Oscillator Power Amplifier
MOSFET	Metal Oxide Semiconductor Field-Effect Transistor
MOT	Magneto-Optical Trap
NEG	Non-Evaporable Getter
NPBS	Non-Polarising Beam Splitter
OBE	Optical Bloch Equations
PBS	Polarising Beam Splitter

PSD	Phase Space Density
QUAD	Quadrupole magnetic field
QUIC	Quadrupole-Ioffe Configuration
QWP	Quarter Wave Plate
RF	Radio Frequency
TA	Tapered Amplifier
TEM_{00}	Transverse Electro Magnetic of the Gaussian Mode
TOF	Time Of Flight
UHV	Ultra-High Vacuum

List of Figures

Chapter 1

Introduction

Laser cooling and trapping has revolutionised the atomic physics field. Many techniques can be used to cool the atoms and achieve low temperatures such as sub-Doppler laser cooling [15] and evaporative cooling which is the last stage before producing a Bose-Einstein Condensate (BEC). A brief overview of the underlying principles for the relevant topics to the work of this thesis is presented in this chapter.

1.1 Laser cooling and trapping

1.1.1 Historical overview

In the nineteenth century, Maxwell introduced the idea that radiation has a momentum [62], and it was demonstrated experimentally in 1901 by Lebedev [50]. In addition to this, a study performed by Nichols and Hull in 1901 and 1903 [70], presented a quantitative measurement of the radiation force on the microscopic particles. After the advent of the laser in 1972, the first experiment in deflecting an atomic beam using laser radiation was conducted by Picqué and Vialle [79, 89]. After the scattering force resulting from the scattering of light when it strikes the atoms was presented by Ashkin, the dipole force, which is attributed to the interaction between the light and the dipole moment of the atoms, was recognized by Askar'yan [76].

The idea behind laser cooling and trapping was introduced in 1975 by Hänsch and Schawlow [36], who demonstrated that the Doppler effect provides a velocity dependent force when illuminating neutral atoms with

laser radiation. The first laser cooling experiments were executed on ions trapped by electric fields. The first laser experiment was reported in 1978 by Wineland, Drullinger and Walls on the cooling of Mg ions [100]. In the same year, another group published their work on laser cooling of trapped Ba^+ ions [69]. Later, the first demonstration of Doppler cooling in three dimensions to obtain very cold atoms was published by Chu et al. in 1985 [13]. That work introduced the so-called optical molasses which cools but does not trap the atoms. This paved the way to develop the so-called Magneto-Optical Trap (MOT) which was reported in 1987 by Raab et al. [81]. Nowadays, the magneto-optical trap is considered as the backbone in most cooling and trapping experiments. Another important cooling process is the so-called Sisyphus cooling [15, 41]. Optical molasses were shown to produce even lower temperatures than Doppler cooling. The considerable progress achieved in the field of laser cooling and trapping generated a Nobel prize in physics in 1997 to Chu, Cohen- Tannoudji and Phillips [24]. Despite the rapid advance of laser cooling, there were still some limitations to achieve higher density due to the recoil limit and heating and trap loss as a result of the collisions of the excited state. In 1995, evaporative cooling was shown to overcome all of these problems by cooling the atoms further and leading to a change in the matter phase resulting in Bose-Einstein Condensation [16].

1.1.2 Fundamental aspects

Laser cooling and trapping of atoms relies on the interaction between the laser radiation and the atoms. The force exerted on the atoms by the laser radiation can be divided into two components: the radiation pressure force, or dissipative force, which is based on the scattering of light by the atoms causing the slowing and then cooling of the atoms. The second component is the dipole force, or the gradient force, which is proportional to the field gradient.

An atom experiences a kick in the opposite direction of its motion due to each absorbed photon. The photons are then spontaneously emitted in random directions. Therefore, scattering many photons produces an average force causing slowing of the atomic motion. To formally describe the mechanisms involved, it is required to consider a two level atom with

ground and excited states $|1\rangle$ and $|2\rangle$ respectively, coupled with laser radiation of frequency ω and natural linewidth $\Gamma = \frac{1}{\tau}$ where τ is the lifetime of the excited state. The scattering rate for an atom can be calculated from the Optical Bloch equations (OBE) [24, 65]:

$$\begin{aligned} \dot{u} =& \Delta v - \frac{\Gamma}{2}u, \\ \dot{v} =& -\Delta u + \Omega w - \frac{\Gamma}{2}v, \\ \dot{w} =& -\Omega v - \Gamma(w-1), \end{aligned} \tag{1.1}$$

where u and v are the real and imaginary parts of the coherence ρ_{12}, w is the population inversion between the ground and the excited states, Δ is the frequency detuning from resonance such that $\Delta = \omega - \omega_0$, where ω_0 is the atomic frequency and Ω is the Rabi frequency, the oscillation frequency between the ground state and the excited state of a two-level atom interacting with a resonant light field. The Rabi frequency is related to the saturation intensity by the saturation parameter, which indicates the probability of finding an atom in the excited state:

$$s = \frac{\Omega^2/2}{\Delta^2 + \Gamma^2/4}. \tag{1.2}$$

At resonance ($\Delta = 0$), it turns to on-resonance saturation parameter:

$$s_0 = \frac{I}{I_s} = \frac{2\Omega^2}{\Gamma^2}, \tag{1.3}$$

where I and I_s are the laser intensity and the saturation intensity respectively. The optical Bloch equations describe the interaction between a two-level atom and radiation which is at near resonance to the atomic transition. For steady state, equations 1.1 are set to zero and solved simultaneously. Therefore, another set of equations are obtained:

$$\begin{aligned} u =& \frac{2\Delta}{\Gamma}v, \\ v =& \frac{2}{\Gamma}(\Omega w - u), \\ w =& \frac{\Omega}{\Gamma}v + 1. \end{aligned} \tag{1.4}$$

From equations 1.4, the population inversion is given as:

$$w = \frac{\Delta^2 + \Gamma^2/4}{\Delta^2 + \Omega^2/2 + \Gamma^2/4}, \tag{1.5}$$

and the steady state population of the excited state is $\rho_{22} = \frac{1-w}{2}$, therefore:

$$\rho_{22} = \frac{\Omega^2/4}{\Delta^2 + \Omega^2/2 + \Gamma^2/4}. \tag{1.6}$$

The scattering rate for an atom is given as $R_{scatt} = \Gamma\rho_{22}$, by substituting ρ_{22} from equation 1.6, we obtain the following:

$$R_{scatt} = \frac{\Gamma}{2}\frac{\Omega^2/2}{\Delta^2 + \Omega^2/2 + \Gamma^2/4}. \tag{1.7}$$

The scattering force is the rate of the transferred momentum and is given as $F_{scatt} = \hbar k R_{scatt}$, when $\hbar$ is the reduced Planck constant and k is the wave vector. Therefore:

$$F_{scatt} = \hbar k\frac{\Gamma}{2}\frac{s_0}{1 + s_0 + 4\Delta^2/\Gamma^2}. \tag{1.8}$$

At high intensity, the scattering force saturates at $\hbar k\Gamma/2$ owing to the fact that the population in both the ground and excited states becomes 1/2. Therefore, the maximum acceleration that is produced due to the scattering force is:

$$a_{max} = \frac{\upsilon_r\Gamma}{2}, \tag{1.9}$$

where υ_r is called the recoil velocity which is the atom's velocity change due to the photon absorption or emission. For sodium atoms the maximum acceleration is $9 \times 10^5\,\mathrm{m/s^2}$, which is 10^5 times the gravitational acceleration. For ^{87}Rb atoms, the maximum acceleration from equation 1.9 has a value of ≈ 1800 times the gravitational acceleration. In order to cool the atoms, two counter-propagating laser beams with red-detuned frequency from the atomic resonance ($\Delta = \omega - \omega_0 < 0$) and same intensity are required. Applying this in three dimensions, six counter-propagating laser beams are required producing a viscous force called optical molasses [71]. The minimum cooling limit is reached in this method because of a stochastic mechanism resulting from the photon absorption and spontaneous emission. This causes a random walk due

to the momentum kicks, which heats the atoms and limits the cooling temperature to the value [24]:

$$T_D = \frac{\hbar\Gamma}{2k_B}, \tag{1.10}$$

where k_B is the Boltzmann constant. So, the Doppler temperature limit depends only on the excited state linewidth which for ^{87}Rb is $\Gamma = (2\pi)6.066\,\mathrm{MHz}$. This limits the temperature to $145.57\,\mu\mathrm{K}$, while for sodium it is $240\,\mu\mathrm{K}$.

1.1.3 Optical molasses

In order to cool atoms moving in a vapour, a three dimensional configuration of counter-propagating laser beams with the same red detuning from the atomic transition ($\Delta < 0$) is required. This arrangement does not have any effect on stationary atoms as the opposing radiation forces cancel. However, an imbalance in the radiation force due to the Doppler effect is produced for moving atoms. For an atom moving in the opposite direction to the laser beam, the Doppler effect shifts the light frequency (with frequency detuning of $\Delta = \omega - \omega_0$) close to resonance with the atomic frequency, causing an increase in the absorption rate. The resultant force slows the atomic velocity, similarly so if the beam comes from any direction. The difference of the force applied from right and left can be expressed mathematically as:

$$F_{molasses} = F_{scatt}(\omega - \omega_0 - k\upsilon) - F_{scatt}(\omega - \omega_0 + k\upsilon), \tag{1.11}$$

where $F_{scatt}(\omega-\omega_0-k\upsilon)$ is the force exerted by the beam which is moving towards the atom with $-k$ wave vector. Whereas, $F_{scatt}(\omega - \omega_0 + k\upsilon)$ is the force on the atoms from the beam moving in the same direction with wave vector $+k$. υ is the atom velocity. By expanding in Taylor series:

$$\begin{aligned} F_{molasses} = &\left[F_{scatt}(\omega - \omega_0) + \frac{\partial F}{\partial \omega}(\omega - \omega_0 - k\upsilon)\right] \\ &- \left[F_{scatt}(\omega - \omega_0 + \frac{\partial F}{\partial \omega}(\omega - \omega_0 + k\upsilon)\right]. \end{aligned}$$

Then:

$$F_{molasses} \approx -2\frac{\partial F_{scatt}}{\partial \omega} kv. \tag{1.12}$$

The equation 1.12 becomes:

$$F_{molasses} = -\alpha v, \tag{1.13}$$

where $\alpha = 2\frac{\partial F_{scatt}}{\partial \omega}$ is the damping coefficient as a result of the damping force which is exerted on the atom by the laser radiation. This behaviour led to the name *Optical molasses* being coined for this mechanism [13].

1.1.4 Magneto-optical trap (MOT)

The Magneto-Optical Trap is the most common technique used to trap neutral atoms since 1987 when it was introduced [81]. It is used frequently to cool the atomic gas from room temperature down to the order of micro kelvins. Optical molasses alone provides cooling without trapping since it is only a velocity dependent force. Therefore, to implement the trapping, it is required to apply a position dependent force in order to confine the atoms. In a MOT, a quadrupole magnetic field needs to be applied to produce a position dependent force. This can be implemented by using two magnetic coils with opposite current directions to produce a quadrupole magnetic field which causes an imbalance in the scattering force applied by the laser beams. Figure 1.1 illustrates the principle of the MOT for the simple atomic transition $F = 0 \rightarrow F' = 1$. The magnetic field perturbs the atomic excited level by the Zeeman effect and lifts the degeneracy of atomic Zeeman sublevels. This perturbation does not occur for the ground state because its angular momentum is zero. As shown in the left picture of figure 1.1, the atoms are illuminated by two counter-propagating laser beams with opposite circular polarisations, σ_+ and σ_-, and a frequency slightly less than the atomic frequency (red-detuned). If an atom is displaced from the trap centre along the z direction where $z > 0$, the Zeeman shift moves the sublevel $m_F = -1$ closer to resonance with the laser frequency. Selection rules impose the absorption of photons by the beam that excites the σ_- transition, producing a scattering force which pushes the atom back to the trap centre. A similar process occurs when the atom is displaced towards the op-

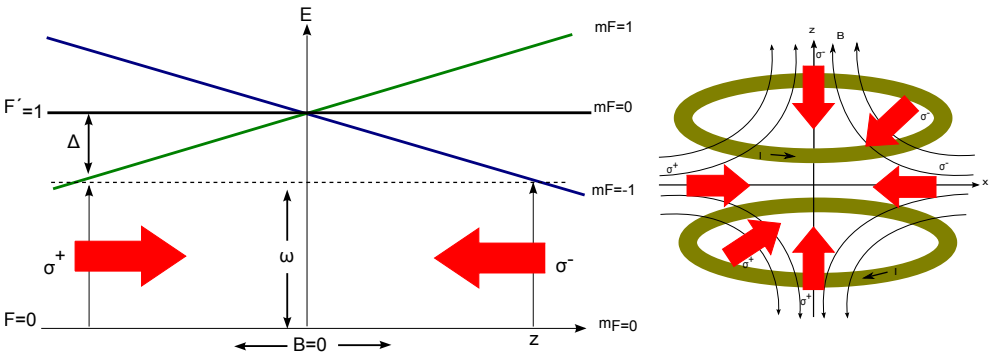

Figure 1.1: Illustration of the principle of the Magneto-Optical trap. Left: Energy of the Zeeman sub levels as a function of the position in one dimensional configuration of the Magneto-Optical trap for the atomic transition between $F = 0$ and $F' = 1$. Two counter-propagating circularly polarised laser beams, red-detuned with respect to the atomic transition interact with the atoms, coupling the σ^- component with the $m_F = -1$ state and $\sigma+$ component with the $m_F = 1$ state according to the selection rules. Right: The configuration of the laser beams in a three dimensional Magneto-Optical trap with two coils to produce a quadrupole magnetic field.

posite direction ($z < 0$). To describe this mechanism mathematically, the frequency shift produced from the Zeeman effect can be included in equation 1.11, thus obtaining:

$$F_{MOT} = F^{\sigma+}_{scatt}(\omega - kv - (\omega_0 + \beta z) - F^{\sigma-}_{scatt}(\omega + kv - (\omega_0 - \beta z)). \quad (1.14)$$

When the energy shift due to the Zeeman effect is $\Delta E = \mu_B g_F m_F \vec{B}$, $\vec{B} = \frac{dB}{dz} z$ and $\Delta m_F = 0, \pm 1$, the frequency shift will be $\beta z = \frac{g_F \mu_B}{\hbar} \frac{dB}{dz} z$ at displacement z where $\mu_B = \frac{e\hbar}{2m_e}$ is the Bohr magneton, g_F is the Landé factor of the relevant atomic state and $\frac{dB}{dz}$ is the magnetic field gradient. The total force in the MOT consists of a velocity and a spatially dependent force [24, 52] given by:

$$F_{MOT} = -\alpha v - \frac{\alpha\beta}{k} z, \quad (1.15)$$

where α is the damping coefficient. The restoring force has a spring constant $\alpha\beta/k$. The 1D configuration in figure 1.1 can be extended to 3D by using three counter-propagating laser beams with their intersection point located at the zero of the quadrupole magnetic field. The MOT provides a combination of a velocity dependent force (as in the optical molasses), which damps the atomic motion, and a position dependent

force, which pushes atoms back to the trap centre. This damping and trapping technique facilitates the MOT loading and makes it a versatile mechanism due to its robustness. The MOT can capture faster atoms than the optical molasses does. The mathematical treatment described here is simpler than the complete one which can be found in [92]. The most important requirement for the MOT is having a closed transition (for ^{87}Rb is $5^2S_{1/2}F = 2 \rightarrow 5^2P_{3/2}F = 3$) such that the atoms keep cycling within it. However, in the alkali metals such as ^{87}Rb, the atoms can decay to the $5^2S_{1/2}F = 1$ state rather than the $5^2S_{1/2}F = 2$ state. Unfortunately, the decay of this excited state is not coupled by the cooling laser beam. Therefore, another laser, called the re-pumper laser is required to excite the atom from the $5^2S_{1/2}F = 1$ state to the $5^2P_{3/2}F = 1$ or $5^2P_{3/2}F = 2$ state from which it can decay back to $5^2S_{1/2}F = 2$ where it can be excited again by the cooling laser.

1.2 Sub-Doppler cooling

In 1988, a fundamental experiment [53] revealed that the atoms can be cooled in optical molasses to temperatures below the Doppler limit. The theoretical explanation was reported in 1989 independently by two groups [15, 94] who confirmed that the Doppler limit may be overcome. In Doppler cooling, the cooling mechanism is based on the imbalance of the radiation pressure from the laser beams, whereas one of the cooling mechanisms in sub-Doppler cooling is based on the polarisation gradient of the light and resulting spatial modulation of the AC stark shift and optical pumping. This sub-Doppler cooling mechanism is also known as *Sisyphus cooling* in reference to the Greek myth of Sisyphus who was condemned to rolling a stone up an impossible hill. The main requirement of this mechanism is an optical lattice configuration [32, 63], with periodic potentials formed by interfering two or more laser beams.
To explain the sub-Doppler cooling mechanism, we consider a two level atom with angular momentum $J = 1/2$ and $J' = 3/2$ for the ground and excited states respectively as depicted in figure 1.2. This atom interacts with a light field of two counter-propagating laser beams having linear orthogonal polarisations. This arrangement is called $lin\perp lin$ optical lattice configuration where the polarisation changes with the position.

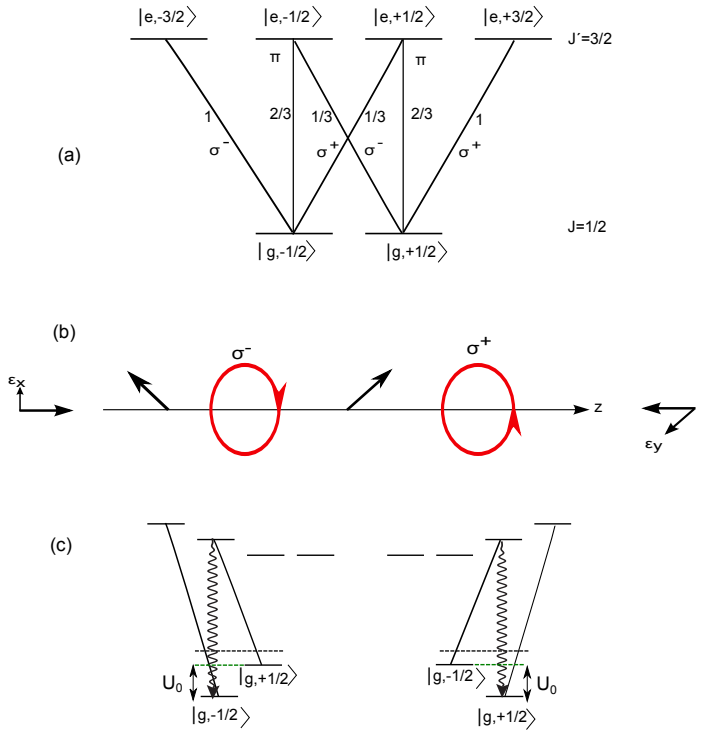

Figure 1.2: Sisyphus cooling mechanism. (a) Zeeman sublevels diagram for the transition $J = 1/2 \rightarrow J' = 3/2$ resulting from the coupling with light of different polarisations. The numbers indicate the squared Clebsch-Gordan coefficients, which are proportional to the transition strength for the allowed transitions that obey the selection rule $\Delta m_J = 0, \pm 1$. (b) The polarisation gradient for the $lin \perp lin$ optical lattice configuration, which shows the polarisation changes between σ^+ and σ^-. The laser beams propagate along z direction. (c) Diagram shows transferring the atoms between the Zeeman sub-level ground states (optical pumping), which causes the atoms to lose energy. The light shift in the Zeeman sublevels is always negative for negative detuning.

Two fundamental aspects of Sisyphus cooling, or polarisation gradient cooling, have to be taken into account. First, the *light shift* which is the atomic energy shift in the ground state sublevels, is determined by the interaction between the atoms' dipole moment induced by the laser, and the laser field itself. When the atoms are placed in the laser field, the electric field of the light induces a dipole moment in the atom in which the protons and electrons are polarised. To explain the light shift mechanism, the general model of a two level atom placed in the polarisation gradient light field is used. This induces the light shift in the ground Zeeman sub-levels $|g, \pm 1/2\rangle$. The strength of the shift is proportional to the square of the Clebsch-Gordon coefficients, which gives

the transition probabilities, and the light intensity of the relevant transition. Thus, the light shift depends on the light polarisation. As shown in figure 1.2, the polarisation gradient produces a spatial dependence in the light shift. For example, for σ^+ polarisation and red-detuned light frequency ($\Delta < 0$), the transition of $|g, +1/2\rangle \rightarrow |e, +3/2\rangle$ is three times stronger than $|g, -1/2\rangle \rightarrow |e, +1/2\rangle$. For this reason, the $|g, +1/2\rangle$ sublevel shifts three times lower than $|g, -1/2\rangle$. On the contrary with σ^- light, the $|g, -1/2\rangle$ is displaced three times lower than $|g, +1/2\rangle$ state. For negative detuning, the light shift is always negative for both light polarisations. So, depending on the spatial position of the atoms, the ground state sub-levels are subjected to a different shift acting as an optical potential which is a position-dependent potential for atoms in the ground state sublevels as illustrated in figure 1.3.

The second element in Sisyphus cooling is the *optical pumping* which is a mechanism of transferring the atoms between the ground state sublevels. Cooling the atoms requires a mechanism for dissipating energy. This process occurs when the atom moves over potential "hills" and "valleys", so that the atom's energy interchanges between potential energy and kinetic energy. When the atom absorbs light at the top of the potential hill, it will emit a photon thus returning to the bottom of the potential valley. The atom's energy is converted from kinetic energy to potential energy when the atom climbs the potential hill, and then dissipated via spontaneous emission at the end of this process, the atom's velocity will be reduced.

To elucidate the mechanism of optical pumping, it is essential to understand the process behind transferring the atoms between ground state sublevels. It can be shown that for a stationary atom, the Zeeman sublevel population depends on the atom position z in the light field. According to the selection rule $\Delta m_J = 0, \pm 1$, the σ_+ polarisation light drives the transition $|g, -1/2\rangle \rightarrow |e, +1/2\rangle$. Two possibilities may occur: either the excited atom in $|e, +1/2\rangle$ decays back to $|g, -1/2\rangle$, and then repeats the process, or it can decay into the $|g, +1/2\rangle$ state from where it cannot escape. The atom, which arrives at the ground sublevel $|g, +1/2\rangle$, can only be excited into $|e, +3/2\rangle$. This is because the σ_+ light only drives the transition $|g, -1/2\rangle \rightarrow |e, +1/2\rangle$ and from $|g, +1/2\rangle \rightarrow |e, +3/2\rangle$ from where it will only decay to $|g, +1/2\rangle$ due to

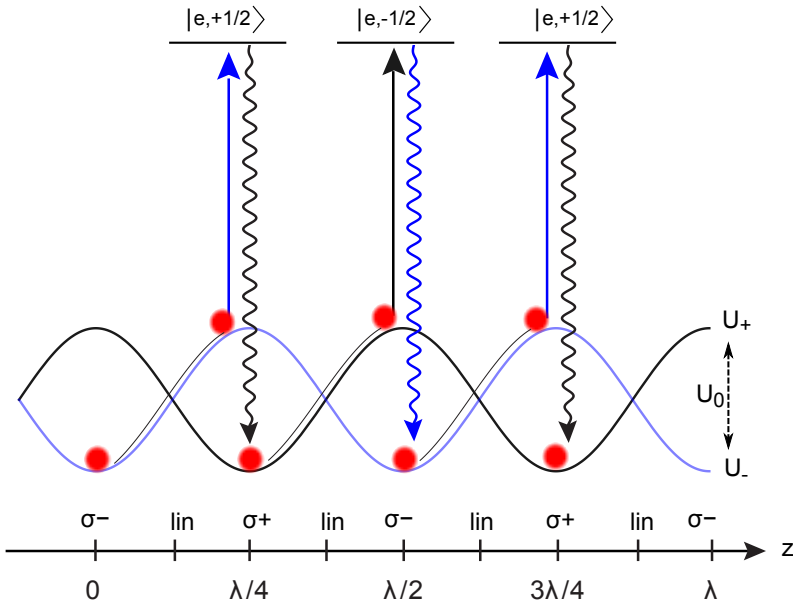

Figure 1.3: The optical potential in a 1D $lin\perp lin$ optical lattice in Sisyphus cooling. The spatially symmetric periodic potential results from the spatially modulated light shift for the atomic transition $J = 1/2 \rightarrow J' = 3/2$. The $U_{\pm}$ potentials are generated by the light shift modulation of the ground sublevels $|g, +1/2\rangle$ and $|g, -1/2\rangle$ respectively. The maxima and minima of the light shift potential are observed at position where the light is circular polarised.

the selection rules restriction. Consequently, absorbing σ_+ light causes pumping of the population from the $|g, -1/2\rangle$ into the $|g, +1/2\rangle$ ground sublevels through the excited state.

A similar process occurs when absorbing σ_- polarisation light to pump the atom into the $|g, -1/2\rangle$ sublevel. With linearly polarised light, both ground state sublevels are occupied with the same probability. It is noted that the most populated sublevel is the one with the lowest energy. Consider an atom located at the minimum of the substate $|g, +1/2\rangle$ potential where it can start absorbing σ_+ polarisation light. Therefore, the atom starts climbing the potential hill. In such process the interaction with the σ_- light polarisation position in the light field and thus the absorption probability increases. Then, the atom will be pumped into the $|g, -1/2\rangle$ substate, where the atom see itself in a valley. Then, the atoms starts climbing the next potential hill until it is pumped again into the $|g, +1/2\rangle$ state. After a few absorption-spontaneous emission processes, the atom loses its energy and gets trapped at the bottom of a potential well. Generally, moving the atoms within the polarisation gradient field dissipates

an energy per optical pumping cycle approximately equal to the light shift U_0 which is the depth of the potential well. This causes the atom to be localised at the periodic potential minima forming the so-called optical lattice. One can show that the Sisyphus cooling temperature limit is proportional to the recoil energy $T_r = E_r/k_B$, which is given by [24]:

$$k_B T_r = \frac{h^2}{m\lambda^2}, \tag{1.16}$$

where k_B is the Boltzmann constant, h is Planck's constant, m is the atomic mass, and λ is wavelength of the laser radiation.
For more complicated atomic energy levels such as ^{87}Rb used in our experiment, the Zeeman sublevel structure differs from the one shown in figure 1.2. Rubidium is widely used in the laser cooling experiments due to the simple scheme of the energy levels with a single valence electron. Figure 1.4 shows the ^{87}Rb D_2 transition, which is relevant to our experiment, with the hyperfine and Zeeman sublevels. Each of the $5^2S_{1/2}$ and $5^2P_{3/2}$ levels are split into $|J - I| \leq F \leq J + I$ hyperfine states. Because the ^{87}Rb possesses $I = 3/2$ nuclear spin [93], the ground state $5^2S_{1/2}$ splits into two hyperfine states $F_g = 1, 2$ for $J = 1/2$. The excited state $5^2P_{3/2}$ splits into four $F_e = 0, 1, 2, 3$ hyperfine levels. When the magnetic field is applied in the Magneto-Optical trap, the degeneracy of the atomic levels is lifted producing $2F + 1$ magnetic substates for each hyperfine level F. The cycling transition for ^{87}Rb D_2, is $5^2S_{1/2}F = 2 \rightarrow 5^2P_{3/2}F = 3$. The ground state splits into five ground sublevels $m_J = 0, \pm1, \pm2$ and seven excited sublevels $m_J = 0, \pm1, \pm2, \pm3$. This transition is not completely closed so the excited atom can decay into the $5^2S_{1/2}F = 1$ level, which is not coupled with the cooling laser. This causes the atom to escape from the trap. The re-pumper laser is therefore required to pump the atoms back into the $5^2P_{3/2}F = 2$ level from where they will decay into $5^2S_{3/2}F = 2$ ground state.

1.3 Magnetic trapping of neutral atoms

Magnetic trapping was introduced for the first time in 1985 by Migdall et al [66]. Two years later, experiments were achieved to trap atoms magnetically with enhanced density and atom number [2, 38, 96]. This

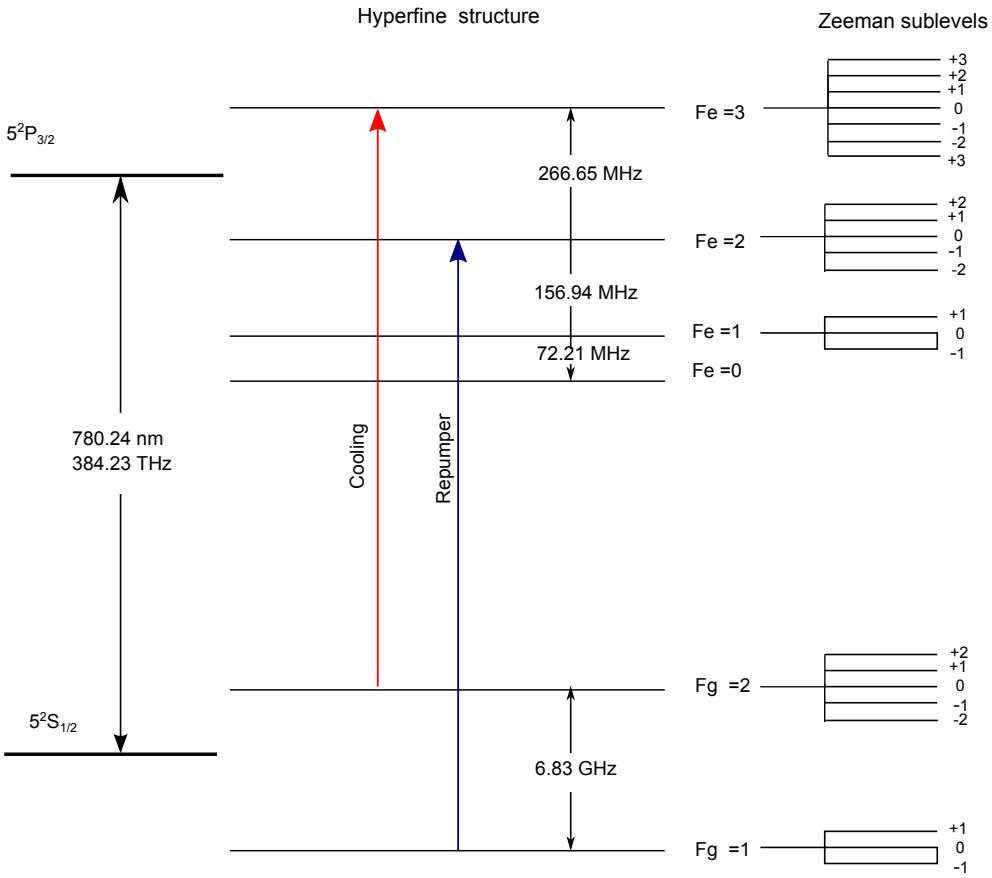

Figure 1.4: Energy levels for the hyperfine structure of the ^{87}Rb D_2 line. The cooling and the re-pumper transitions are indicated by the red and blue arrows respectively.

trapping mechanism is useful in many research areas, but is well known as the final stage to approach *Bose-Einstein Condensation*. Magnetic trapping confines atoms, which are pre-cooled by lasers, and compresses them to increase the collision rate that is required for evaporative cooling. The principle of the magnetic trap relies on the interaction between an inhomogeneous magnetic field and the atomic magnetic moment. To implement the magnetic trap, it is required to increase the magnetic field of the MOT coils, which allows only the colder atoms with lower energy to be retained in the trap centre. The principle of the magnetic trapping of neutral atoms is the interaction between the magnetic dipole moment μ of the atom and the applied magnetic field B as given by the following formula [65]:

$$E = -\vec{\mu}.\vec{B}. \tag{1.17}$$

For an atom in the state $|IJFM_F\rangle$ the energy shift that results from the Zeeman effect for weak magnetic fields is given by:

$$\Delta E = g_F \mu_B m_F B, \tag{1.18}$$

where m_F is the Zeeman sublevel of the hyperfine level F and μ_B is the Bohr magneton. The resultant force produced from the coupling between the magnetic field and the magnetic moment of the atoms, is of the form:

$$\vec{F} = -\vec{\mu}.\nabla\vec{B}. \tag{1.19}$$

Accordingly, the magnetic trapping force depends only on the magnetic field gradient (i.e. for atoms whose spin is aligned with the magnetic field, their potential energy increases linearly with increasing magnetic field). Because of the fact that local maxima of magnetic fields are forbidden in free space [101], a magnetic field minimum should be utilised to trap the atoms magnetically. Therefore, only atoms which are *low field seeking atoms* can be trapped in the potential minimum. *High field seeking atoms* are instead ejected from the trap. Therefore, the g_F sign determines the trappable magnetic sublevels. With $g_F m_F > 0$, atoms are low field seekers as the energy remains negative and so can be trapped at the minimum of the magnetic field. On the other hand, atoms with $g_F m_F < 0$ are high field seekers and cannot be trapped at the minimum. For the ^{87}Rb ground state, the low field seeking substates are $|F = 1, m_F = -1\rangle$ and $|F = 2, m_F = 1, 2\rangle$ since $g_F = -1/2$ for $F = 1$ and $g_F = 1/2$ for $F = 2$. The transition of the atoms from the low into high magnetic field causes them to be lost from the trap. This is because the atoms are moving in the trap, and so see the trap with different values and directions. In order to keep the atom in the trap, the atomic dipole moments must be adiabatically aligned to the direction of the magnetic field. This means that the magnetic moment precession of the atom has to be faster than the magnetic field change otherwise atoms end up in untrappable sublevels. The atom's magnetic moment precesses about the magnetic field with the Larmor frequency:

$$\omega_{Larmor} = \frac{\mu B}{\hbar}. \tag{1.20}$$

Therefore, in the region of the trap where the magnetic field is very small, the rate of the precession of the magnetic dipole moment μ about the magnetic field B is also very small. However, the adiabaticity is broken close to the magnetic field zero, thus the atoms are ejected from the trap due to Majorana spin-flip transitions [75].

1.4 Evaporative cooling

Laser cooling of atoms to extremely low temperatures and high phase-space densities is restricted by the photon absorption and emission mechanisms. So, to reduce the temperature further and increase the density, *evaporative cooling* is very effective because its mechanism does not rely on laser radiation [37]. The principle of evaporative cooling is similar to cooling a cup of coffee, where the steam takes the heat away. The atoms in thermal equilibrium have a Maxwell-Boltzmann distribution given by:

$$N(E) = N_0 exp(-E/k_B T). \tag{1.21}$$

To cool the atoms evaporatively, the hottest atoms in the cloud have to leave the trap carrying away energy which is more than the average energy. Atoms leaving the trap have energy larger than threshold energy, of a single atom given by:

$$E_{cut} = \eta k_B T, \tag{1.22}$$

where η is a parameter determining the evaporative time (truncation parameter), k_B is the Boltzmann constant and T is the temperature of the atoms. The remaining atoms in the trap experience elastic collisions, which determine the thermalisation process. The Boltzmann distribution is re-established as the atoms get rethermalised. This leaves the sample colder. The evaporation cooling time has to be relatively slow in order to allow the atoms to rethermalise. It must, however, be fast enough to avoid the inelastic collisions. This cooling process is continuously repeated, followed by a rethermalisation mechanism that produces a Boltzmann distribution which possesses colder atoms than before. This mechanism increases the phase space density (PSD), the number of atoms

per cubic de Broglie wave length, of the atomic sample in the harmonic trap, formed by the quadrupole-Ioffe configuration in our experiment, since the atoms accumulate around the potential minimum. In this situation the system reaches the quantum regime.
Evaporation can be produced by reducing the strength of the trap. This is not efficient however because it reduces the atomic density in addition to weakening the traps ability to hold the atoms against gravity. Another reliable method is evaporating the magnetically trapped atoms by applying radio frequency radiation to couple the trapped and untrapped Zeeman sublevels. Evaporative cooling does not show any fundamental temperature limit, but it will not be effective when there is a substantial decrease in the atom number.

1.5 Dipole trapping

Neutral atoms can be trapped optically by using an *optical dipole trap*. This mechanism relies on the interaction between the electric dipole and the far-detuned light. This trapping method was introduced in 1978 [5] and observed experimentally for neutral atoms for the first time in 1986 [12]. In general, the scattering force is neglected for a far-detuned laser field, as shown by equation 1.8 [24, 30].
With the assumption of large detuning and negligible saturation, the dipole trap potential, U_{dip}, and the photon scattering rate, R_{scatt}, can be expressed by the following [30]:

$$U_{dip}(r) = -\frac{3\pi c^2}{2\omega_0^3}\left(\frac{\Gamma}{\omega_0-\omega}+\frac{\Gamma}{\omega_0+\omega}\right)I, \tag{1.23}$$

$$R_{scatt}(r) = \frac{3\pi c^2}{2\hbar\omega_0^3}\left(\frac{\omega}{\omega_0}\right)^3\left(\frac{\Gamma}{\omega_0-\omega}+\frac{\Gamma}{\omega_0+\omega}\right)^2 I. \tag{1.24}$$

Here ω is the driving frequency, ω_0 is the atomic frequency and Γ is the damping rate or the natural linewidth, that corresponds to the spontaneous decay rate of the excited state. For simplicity, we apply the rotating wave approximation [54], by ignoring the counter rotating term $\omega_0+\omega$. The approximation holds as $\Delta \equiv \omega-\omega_0 << \omega_0$ and $\frac{\omega}{\omega_0} \approx 1$, and

the equations 1.23 and 1.24 can be simplified to:

$$U_{dip}(r) = \frac{3\pi c^2}{2\omega_0^3}\frac{\Gamma}{\Delta}I, \tag{1.25}$$

$$R_{scatt}(r) = \frac{3\pi c^2}{2\hbar\omega_0^3}\left(\frac{\Gamma}{\Delta}\right)^2 I. \tag{1.26}$$

These equations describe the behaviour of a two-level atom in a dipole trap. From the previous equations, it can be noted that for red-detuned ($\Delta < 0$) light, the atoms are attracted to the high intensity region as the dipole potential is negative. While blue detuned light ($\Delta > 0$), and a positive dipole potential leads to the ejection of the atom from the high intensity region. In addition, from equations 1.25 and 1.26, the dipole potential is proportional to I/Δ, while the scattering rate is proportional to I/Δ^2. Therefore, a large detuning of the laser field is important to reduce the scattering rate. This can be done as well as increasing the light intensity in order to retain the small scattering rate at a given potential depth. The simple relation between the dipole potential and the scattering force is :

$$\hbar R_{scatt}(r) = \frac{\Gamma}{\Delta}U_{dip}(r). \tag{1.27}$$

1.6 Thesis Overview

This thesis starts with the present introductory chapter devoted to the theoretical principles behind the work conducted in the next chapters. Chapter 2 describes the experimental apparatus and laser setups that were used in the experiments described in the following two chapters. Chapter 3 presents the theory behind the ratchet effect for cold atoms. This is followed by the description in Chapter 4 and Chapter 5 of the two experiments on the ratchet effect. The experimental setup and the results obtained from the experiment on the current reversals in a rocking ratchet are outlined in Chapter 4. Chapter 5 describes the vibrational resonance phenomenon and presents the experimental results obtained from the related experiment. Chapter 6 introduces the theoretical concepts related to Bose-Einstein Condensation in addition to the new laser system and the results of this last experiment. Finally, the purpose of Chapter 7 is

concluding the thesis work and highlighting the next step of the dipole trap experiment.

Chapter 2

Experimental apparatus

This chapter describes the setup that is used to run the experiment. It starts with the vacuum system, which is an essential component to prepare the cold cloud of ^{87}Rb atoms. Since it is desirable to trap cold atoms with a long life time, the vacuum system was upgraded from a single MOT chamber, as used in previous experiments, to a double MOT chamber. This reduces background collisions in the main chamber and therefore increases the lifetime of the trapped atoms, which is a necessary requirement for Bose-Einstein condensation. Then, the chapter proceeds to describe the laser system and the setup used to produce the cooling, re-pumper, lattice and imaging beams. The frequency stabilisation mechanism which is called Doppler Free Dichroic Atomic Vapour Laser Lock (DF-DAVLL) is also described in this chapter. Experiments with cold atoms require control of all experimental parameters with high temporal resolution and stability. The computer control to achieve this is presented in the following section. Finally, the details of the imaging system are reported in the last section.

2.1 Vacuum system

The vacuum system of the single MOT chamber was constructed by the previous PhD students and is described in [20, 25, 51]. The current section describes only the design and construction of our current vacuum system. The new vacuum system consists of two chambers. In the first (*LVIS chamber*), the cold atoms are prepared in a magneto-optical trap

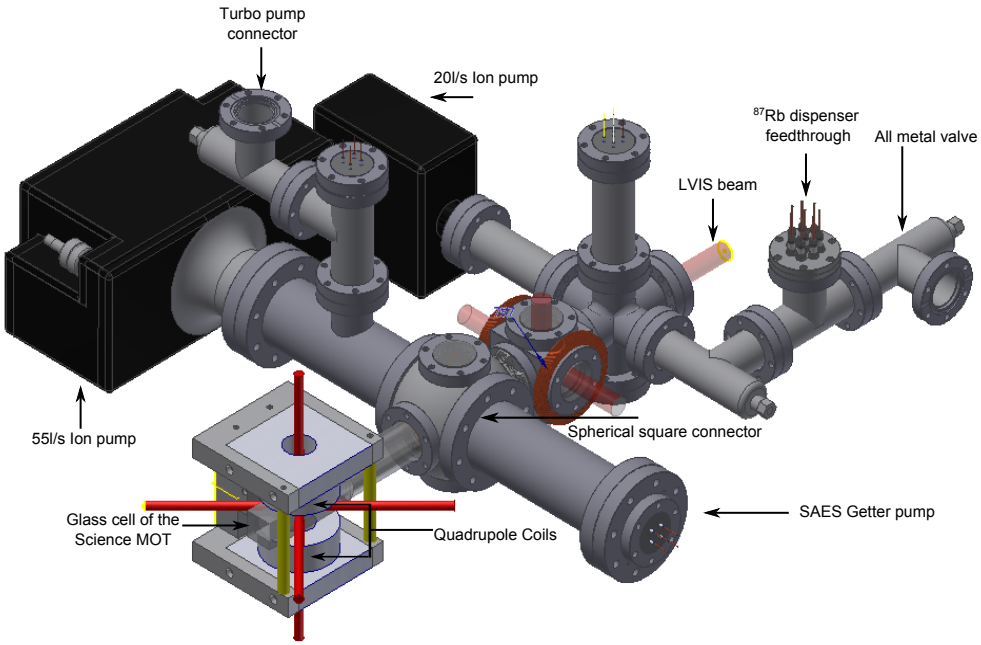

Figure 2.1: The ^{87}Rb vacuum system overview which illustrates the vacuum components. The first vacuum chamber consists of a cubic glass cell connected to the ^{87}Rb dispenser. The atoms are transported from the first MOT into the science MOT via a 1.5 mm hole using a Low Velocity Intense Source of atoms. In the science cell the atoms are trapped by another MOT using a compact design of quadrupole coils. Two ion pumps are shown in the system, which are used to maintain the low pressure in both chambers. Another SAES getter pump can be attached to improve the vacuum environment.

loaded from a background vapour of ^{87}Rb at room temperature. We then extract an atomic beam to the second chamber (*Science chamber*) which has an Ultra-High Vacuum (UHV) below 10^{-10}mbar. The vacuum construction can be seen in figure 2.1.

LVIS There are various methods to produce slow atomic beams. The Low Velocity Intense Source of atoms (LVIS) [56] configuration is implemented in this experiment. This method has many advantages such as simplicity, compactness and the ability to produce an intense atomic flux. A cross section of the vacuum setup is shown in figure 2.2. The thermal ^{87}Rb atoms are produced in the LVIS chamber by flowing current through an alkali dispenser[1] connected to an electrical four-pin feedthrough, which

[1]SAES Getter, Rb AMD Rb/NF/5.4/12.5/FT 10

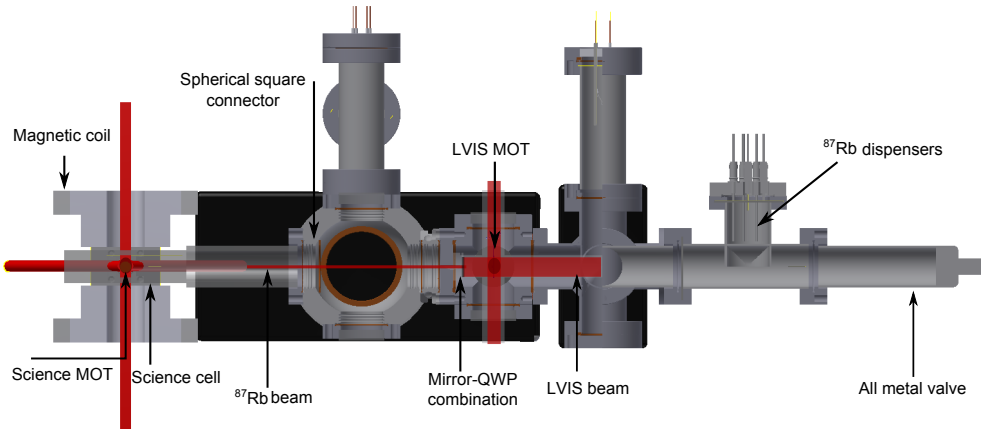

Figure 2.2: The cross section of the vacuum system shows the LVIS beam path, which passes from the first MOT chamber through the mirror-quarter wave plate combination and a spherical-square connector into the second cell.

was later replaced by an eight-pin feedthrough[2]. This limits the pressure in the LVIS chamber to about 10^{-9} mbar. Collisions between hot background gas and cold MOT atoms lead to heating and trap losses and therefore reduce the trap lifetime. The trap in the LVIS chamber is produced by three counter-propagating laser beam pairs, each pair having opposite circular polarisation. This configuration allows us to optimise the beam balance using a half wave plate and a polarising beam splitter placed in each beam's path, and therefore centres the position of the MOT. The position of the MOT with respect to the hole is crucial for the flux of cold atoms. The LVIS push beam is retro-reflected by a mirror inside the vacuum, while the other beams are not. The atoms are transported to the science chamber through a 1.5 mm hole as an extraction channel for the atomic beam due to the imbalance in radiation pressure. This arrangement offers a differential pressure between the chambers and reduces the problem of background collisions in the science cell, therefore boosting the trap lifetime [90]. The pressure in the LVIS chamber is maintained by an ion pump and can be monitored via the current displayed on the pump controller[3]. The LVIS configuration provides pressure below 10^{-10} mbar in the science cell.

In addition to the MOT coils in anti-Helmholtz configuration, there

[2]EFT0583093 from Kurt J. Lesker
[3]MiniVac controller

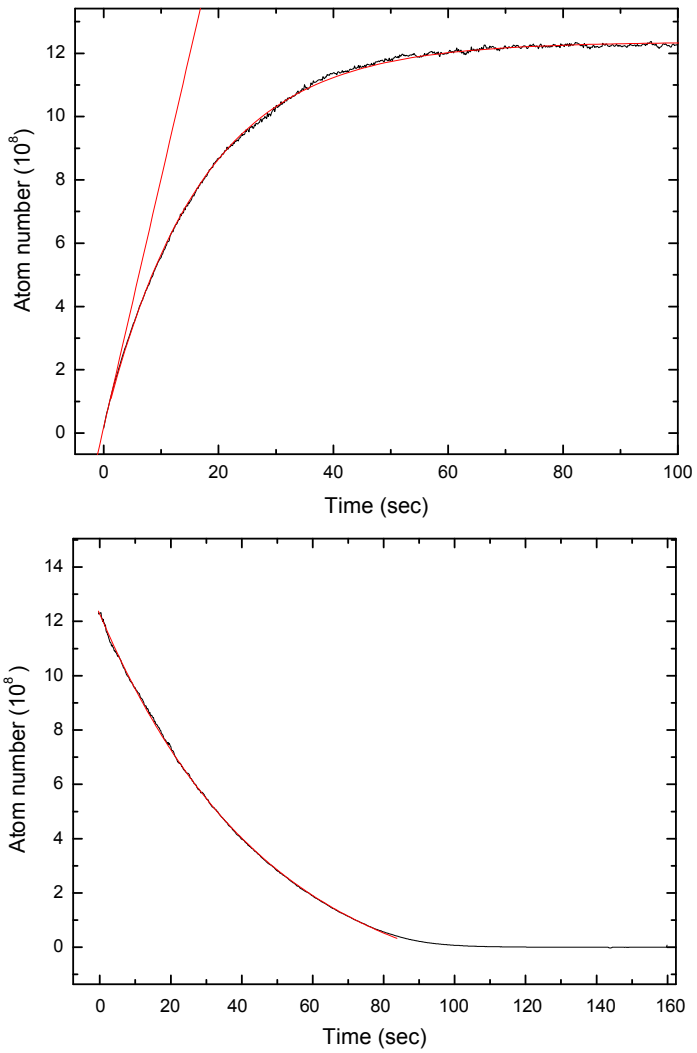

Figure 2.3: Upper panel: The atom number of the science MOT as a function of MOT loading time. The red curve is an exponential fit to the data. The red line is a linear fit from the origin with a slope of 7.8×10^7 atom/s, which is the loading rate of the science MOT. Lower panel: The exponential decay of the science MOT after switching the LVIS beam off. The red curve is an exponential fit. The decay time is about $37.7\,s$. It can be seen that after $85\,s$, the MOT continues to decay but this cannot be recorded by the camera chip due to the MOT small size. The atom number is measured by the fluorescence imaging with a Charge-Coupled Device (CCD) Pixelfly camera.

are two pairs of compensation coils in Helmholtz configuration used to position the trap vertically and horizontally in front of the hole. To increase the capture range, a telescope is built to increase the laser beam waist to about 1 cm with a power of about 4 mW per beam. Re-pumper light of 3 mW is overlapped with the MOT beams.

Vacuum components The LVIS chamber consists of a standard six way cube with 2 3/4" flanges. The blank flange of the cube that leads to the science cell is modified with a mirror-quarter wave plate combination with the small hole in the centre which acts as the differential pumping stage. This combination is glued to the flange using a low vapour pressure glue[4] which is suited for vacuum pressures below 10^{-9} mbar. The distance between both the LVIS and science MOT is 330 mm. The rubidium dispensers are in a separate compartment of the first MOT chamber connected via a valve. This enables us to replace the ^{87}Rb dispensers without pumping and baking the rest of the vacuum system each time the dispensers are replaced (approximately each year). After exchanging the dispensers the chamber could be pumped out via an additional valve without contaminating the main chamber. The science chamber consists of a glass cell with dimensions $(30 \times 30 \times 100)$ mm^3. The LVIS and the science cell are connected via a spherical square connector[5], multi-CF (ConFlat) flanges fitting port with two 4 1/2" CF ports and four 2 3/4" CF ports. One of the small ports is attached to the LVIS cell and another small port is attached to the science cell. The two ports left are used to perform some measurements, such as an atomic flux measurement. The large ports are connected to the ion and getter pumps. Two ion pumps and one getter pump are used to maintain the pressure in both vacuum chambers. In the LVIS chamber, the ion pump[6] has a pumping speed of 20 l/s. In the science chamber the pressure is maintained by a slightly bigger pump[7] with 55 l/s. A Non-Evaporable Getter (NEG) pump[8] is additionally used to improve the vacuum environment and increase the pumping speed.

As can be seen from figure 2.3, the upper curve represents the loading graph with 7.8×10^7 atoms/s loading rate which can be improved by alignment to obtain more atoms in the trap. The lower graph shows the MOT decay behaviour when switching off the LVIS beam. The trap life time is about 37.7 s in the science chamber with the final pressure below 10^{-10} mbar, which enables sufficient trapping times for Bose-Einstein

[4]Varian TorrSeal
[5]Kimball Physics, MCF450-SphSq-E2C4
[6]Varian Inc.,Vaclon Plus 20 StarCell
[7]Varian Inc.,Vaclon Plus 55 StarCell
[8]SAES Getter, SORB-AC^{TM}GP100 MK5 St 707

Condensation.

Baking procedure After assembling the vacuum system, the next step is to pump it down. Three different pumps are used to obtain high vacuum condition, since each pump works best for different pressure regimes. The rotary pump can take the system down to 10^{-1} mbar. The second pressure stage is 10^{-5} mbar and is reached by using a turbo pump which is connected in series with the rotary pump. Ultra-high vacuum is reached and only maintained by the ion and getter pumps. Outgassing is an unavoidable problem of any vacuum system because of remaining undesirable gases on the internal surfaces of the vacuum. Baking the system increases the outgassing rate and releases the unwanted gases from the walls. The baking process starts by wrapping heat tape, covered by layers of aluminium, around the vacuum chamber to ensure even distribution of temperature. It is vital to heat the system gradually with a rate of 10 °C/h in order to prevent any damage due to temperature gradients. We baked the system for a week. The science cell was baked at about 200 °C and the LVIS cube at about 120 °C, which was limited by the maximum temperature rating of the vacuum glue. Normally, both the glass cells' temperature, and the vacuum pressure, are monitored and recorded every five minutes during the heating and the cooling procedure. After cooling the system back to room temperature, the turbo pump valve is closed. The final pressure in the LVIS chamber is about 10^{-9} mbar.

2.2 Laser system

Tuneable lasers are a basic requirement to cool and trap atoms [99]. Commercial semiconductor laser diodes are used in our system to provide the MOT and lattice beams. After upgrading the vacuum system to a double MOT system, more laser power was needed to distribute it sufficiently for both MOT systems. The new laser system implements a Master Oscillator Power Amplifier (MOPA) and is described in chapter 6. Another high power 50 W laser, which is a fibre amplifier[9] with 1064 nm wavelength, was installed recently for an optical dipole trap. The rest of

[9]NUA-1064-PD-0050-D0 1064- 1110

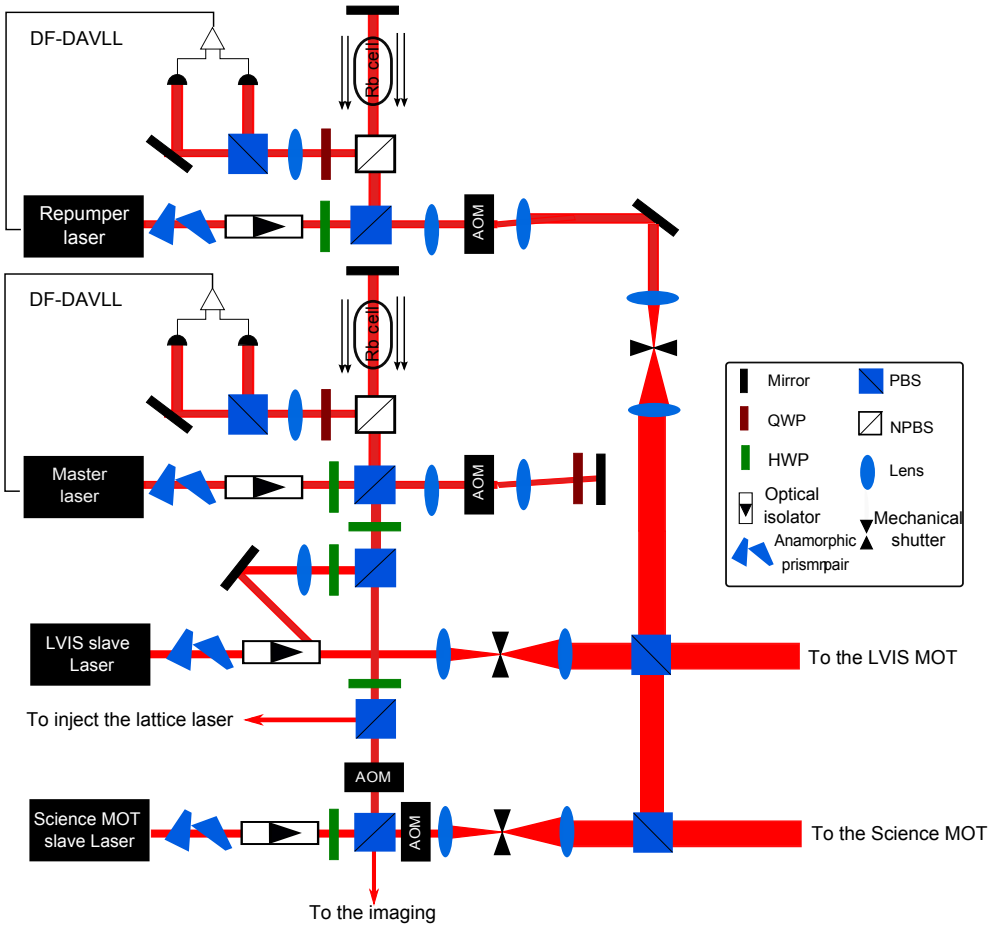

Figure 2.4: Schematic of the laser setup. Three types of lasers are used: The master as a cooling laser, re-pumper and two slaves for both the LVIS and science MOT. Anamorphic prism pairs are placed after the laser directly to transform the elliptical profile of the laser beam into circular. An optical isolator then is used to prevent the laser injection from the back reflected light. Both slaves are injected from the master by sending a fraction back to the slave laser by the side of the optical isolator. A half wave plate (HWP) before the polarised beam splitter is used to balance the power between each beam. To control the laser frequency and switching the laser beam off and on, an Acousto-Optical Modulator (AOM) is used. The master laser frequency is shifted up twice by 100 MHz with the double pass AOM. A quarter wave plate is placed after the double pass AOM to rotate the polarisation and thus enable the beam to be reflected from the polarising beam splitter (PBS) to inject the slaves.

this section deals with the MOT and lattice lasers, their construction as External Cavity Diode Lasers (ECDL) and their frequency stabilisation.

2.2.1 Laser setup

The laser system is based on the home built single-sided external cavity design [103] in Littrow configuration [85] with a commercial laser diode[10]. This configuration consists of a laser diode mounted together with a collimating lens that has a high numerical aperture. The collimated beam is then diffracted by a holographic grating[11] that is attached to a mount which can be finely adjusted in both the vertical and horizontal directions. This arrangement creates an external resonator with the laser diode and narrows the linewidth of the free running laser. It also enables us to tune the frequency by changing the angle of the grating because the first diffracted order is fed back into the laser diode. The laser frequency can now be controlled by adjusting the grating angle, which affects the laser frequency twofold: by changing the length of the external cavity and therefore its resonance frequency, and also by changing the diffraction angle of the first order. It is done electronically with a piezoelectric transducer[12]. To limit frequency drifts, the diode laser's temperature is stabilised. Therefore, the frequency sensitive construction is mounted on a Peltier element[13], with the laser's massive aluminium base acting as a heat sink. The temperature is measured with an AD590 temperature sensor glued close to the laser diode and the temperature is then kept stable by a commercial temperature controller[14].

In our laser setup, three types of lasers are implemented: the master which is the cooling laser, the re-pumper laser and a slave laser. Both the master and re-pumper lasers are ECDLs in the Littrow configuration [85], which enables us to control their frequency, whereas the slave is just a laser without a grating and is injected by the master laser to force it to work at the same frequency of the cooling laser. The schematic of the laser setup is illustrated in figure 2.4.

[10] DL7140-201S 785 nm, 70 mW from Thorlabs
[11] Holographic grating GH13-18V
[12] Piezomechanik Pst 150/4/5
[13] Peltier cooler muticomp-mcpe1-12707AC
[14] Wavelength Electronics, MPT-2500

2.2.2 Dichroic Atomic Vapour Laser Lock (DAVLL)

Since the diode laser central frequency drifts over time due to temperature, current and mechanical fluctuations, the frequency needs to be actively stabilised to an atomic transition. The technique we use is called Doppler Free Dichroic Atomic Vapour Laser Lock (DF-DAVLL)[67, 72]. The principle of this technique is to induce dichroism in the ^{87}Rb vapour cell by applying an external weak magnetic field. This leads to a shift of the magnetic sublevels of the ^{87}Rb hyperfine levels due to the Zeeman effect. This makes the gas absorption frequency dependent on the circular polarisation of the probe light. The mechanism is implemented by sending a fraction of linearly polarised laser light, to produce a pump beam, through a rubidium cell enclosed by a solenoid. To be able to observe the hyperfine structure, the beam is retro reflected, to produce a probe beam with much less intensity than the pump beam. Both beams have to be overlapped inside the ^{87}Rb vapour cell to interact with the same set of atoms. Therefore, scanning the laser frequency over the atomic transitions produces the Doppler-free spectrum with its hyperfine structure. Then, a weak magnetic field is turned on to produce the Zeeman shift. According to the selection rules $\Delta m = \pm 1$, $\sigma\pm$ light couples different sublevels. Since the linearly polarised probe beam can be seen as a superposition of equal components of $\sigma\pm$ light, the gas is simultaneously exposed to both polarisations. After the cell a quarter wave plate and a polarising beam splitter enable us to observe each circular component separately with a photodiode (see reference [78] for more information about the photodiode box). A differential amplifier subtracts both signals and produces an error signal with a linear slope and a zero crossing, which is a reference to the laser frequency and is used to lock the frequency. The error signal is integrated and fed back to control the piezoelectric transducer. Thus, it controls the diffraction grating angle on which the piezo element is mounted. This locking mechanism is less sensitive to the noise sources when the laser frequency changes. As shown in figure 2.4, five lasers are implemented in the experiment: The master, LVIS MOT slave, science MOT slave, re-pumper, and the optical lattice laser (its schematic will be shown in chapters 4 and 5).

Master laser The master laser controls the frequency of the light required for the MOT. The frequency of the master laser should be set slightly below the resonance frequency (red-detuned) of the cycling transition $5^2S_{1/2}F = 2 \rightarrow 5^2P_{3/2}F = 3$. Therefore its frequency is locked to the $5^2S_{1/2}F = 2 \rightarrow 5^2P_{3/2}F = 1, 3$ cross-over line with a detuning of -211.79 MHz to the transition. A cross-over transition has a frequency midway between any two excited levels. The cross-over transitions can be observed when the laser frequency is scanned over the whole frequency range of the atomic transitions (cycling and hyperfine transitions). Apart from the light used for the stabilisation all laser output is shifted up in frequency by a double pass AOM[15]. This enables us to control the laser frequency electronically by changing the applied radio frequency to the AOM. After the AOM, the laser beam gets reflected by a mirror and then passes through a quarter wave plate (QWP) in order to rotate the polarisation and thus enable the beam to get reflected from the polarising beam splitter used to inject the slaves. In normal operation we shift the laser frequency up twice by about 100 MHz and obtain an effective detuning of -2 Γ (i.e. 12 MHz) where Γ is the natural linewidth for ^{87}Rb ($\Gamma = (2\pi)6.066$ MHz). The detuning can be controlled by the computer within $-6\Gamma \leq \Delta \leq +2\Gamma$.

Slave laser The output power from the master laser is around 50 mW, and most of it is lost in the double pass AOM configuration and other optical components, or used for the DF-DAVLL spectroscopy. For this reason, a slave is required to amplify the cooling laser light. Therefore, the slave gets injected by the master beam (even a few microwatts are enough). The master laser beam is split into two parts to inject both slaves. This is performed by sending a fraction from the master laser back to the slave by a polarising cube inside the optical isolator. This forces the slave laser to oscillate at the lasing frequency of the master but provides far more power since there is no diffraction grating. High power is essential to trap a sufficient number of atoms. Most of the light is sent to supply the LVIS MOT beams, but a small fraction of the master laser is used to inject another slave, which is then used for the science MOT. To be able to electronically control the light intensity of this beam we

[15] AOM 3080-122 from Crystal Technology

introduce an AOM, with 80 MHz central frequency, in the beam path. To compensate for incurring an 80 MHz shift, another AOM is placed in the injecting beam. Even if the AOM is switched off, still there is a light leakage from the first order, which may occur even without applied radio frequency. Therefore, mechanical shutters are placed after the AOMs to block any undesirable light.

Re-pumper laser The re-pumper frequency is also locked using a DF-DAVLL. Here the locking feature is the $5^2S_{1/2}F = 1 \rightarrow 5^2P_{3/2}F = 1, 2$ crossover line. Since the re-pumper absorption feature is very small at room temperature, the vapour cell is heated up to 60 °C. The light not used for the spectroscopy is then shifted up by 80 MHz to reach the re-pumping transition $5^2S_{1/2}F = 1 \rightarrow 5^2P_{3/2}F = 2$. A non-polarising beam splitter (NPBS) is utilised to divide the re-pumper beam for both MOTs. Then the re-pump light is combined with the cooling light via polarising beam splitters.

2.3 Experimental control

Cooling and trapping atoms in a MOT followed by several other cooling stages, such as optical molasses and evaporative cooling, requires reproducible data collection with a high repetition rate. This can be executed effectively by controlling all experimental parameters with a computer. We used two computers: one for the experimental control and one for data acquisition. The first computer is used to control all experimental parameters in a temporal sequence. Parameters are, for example, the time intervals for each experimental phase, frequency detuning, beam intensities and magnetic fields for the MOT. The computer control consists of a digital PCI-card with 64 digital In/Out channels[16] and two analogue output cards with eight channels each[17]. The digital card is mainly used for on/off switching in combination with electronic circuits that interface with the experiment. For example, the mechanical shutter switching is controlled by sending a digital signal from the computer control to an electronic circuit to switch the shutter when a high voltage reaches the

[16] Viewpoint DIO-64
[17] National Instrument PCI-6731

shutter solenoid. A digital signal also can be sent to the function generators to trigger them. While, the analogue card can produce ramps e.g. for the detuning or the intensity of the lasers. The analogue card is also used to control the magnetic field of the anti-Helmholtz and Ioffe coils by varying the coils current. The output range of this card is from -10 V to +10 V with 16 bit resolution. The overall timing resolution is 1 μs which determines the time precision for the experimental sequence.
Controlling the coils current is done by using a high power Metal Oxide Semiconductor Field-Effect Transistor (MOSFET)[18] bank, which has eight MOSFETs in parallel. The voltage over the MOSFET gate, which is controlled from the computer, is proportional to the coils current. The gate voltage is stabilised by a feedback circuit whose set point is controlled by the analogue output card. The MOSFETs are mounted on copper water cooled plates in order to dissipate the generated heat due to the high current.
The second computer is connected to the CCD camera and is utilised to acquire and save the images. Two types of images can be taken: real time images, which monitor the atomic cloud continuously and can help to verify immediately the cloud stability and the laser locking. Also, images can be taken when the camera is triggered to open its shutter, by receiving a digital signal from the computer control. This triggered image is taken for a specified time determined by the experimental sequence. The imaging is usually the last stage of the experimental sequence to be able to observe the effect of the sequence stages on the atomic cloud. Most experimental data in cold atom experiments consists of position and size data of the atomic cloud. In most cases the images are fitted with a 2D Gaussian function, the fit result saved in a file and analysed to determine the outcome of the experiment. For the ratchet experiment, it is necessary to control the frequency and amplitude of the bi-harmonic force (defined in chapter 3). Therefore, the acquisition computer is responsible for controlling the function generators which are connected to the computer via a USB. A Rohde and Schwarz function generator used for the radiofrequency evaporation for the BEC production is also connected to the computer control via an RS232 port. The LabView code, the software used as a user interface for both computers, was written by

[18] IXFN150N15-MOSFET, N, SOT-227B from Farnell

the previous PhD students [25, 51].

2.4 Summary

This chapter describes the construction of the new vacuum system. A double MOT chamber in the LVIS configuration was installed, which reduces the vacuum pressure in the science MOT significantly from 10^{-9} mbar for the LVIS chamber, if used as a single chamber, into below 10^{-10} mbar. The life time of the science MOT reaches 37.7 s. This is sufficient for successful BEC creation. The laser system for the experiments was concisely described. Details about the laser experimental setup and the respective frequency stabilisation were given. The chapter ended with a brief description of the experimental control.

Chapter 3

Ratchets

3.1 Introduction

Transport phenomena are a very interesting topic in many fields of science like physics, chemistry, and biology [83]. Brownian motors, or ratchets, are microscopic devices that turn random fluctuations into directed motion in the absence of a bias force. Ratchets are an intriguing phenomenon that have attracted the attention of the scientific community for their numerous applications, such as electron pumps [95] or particle separation devices [86]. Our group already devoted a lot of work towards the understanding of ratchet mechanisms [26, 27, 29, 42]. Two ratchet experiments were conducted during my study period, which will be described in the next two chapters. The first experiment investigates current reversals [83], i.e. variations in the atomic current direction as a function of one of the experimental parameters, in rocking ratchet [4]. This is a kind of ratchet in which the optical potential is rocked periodically. The second experiment studies the vibrational resonance phenomenon. This chapter describes the principles behind the ratchet effect.

3.2 Brownian motors or ratchets

Ratchets are devices that rectify fluctuations and generate a directed current out of unbiased fluctuations. Ratchets are useful for the understanding of how nanoscale motors can work under the influence of substantial thermal motion. Many physicists explored the possibility of extracting

work from a system without violating the second law of thermodynamics [35]. This led to the design for paradoxical perpetual motion machines. A first gedanken experiment on the topic was the Feynman-Smoluchowski ratchet [83]. It was first considered by Smoluchowski in 1912 and later extended by Feynman. In 1963, Feynman [22] analysed Smoluchowski's ratchet and pointed out its limitations with respect to the generation of directed motion in thermal equilibrium; it would violate the second law of thermodynamics. He showed, however that if operated out of equilibrium the ratchet mechanism can be used to rectify fluctuations.
In general, it is not possible to generate directed current from systems in thermal equilibrium otherwise it will violate the second law of thermodynamics. An additional requirement is related to the symmetries of the system. As it will be discussed in detail in the following, it is necessary to break the symmetries which would otherwise prevent directed motion. Thus, gaining useful work out of unbiased random fluctuations, and the occurrence of the ratchet effect, require two elements: out of equilibrium settings and breaking one or more of the system symmetries. According to Curie's principle, which states that if a certain event is not ruled out by symmetry then it will occur [83], this is sufficient to produce directed transport.

The Smoluchowski ratchet is a device with an axle and a paddle wheel attached to one end and an asymmetric gear wheel to the other end, as shown in figure 3.1. The gear wheel is usually termed the ratchet wheel. The whole device is immersed in a gas at thermal equilibrium. It is thus subjected to the random fluctuations of the gas (Brownian motion). A pawl attached to the ratchet wheel stops the wheel rotating in one direction. In the other direction however the wheel is free to rotate. Random collisions of the gas would now start to rotate the wheel in the permitted direction even if a small load is applied and thus extract work out of thermal equilibrium which is forbidden by the second law of thermodynamics. The reason why such a process is not possible, according to Smoluchowski, is that the pawl itself would have to be extremely small. The random fluctuations of the gas molecules would then move the pawl as well. So overall useful work cannot be extracted.

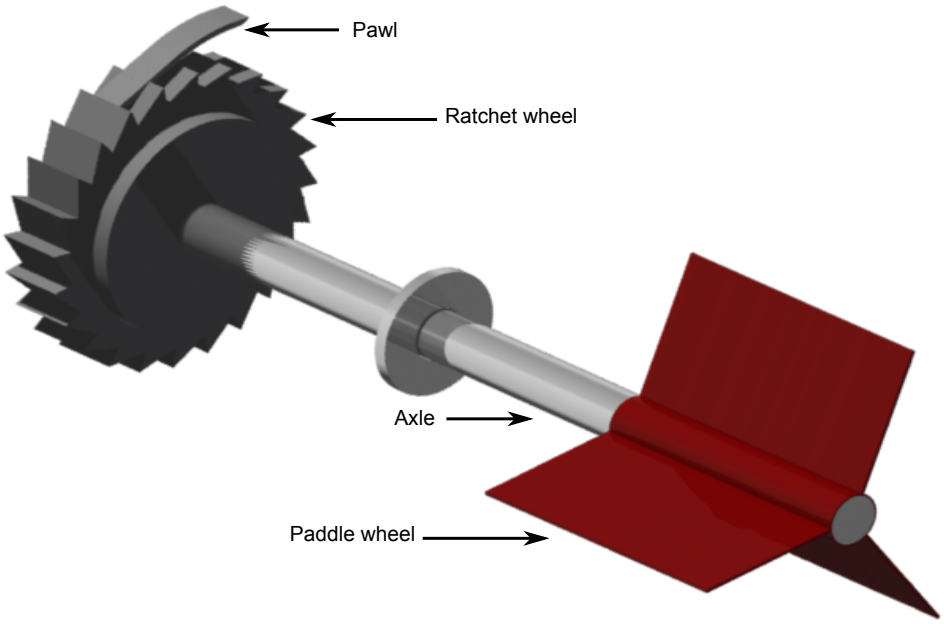

Figure 3.1: The ratchet wheel is connected to the paddles by an axle. The whole device is immersed in a gas at thermal equilibrium. The pawl is attached to the ratchet wheel to rectify the motion in one direction. Without the pawl, the random motion of the gas produces unbiased rotation.

Feynman rachet Feynman extended the Smoluchowski device. This was done by introducing two reservoirs with different temperatures. The paddle wheel in one reservoir, and the ratchet with the pawl in the other reservoir, as shown in figure 3.2. Feynman demonstrated that if the entire system is at the same temperature, there is no rectification. On the other hand, if the temperature of the two reservoirs is different, the ratchet can move in one direction and can extract useful work, such as lifting a weight that is attached to the axle. So, a temperature gradient can produce work. This does not violate the second law of thermodynamic which is valid only at the thermal equilibrium with a single bath at a single temperature. The ratchet device should be considered at the molecular scale where the thermal noise, which results from the thermal fluctuations in the system environment, plays a significant role. Without the asymmetric feature of the wheel, no movement will be expected. In the following, to illustrate the ratchet phenomenon in more details, I will focus on one class of ratchets, the so-called rocking ratchet, as it corresponds to the scheme used in our setup. The other types of ratchets are described in detail in Ref. [83].

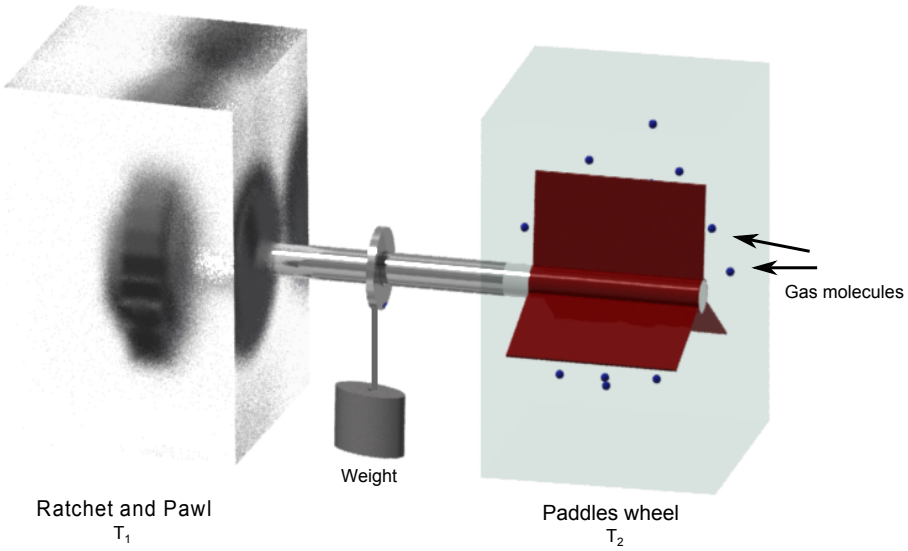

Figure 3.2: Feynman ratchet. The ratchet wheel and the pawl are placed in a reservoir with temperature T_1. The paddle wheel in a second reservoir with temperature T_2. The pawl is supposed to rectify random fluctuations of the paddle which therefore might be used to extract work (such as lifting a weight) when the temperature of the two reservoirs is not the same.

3.3 Rocking ratchets

The last twenty years have seen a considerable amount of studies aimed to understand the rectification mechanisms at the molecular scale. Ratchets were discussed again in 1993 by Magnasco [57]. In 1997, the quantum ratchet in an adiabatically rocked ratchet system was investigated theoretically [84]. Most of the publications were theoretical due to the difficulty in performing experiments at the nanoscale. Recently, ratchet experiments for cold atoms were reported. The first rocking ratchet for cold atoms was demonstrated in 2003 [88]. Rocking ratchets, or generally AC driven ratchets, are one of the most common ratchets. Rocking ratchets can be realised by using either an asymmetric spatial potential and zero mean symmetric driving force, or a symmetric spatial potential and a temporal asymmetric driving force. The latter configuration is used in our system.

The principle of a rocking ratchet is shown in figure 3.3: a spatially symmetric potential is rocked, or tilted, by a time asymmetric zero average force. This force drives the system out of equilibrium and breaks the system symmetry. Therefore, a directed current can be generated.

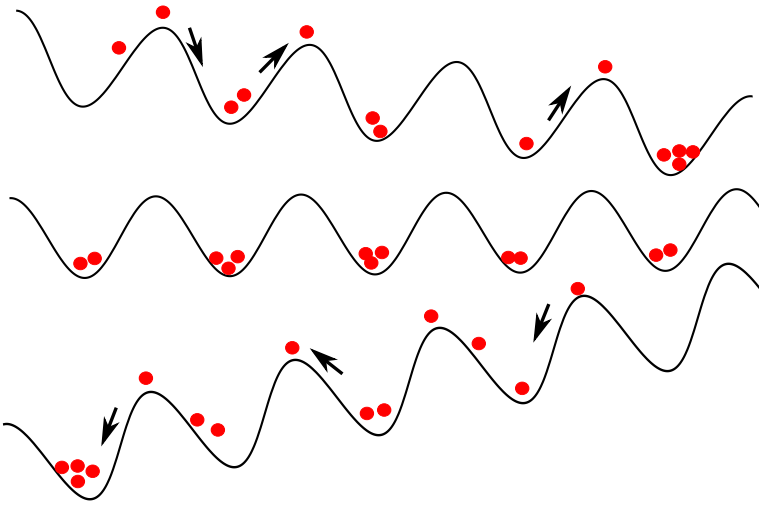

Figure 3.3: The mechanism of the rocking ratchet. A spatially symmetric potential (shown in the middle of the figure) is tilted by a time asymmetric bi-harmonic force. The potential is rocked between two asymmetric potentials (shown in the upper and lower drawing of the figure). The time-average of the applied force is zero. The ratchet current is produced as a result of the force asymmetry.

A complicated behaviour can be observed, the so-called current reversals [83]: the current can change its direction (sign) by tuning some of the system parameters such as the driving frequency or the noise strength.

3.4 Simple stochastic model

Brownian particles are one of the key elements in the simplest model to describe the ratchet dynamics. For simplicity, one dimensional motion is used to describe the system dynamics. If we consider a Brownian particle with mass m moving in the x direction, the dynamics can be described by Newtons's equation of motion:

$$m\ddot{x} = -\gamma\dot{x} + \zeta\left(t\right), \tag{3.1}$$

where γ is the damping or friction coefficient, $\dot{x}, \ddot{x}$ are the first and second derivative of x with respect to the time and ζ is Gaussian white noise term. The Gaussian white noise has a zero average value:

$$\langle\zeta\left(t\right)\rangle = 0, \tag{3.2}$$

which means that the noise is unbiased. The Gaussian noise in equation 3.2 obeys the auto-correlation function given by the fluctuation-dissipation relation [35, 83]:

$$\langle \zeta(t)\,\zeta(t')\rangle = 2\gamma k_B T \delta(t-t'), \tag{3.3}$$

where k_B is Boltzmann constant, T is the system temperature, $\delta(t)$ is Dirac's delta function. To produce a ratchet system, two additional elements are required. A force denoted by $U'(x)$ produced by a periodic potential:

$$U'_{\pm}(x) = \pm U_0 k \sin 2kx. \tag{3.4}$$

Additionally, a driving force denoted by $F(t)$, whose specific form will be defined in the next section, has to be introduced. Therefore, equation 3.1 turns into the following Langevin equation:

$$m\ddot{x} + \gamma\dot{x} = -U'(x) + F(t) + \zeta(t). \tag{3.5}$$

Three different regimes of ratchet dynamics can be studied in the system: Hamiltonian or dissipationless systems, for a zero damping coefficient $\gamma = 0$ and zero noise $\zeta(t)$, overdamped system in which the damping term in equation 3.5 is large and can dominate the inertial term $m\ddot{x}$ (i.e. $m = 0$) and underdamped system when the damping term is small compared to the inertial term.

3.5 Bi-harmonic driving force

The rocking ratchet scheme considered in this work is based on a temporally asymmetric bi-harmonic drive and a spatially symmetric periodic potential. The underlying mechanism of rectification is the so-called *Harmonic Mixing* [58]. The anharmonicity of the optical potential causes the medium to be nonlinear. Thus, it becomes able to mix the harmonics with frequencies ω_d and $2\omega_d$, with phase difference ϕ and to generate a current. This current is proportional to the sine of the relative phase ϕ between driving harmonics ($I \propto \sin\phi$) [23]. Basically, in harmonic mixing mechanism, all possible higher harmonics and their relative sum and difference are generated. When the driving frequencies are commensu-

rable ($i.e. n\omega_{d1} = m\omega_{d2}$), with n and m integer, the DC response also will appear [58, 102]. The driving force relevant to our experiment is given by [27]:

$$F_d(t) = F_0 \left[A \cos(\omega_d t) + B \cos(2\omega_d t + \phi)\right], \tag{3.6}$$

where F_0 is the overall amplitude of the driving force, $\omega_d = \frac{2\pi}{T}$ is the driving frequency, A and B are the driving force amplitudes and ϕ is the relative phase between the harmonics, which controls the symmetry of the system and therefore the generation of a current.

3.6 Symmetry analysis

In addition to the requirement of out of equilibrium settings, a ratchet has to possess a type of asymmetry to be able to generate a directed current. Symmetry analysis is the tool that is used to predict whether directed transport is possible or not. According to Curie's principle, generation of a current is expected when the system does not have any symmetry, which would prevent it. First, it is important to understand why the system symmetry prevents the generation of a directed current. The relevant quantity in each ratchet experiment is the particles current, which is the ensemble average velocity $\langle \dot{x} \rangle$ [83]. Generally, the system consists of an ensemble of identical particles whose dynamics follow the equation 3.5. When the system is symmetric, this means that the statistical weights of a trajectory with $x(t, x_0, p_0)$, $p(t, x_0, p_0)$ and the trajectory with $x(t, x_0, -p_0))$, $-p(t, x_0, -p_0)$, which has opposite velocity, are equal. Therefore, taking the average over the particles ensemble will give zero velocity and thus, no particle current is produced.
To analyse the symmetry of the ratchet system, we examine the conditions for the Langevin equation to be invariant under the inversion of x or t, so that the velocity is reversed. Characterising the relevant symmetries of equation 3.5 will then allow us to predict when no current occurs. To find the conditions for the invariance of the Langevin equation under inversion of the velocity, we consider the inversion of one variable, followed by a shift, and a shift of the other variable, in other words, the inversion in x with a time shift, or the inversion of the time t with a

position shift [19]. The transformations are:

$$x \to -x + x', \quad t \to t + t', \tag{3.7}$$

$$x \to x + x', \quad t \to -t + t', \tag{3.8}$$

where x', t' are constants. Generally, for a periodic function $f(x)$, three symmetries have to be considered.

- Symmetric function: $f(x + x') = f(-x + x')$. We say that the function possesses $\hat{f}_s$ symmetry.
- Antisymmetric function: $f(x + x') = -f(-x + x')$. The function is said to be possess $\hat{f}_a$ symmetry.
- Shift symmetric function: $f(x) = -f\left(x + \frac{L}{2}\right)$. The function changes its sign after half a period $L/2$. We say it possesses $\hat{\mathrm{f}}_{\mathrm{sh}}$ symmetry.

From Langevin equation 3.5, the asymmetry either comes from the potential $U(x)$, which is time independent, or the driving force $F(t)$, which is time dependent and spatially homogeneous. The transformations, under which the Langevin equation 3.5 is invariant, provided the listed conditions are satisfied, are the following [18]:

$$\begin{aligned}
&\hat{S}_a: \ x \to -x, && t \to t + \frac{T}{2}, && \text{if } \{U_a, F_{sh}\} \\
&\hat{S}_b: \ x \to x, && t \to -t, && \text{if } \{F_s, \gamma = 0\} \\
&\hat{S}_c: \ x \to x + \frac{L}{2}, && t \to -t, && \text{if } \{U_{sh}, F_a, m = 0\}
\end{aligned} \tag{3.9}$$

where T and L are the time period of the force and the spatial period of the periodic potential respectively. The Hamiltonian and the weakly damped regimes are of direct relevance to our experiment, and will be discussed in detail in the following chapter.

In the overdamped limit, the system possesses $\hat{\mathrm{U}}_{\mathrm{sh}}$ symmetry. Furthermore, for $\phi = n\pi + \frac{\pi}{2}$, the symmetry F_a holds and no current can occur. The atomic current in the overdamped ratchet has the form:

$$I \propto \cos\phi, \tag{3.10}$$

and indeed for $\phi = n\pi + \frac{\pi}{2}$ no atomic current is generated. The ratchet system in the overdamped limit is coined as supersymmetric [82]. For our rocking ratchet, only $\hat{S}_a$ and $\hat{S}_b$ are relevant since the atomic motion is never overdamped in a $lin\perp lin$ optical lattice because the damping of the atomic motion saturates due to the Sisyphus cooling limit [10].

3.7 Rocking ratchet for cold atoms

A rocking ratchet can be implemented experimentally by using an optical lattice [27, 88]. Optical lattices can be defined as periodic potentials produced by the interference of two or more laser beams. It was suggested for the first time when Letokhov proposed the possibility of cooling and confining the atoms in the potential wells by the dipole force that results from the light shift [63]. Later in 1987 [87], it was the first time that a study of a one dimensional optical lattice was published. Ever since, this topic has become important in controlling the atomic motion optically. The first cold atom ratchet was demonstrated in 1999 using cold atoms in a spatially asymmetric undriven optical lattice [64]. Later in 2006 and 2007 [34, 91], two experiments were reported for an undriven optical lattice in a spatially symmetric and shifted potential. More details about optical lattices can be found in Ref. [31].

Dissipative optical lattice As explained in section 1.2, the laser beams configuration of the $lin\perp lin$ optical lattice creates a spatial modulation of the laser field polarisation. By interacting with the atomic states, a periodic modulation of the light shift of the ground state sublevels is produced. For this configuration, the interaction between the laser fields and the atoms reduces the kinetic energy and then localises the atoms in the optical potential as shown in the figure 1.3 in chapter 1.

The optical lattice configuration used in our experiment is the one dimensional $lin\perp lin$ configuration. This optical lattice results from two counter-propagating laser beams with the same frequency ω and intensity I, and with orthogonal linear polarisations. In order to derive the optical potential, the transition $J = 1/2 \rightarrow J' = 3/2$ will be considered for simplicity. The electric field for both laser beams propagating in the

z direction, with a constant amplitude E_0 and frequency ω is given by the equations:

$$\vec{E_1}(z,t) = \frac{1}{2}\vec{\epsilon_x}E_0 \exp i\,(kz - \omega t) + c.c. \tag{3.11}$$

$$\vec{E_2}(z,t) = \frac{1}{2}\vec{\epsilon_y}E_0 \exp i\,(-kz - \omega t + \phi) + c.c. \tag{3.12}$$

where $\vec{\epsilon}_x$, $\vec{\epsilon}_y$ are the linear polarisation vectors, which are perpendicular to each other, along the x and y axes, $k = \frac{2\pi}{\lambda}$ is the wave number, $\omega = kc$ is the angular frequency and ϕ is the relative arbitrary phase between both beams' field. The superposition of the electric fields 3.11 and 3.12 creates the optical potential. The total electric field E_L incident on the atoms can be given as:

$$\vec{E_L} = \frac{E_0}{2}\left[\vec{\epsilon_x}\exp i\,(kz - \omega t) + \vec{\epsilon_y}\exp -i\,(kz + \omega t + \phi)\right] + c.c. \tag{3.13}$$

We notice that varying the phase in equation 3.13 does not change the potential topography. It just induces a spatial translation of the lattice. As it will be discussed in the following, this can be used to apply a force. In the present derivation of the potential, the relative phase ϕ can be eliminated $\left(e^{-i\phi} = 1\right)$. After using Euler's formula[1], the total light field becomes:

$$\vec{E_L} = \frac{E_0}{\sqrt{2}}\exp(-i\omega t)\left[\vec{\epsilon_-}\cos kz - i\vec{\epsilon_+}\sin kz\right], \tag{3.14}$$

which can be written as:

$$\vec{E}_L = \exp(-i\omega t)[E_+(z)\vec{\epsilon}_+ + E_-(z)\vec{\epsilon_-}] + c.c. \tag{3.15}$$

where $\vec{\epsilon_\pm} = \mp\frac{1}{\sqrt{2}}(\epsilon_x \pm i\epsilon_y)$ are the circular polarisation unit vectors that results from the superposition of both linear polarisations in the x and y direction, and E_+ and E_- are given as:

$$E_+ = -i\frac{E_0}{\sqrt{2}}\sin kz, \tag{3.16}$$

and

$$E_- = \frac{E_0}{\sqrt{2}}\cos kz. \tag{3.17}$$

[1]Euler's formula is $e^{i\theta} = \cos\theta + i\sin\theta$ and $e^{-i\theta} = \cos\theta - i\sin\theta$

Equation 3.14 shows that the total laser field has a constant intensity and variable polarisation whose ellipticity changes as a function of the position z in the lattice. As was presented in figure 1.3, the polarisation of the light field changes from σ^- polarisation at $z = 0$ into linear polarisation at $z = \lambda/8$. Then, at $z = \lambda/4$, the polarisation returns into circular with σ^+ and so on. When the atom travels through the optical lattice, it experiences a sinusoidal potential. As mentioned in chapter 1, the coupling between the atom and the light field leads to the light shift which can be evaluated easily for a two levels atom with transition $J = 1/2 \rightarrow J' = 3/2$. The light shifts $U_\pm$ for the ground state sublevels $|g, +1/2\rangle$ and $|g, -1/2\rangle$ can be shown to be given by [31]:

$$U_\pm = 2\hbar\acute{\Delta}_0(\frac{I_L^+}{I_L} + \frac{I_L^-}{3I_L}), \tag{3.18}$$

where $I_L^\pm$ represent the intensities of the laser beam with left and right polarisation and the total intensity is $I_L = I_L^- + I_L^+$, $\acute{\Delta}_0$ is the light shift per beam of the closed atomic transitions, and is given by:

$$\acute{\Delta}_0 = \frac{\Delta s}{2}, \tag{3.19}$$

after substituting the saturation parameter s from equation 1.2, equation 3.19 yields:

$$\acute{\Delta}_0 = \Delta\frac{\Omega^2/4}{\Delta^2 + \Gamma^2/4}, \tag{3.20}$$

where $\Delta = \omega - \omega_0$ is the detuning of the optical lattice beam from atomic resonance, Ω is the Rabi frequency and Γ is the atomic transition linewidth. The value of $U_\pm$ represents the optical potential corresponding to the light shift of $\left|g, \pm\frac{1}{2}\right\rangle$ Zeeman sublevels. By substituting the intensity of the left and right polarisation beams with $I_L^\pm = |E^\pm|^2$ from 3.16 and 3.17, and using trigonometric identities, the expression for the optical potential can be written as:

$$U_\pm = \frac{U_0}{2}[-2 \pm \cos 2kz], \tag{3.21}$$

where

$$U_0 = -\frac{4}{3}\hbar\acute{\Delta}_0, \tag{3.22}$$

is the depth of the potential wells. The anharmonic potential can be approximated by an harmonic oscillator. Therefore, the vibrational frequency ω_v can be determined as:

$$\omega_v = \frac{2\sqrt{E_r U_0}}{\hbar}, \tag{3.23}$$

where E_r is the recoil energy of the atoms $E_r = \hbar\omega_r$ with ω_r is the recoil frequency and U_0 is the potential depth represented by the light shift of the atomic sublevels.

To sum up, the polarisation gradient of the optical lattice configuration produces the light shift modulation of the ground state sublevels. This acts as a periodic optical potential which is the main ingredients of the rocking ratchet. This optical potential can be characterised by the their depth, given in 3.22, and the vibrational frequency, given in 3.23. However, the periodic potential here is symmetric, thus a bi-harmonic driving force, introduced in section 3.5, has to be applied to introduce an asymmetry in the system. It also serves the purpose of driving the system out of equilibrium. Experimentally, the force is applied by modulating the frequency of one of the lattice laser beams. This will be discussed in detail in the next two chapters. The optical lattice system is a unique system because it can be precisely tuned by varying the laser parameters. It is also a defect free system compared to the other ratchet types.

Chapter 4

Current reversals in a rocking ratchet

This chapter describes the results of my first experiment on current reversals in a rocking ratchet which have been published in [97].

4.1 Introduction

Current reversals are an intriguing feature of the rocking ratchet. Current reversals are changes in the direction of the current due to a change of a system parameter, such as, the amplitude and frequency of the driving force or the noise strength in the rocking ratchet system [4, 43, 61]. Current reversals have an important application in constructing particle separation devices which can separate particles with different sizes or mass [43, 86]. An early numerical study in 1994 was done on a rocking ratchet system with an asymmetric potential and a symmetric driving force. A current reversal was observed when the noise strength was varied at constant amplitude of the driving force. A current reversal was also observed when the force amplitude was varied with fixed noise strength [4].

Another theoretical study, by Mateos [61] in 2000 aimed to understand the mechanism behind the current reversals in rocking ratchets. Mateos tried to relate the origin of the current reversal in a chaotic deterministic rocking ratchet to the bifurcation from the chaotic to the periodic regime. Mateos analysis was based on the comparison between the current and

the bifurcation diagram[1] as obtained by varying the driving force amplitude. The behaviour just before and after the occurrence of a current reversal was then examined. This investigation interpreted the current reversals as a dynamical effect. However, such a claim was refuted by Barbi and Salerno [3] and Kenfack et al. [46]. They showed that the current reversals do not always correspond to transitions from chaotic to periodic regimes in the bifurcation diagram.
Later, in 2010, a study done by our group [14] addressed the origin of the current reversals in a rocking ratchet from a completely different point of view. It was shown that the current reversals in such a system are determined by dissipation-induced symmetry breaking. This, therefore, suggests a link between current reversals and a symmetry breaking mechanisms. Therefore, it is not possible to observe the current reversals in the Hamiltonian and overdamped limits. To generalise this result, I investigated the link between current reversals in the frequency domain and dissipation-induced symmetry breaking. I conducted an experiment on the same rocking ratchet system examined previously but by varying the driving frequency of the bi-harmonic force to observe the current reversals. The experimental work was supported by a numerical analysis done by our collaborator Dr.Cubero [97]. The experimental setup, experimental results and theoretical analysis will be described in the following sections of the present chapter.

4.2 Ratchet setup and symmetries

Ratchet setup Our experimental setup of the rocking ratchet system consists of Brownian particles, represented by ^{87}Rb atoms, in a spatially symmetric periodic potential driven by a time asymmetric bi-harmonic force. The system dynamics is described by the Langevin equation given in 3.5. To be able to investigate, theoretically, different damping and noise regimes, the case of a linear friction γ is considered in the Langevin equation. The periodic symmetric potential is generated by a 1D optical

[1]The bifurcation diagram is a plot used to study a system dynamics described by a differential equation, the equation of motion in our case, which depends on the value of one of its parameters, such as a driving force amplitude, by distinguishing between two regimes: periodic and chaotic.

lattice and is given by the equation 3.4. The asymmetry is introduced into the system by the bi-harmonic force which is given by equation 3.6.

Symmetries The analysis of the ratchet setup used in our experiment requires first the examination of the system symmetries. As discussed in section 3.6, the current occurs when the system does not have any symmetry which would otherwise prevent the generation of directed motion. Therefore, finding conditions for the Langevin equation to be invariant is essential to predict when the atomic current can be generated. These symmetries will then be used to establish the link between the current reversals in the frequency domain and dissipation-induced symmetry breaking. For the spatially symmetric potential under consideration, there are two symmetries which have to be broken in order to generate a current: the shift symmetry and the time reversal symmetry. Both symmetries were introduced in chapter 3. The bi-harmonic force given in equation 3.6 is used to drive the system out of equilibrium as well as to break the system symmetry. This force breaks the shift symmetry regardless of the relative phase ϕ value between the harmonics. For the time reversal symmetry, two distinct cases have to be considered, depending on both the phase ϕ and the dissipation level:

- In the dissipationless case or Hamiltonian ($\gamma = 0$), the system is invariant under the time reversal symmetry for $\phi = n\pi$, with n an integer number. Consequently, directed motion cannot be generated [23]. It was shown by Flach et al. [23] and Quintero et al. [80] that, in leading order, the atoms' average velocity has a sinusoidal dependence on the relative phase ϕ between the harmonics of the driving force, i.e.:

$$\langle v \rangle = v_{max} \sin \phi. \tag{4.1}$$

  This was also discussed in section 3.5 in the context of the analysis of the harmonic mixing mechanism which determines directed motion in the case of a bi-harmonic drive.

- In case of non zero dissipation, dissipation breaks the time reversal symmetry even for $\phi = n\pi$ and may lead to directed motion. In the weak dissipation case, the velocity has also sinusoidal dependence

on the phase ϕ but with an additional phase shift (phase lag) ϕ_0 [80] as, i.e.:

$$\langle v \rangle = v_{max} \sin(\phi + \phi_0). \tag{4.2}$$

The phase lag ϕ_0 is determined by dissipation. In the Hamiltonian limit, the phase lag vanishes since there is no dissipation [26]. In the over-damped regime, in which the damping term γ dominates the inertia term m in equation 3.5, the phase lag becomes $\phi_0 = -\pi/2$. The system is invariant under the transformation S_c given in equation 3.9 whenever $\phi = \frac{\pi}{2} + n\pi$, and thus the generation of atomic current is forbidden for these values of ϕ.

4.3 Experimental setup

The experimental setup for the study of current reversals in a rocking ratchet is shown in figure 4.1. A 1D $lin \perp lin$ optical lattice configuration is used to create the optical potential. The optical lattice laser beams are generated from a diode laser injected by the master laser with detuning $-6\Gamma \leq \Delta \leq +2\Gamma$, as described in 2.2.2. A polarising beam splitter is used to split the laser beam into two beams to form the optical lattice. Each beam passes through an AOM to shift the frequency by 80 MHz to produce $\Delta = -9\Gamma$ detuning from the atomic resonance. In addition, the AOM is also used to control the beam intensity, switching the beam and applying the bi-harmonic drive. The intensity for each lattice beams is set to $(43.5 \pm 0.3)\,\mathrm{mW/cm^2}$ per beam. Both AOMs are driven by function generators[2]. The rocking force is applied via frequency modulation. It is produced by two sinusoidal signals from two phase-locked function generators[3]. Their frequencies are in a 1:2 ratio. The signals are added electronically by an electronic circuit using an analogue multiplier[4] and multiplied by an envelope function[5] to be able to switch on the modulation adiabatically and thus avoid any directed motion of the atoms

[2]Signal Generator 9 kHz- 1.040 GHz from Rohde & Schwarz.

[3]3220A, 20 MHz Function/Arbitrary Waveform Generator from Agilent Technologies.

[4]AD633 from Analog Devices

[5]The envelop function is a constant signal generated by the program of the computer control via the analogue card and then multiplied to the modulation amplitude. This signal used as a ramp of the modulation.

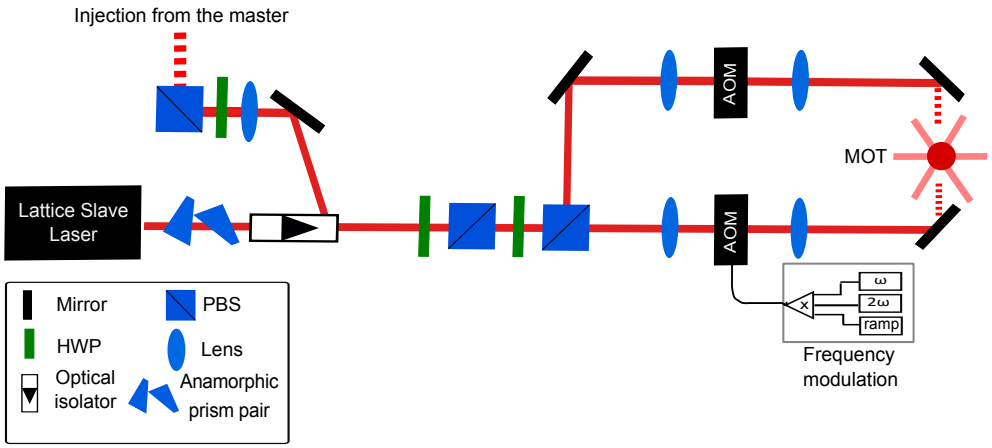

Figure 4.1: Experimental schematic for the 1D *lin* ⊥ *lin* optical lattice setup used to investigate the current reversals. The optical lattice laser is a diode laser injected by the master laser (details in 2.2.2). The laser beam passes through an anamorphic prism pair to transform the beam profile from elliptical into circular. An optical isolator is used to protect the lattice laser and inject it by sending a fraction of the master laser beam back to the lattice slave laser. The lattice beams are produced by splitting the main laser beam with a polarising beam splitter which is placed after a half wave plate to balance the power of the lattice beams. Then, each beam passes through an AOM to control their frequency and intensity. The frequency of one of the lattice beam is modulated by the multiplied signal (the bi-harmonic and the ramp signals).

due to the sudden kick. The signal generated in this way is sent to the frequency modulation input of one of the AOM drivers. By modulating the frequency of the AOM of one of the lattice beams, a time-dependent homogenous force is applied to the optical lattice. The accelerated frame, in which the optical lattice is stationary, is defined by $\tilde{x} = x - \frac{\alpha(t)}{2k}$ where $\alpha(t)$ is the phase modulation. In the moving frame of the optical lattice, the atom is subjected to an inertial force $F(t)$ which is given by:

$$F(t) = -ma(t) = \frac{m}{2k}\ddot{\alpha}. \tag{4.3}$$

The bi-harmonic driving used here for the phase modulation is of the form:

$$\dot{\alpha} = -A_\nu \left[A \sin(\omega_d t) + 2B \sin(2\omega_d t + \phi)\right], \tag{4.4}$$

where A_ν is the modulation amplitude in kHz/V. Therefore, the frequency modulation has the following form:

$$\ddot{\alpha} = -A_\nu \omega_d \left[A \cos(\omega_d t) + 4B \cos(2\omega_d t + \phi)\right], \tag{4.5}$$

By substituting 4.5 in 4.3, the applied force on the atoms in the accelerated frame will be:

$$F(t) = -\frac{m}{2k}\omega_d A_\nu \left[A\cos(\omega_d t) + 4B\cos(2\omega_d t + \phi)\right]. \tag{4.6}$$

The total amplitude F_0 of the force in equation 4.6 applied to an atom, is:

$$F_0 = -\frac{m}{2k}(2\pi)^2 A_\nu f_d U_{FG}, \tag{4.7}$$

where f_d is the modulation frequency in Hz, U_{FG} is the peak to peak voltage applied by the function generator. F_0 can be written as:

$$F_0 = -m\lambda g_0, \tag{4.8}$$

where λ is the wave length of the laser light and g_0 in units kHz^2 is given by:

$$g_0 = A_\nu f_d U_{FG}. \tag{4.9}$$

In the experiment, it is important to keep the amplitude of the modulation force constant when changing the driving frequencies. This is done by controlling the amplitude of the frequency modulation. The control parameters of the experimental sequence are given in figure 4.2. The experimental sequence starts with loading ^{87}Rb atoms for 3 s in a magneto-optical trap to trap up to 10^8 atoms, as measured by the fluorescence of the MOT with a photodiode, and cool them down to $\approx 50\,\mu$K. To ensure the experimental parameters are applied by the experimental control at the desired time, an appropriate delay time due to the finite time response of shutters and magnetic coils, has to be introduced. Specifically, after switching off the current of the MOT's coils, 50 ms delay is required before loading the lattice beams. Then, the MOT's beams are turned off and the 1D $lin\perp lin$ optical lattice is loaded, by switching the AOMs controlling the lattice beams on. The atoms are left in this undriven lattice for 2 ms which is sufficient for the atoms to thermalise. After that the frequency modulation of the optical lattice is turned on slowly with 1 ms ramp up time. This is initially done by ramping the modulation amplitude up linearly and then the modulation is kept to the full amplitude for 8 ms. This time is optimised for efficient imaging and it is used with the measurements of the cloud's centre of mass to

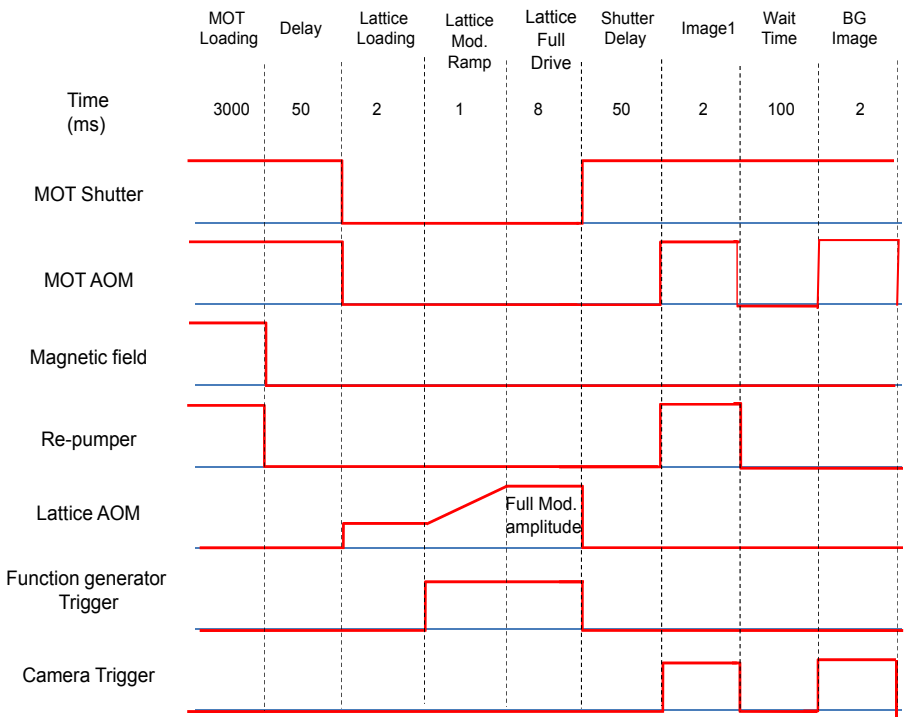

Figure 4.2: Experimental time sequence for the investigation of current reversals.

calculate the atom velocity. The cloud fluorescence was imaged with a CCD camera[6]. The MOT's beams shutter is opened 50 ms before imaging the cloud in order to compensate for the mechanical shutter response time. A first image is taken with the MOT light on. Then, a second image is taken after 100 ms time and then subtracted from the first image to remove the background. The subtracted image was fitted with a 2D Gaussian and the fitting parameters were saved in a file to calculate and derive the velocity of the atomic cloud. Many images were taken for the same modulation strength value and averaged later to reduce the error.

4.4 Experimental results

Current reversals are a characteristic feature of the rocking ratchet. The purpose of this experiment is to study the behaviour of the current reversals as a function of experimental parameters. The first experiment

[6]AVT Guppy F038B NIR

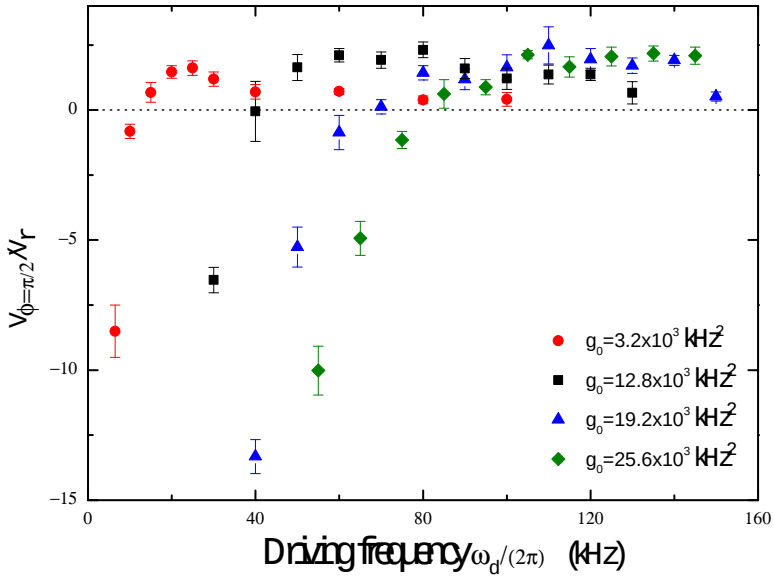

Figure 4.3: The atomic velocity, rescaled by the recoil velocity of the ^{87}Rb, as a function of the driving frequency ω_d for fixed value of the relative phase $\phi = \pi/2$ between the harmonics of the bi-harmonic driving. The data were taken for four different force amplitudes g_0 and the current reversals are observed clearly for all of them.

examined the atom current as a function of the driving frequency of the bi-harmonic modulation. The relative phase is fixed to $\phi = \pi/2$ so that the Hamiltonian time symmetry is maximally broken [28, 42]. This allows us to study the current as a function of the driving frequency. The ratio between the harmonics was kept constant $A/B = 1/2$. After applying the bi-harmonic driving, the velocity of the atoms in the lattice can be measured from the centre of mass displacement. The experiment was conducted for different force amplitudes. For each force amplitude, the atom velocity was measured as a function of the driving frequency of the bi-harmonic force. The amplitude of the force on the atoms has to be kept constant to observe the effect of varying the driving frequency. This was done by adjusting the driving amplitudes so to maintain the force amplitude (Eq. 4.9) constant. As can be seen from figure 4.3, our results show that the direction of the atomic current can be controlled by changing the driving frequency.

A second experiment was conducted to establish the link between the

current reversals and dissipation. This was done by studying the atomic current as a function of the relative phase between the harmonics of the bi-harmonic driving. The observed behaviour of the current is shown in figure 4.4 for the force modulation amplitude of $g_0 = 19.2 \times 10^3\,\mathrm{kHz}^2$, and different driving frequencies. As expected, the observed behaviour is well described by equation 4.2.
More data sets were taken for different force amplitudes and all show the same behaviour. By fitting the sinelike curves with the function 4.2, the maximum velocity amplitude v_{max} and the dissipation-induced symmetry-breaking phase lag ϕ_0 can be extracted. These are reported in figure 4.5. It can be seen from the right graph of figure 4.5 that the amplitude is always finite around the reversal frequency, i.e. the frequency where the direction of the atomic current is inverted. The relation between the phase lag ϕ_0 and the driving frequency is shown in the left graph of figure 4.5. It appears that the phase lag varies between $-\pi$ and 0 across the current reversals. Since the relative phase between the harmonics was fixed at $\pi/2$, therefore, as shown in 4.2, for phase lag $-\pi/2$, the current will vanish at the corresponding reversal frequency. In summary, a large variation of the dissipation-induced symmetry-breaking phase lag ϕ_0 around the reversal frequency determines the current reversals in the frequency domain. This result generalises the link between symmetry breaking and current reversals which was established previously for reversals in the amplitude domain [14].

Our experimental setup is only suitable for the weakly damped regime. Investigating the Hamiltonian and the overdamped regimes is required to fortify our results. However, these regimes are not accessible experimentally. Therefore, this was done numerically by Dr. Cubero. In the Hamiltonian and the overdamped regimes, the phase lag is fixed to $\phi_0 = 0$ and $\phi_0 = -\pi/2$ respectively. Thus, variation in the driving frequency should not produce current reversals. The middle panel of figure 4.6 presents the numerical analysis relevant to our experimental implementation of the weakly damped regime. The average atomic velocity is shown as a function of the relative driving phase for three different driving frequencies. Current reversals are observed at about $\phi = \pi/2$ or $\phi = 3\pi/2$ with increasing driving frequency as a result of the variation of the phase lag ϕ_0, in agreement with our experimental findings.

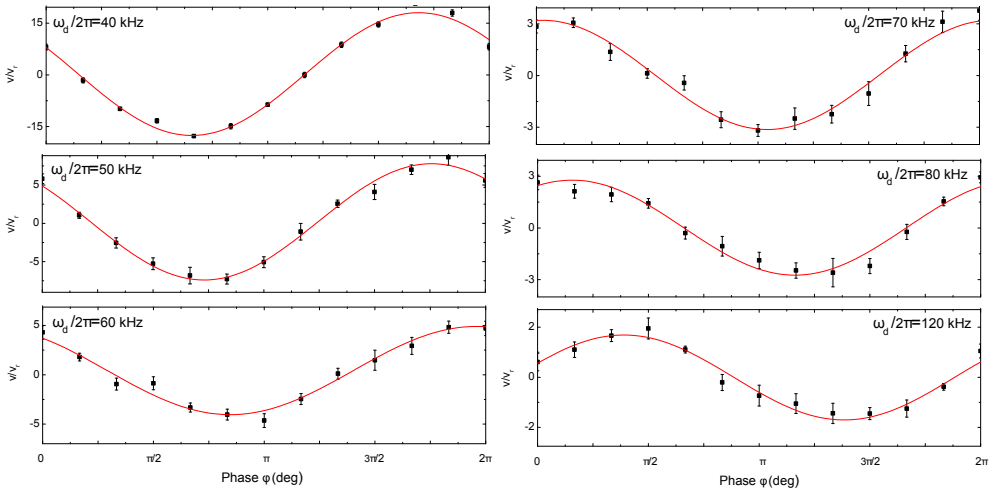

Figure 4.4: The atomic average velocity as a function of the relative phase between the harmonics of the bi-harmonic driving for different drive frequencies $\omega_d/2\pi$. The data were taken for different force amplitudes but it is shown here only for $g_0 = 19.2 \times 10^3\,\mathrm{kHz}^2$ as an example. The red lines are the best fit of the data with the function 4.2. The variation of the dissipation-induced phase lag with increasing drive frequency is clearly visible.

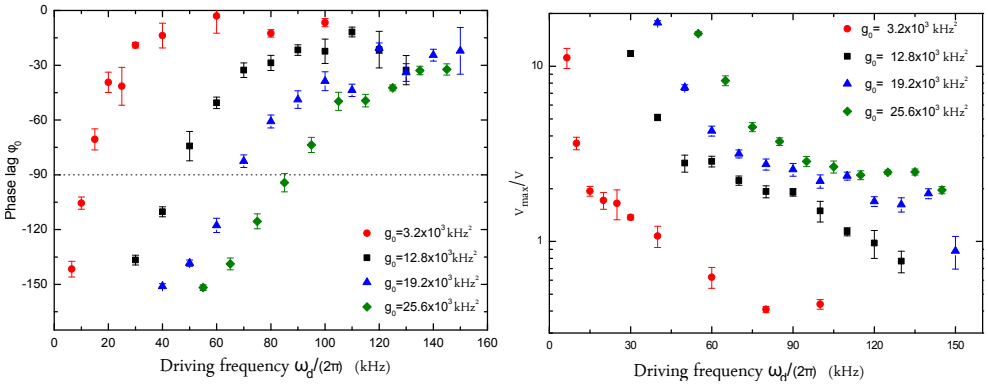

Figure 4.5: Phase lag ϕ_0 and atomic current amplitude v_{max}, obtained from the fit results of the data as those shown in figure 4.4, as functions of the driving frequency. The data were taken for different force amplitudes g_0. The left graph shows the dissipation-induced symmetry breaking phase lag as a function of the drive frequency. The phase lag shows a substantial variation between $-\pi$ and 0 across the current reversals. At $\phi_0 = -\pi/2$ phase lag, the current vanishes as the relative phase is fixed to the value $\phi = \pi/2$ and then inverts its sign. The right graph shows the maximum amplitude of the atomic velocity as a function of the drive frequency. The amplitude is always finite around the reversal frequency, where the current vanishes and then inverts its direction.

Current reversals are not observed in the Hamiltonian (upper panel) and the overdamped (lower panel) regimes. In these regimes, increasing the driving frequency results only in a variation of the current amplitude.

Therefore, the numerical analysis confirms the established link between the current reversals in the frequency domain and dissipation-induced symmetry breaking.

4.5 Summary

This chapter presented the experiment conducted to examine the mechanism behind the current reversals in a rocking ratchet. The ratchet system implemented in the experiment used cold ^{87}Rb atoms in a spatially symmetric potential driven by a time-dependent asymmetric force, and specifically a bi-harmonic driving force. The current reversals were investigated by varying the driving frequency. It is observed that a class of current reversals is determined by dissipation-induced symmetry breaking. This link was established previously by our group [14] in the amplitude domain. Our results generalised the established link to the frequency domain. Our experiment was complemented by numerical simulation, which also explored the Hamiltonian and overdamped regimes. It was found that current reversals are only observed in the weakly damped regime. Current reversals do not appear in the Hamiltonian or in the overdamped regimes.

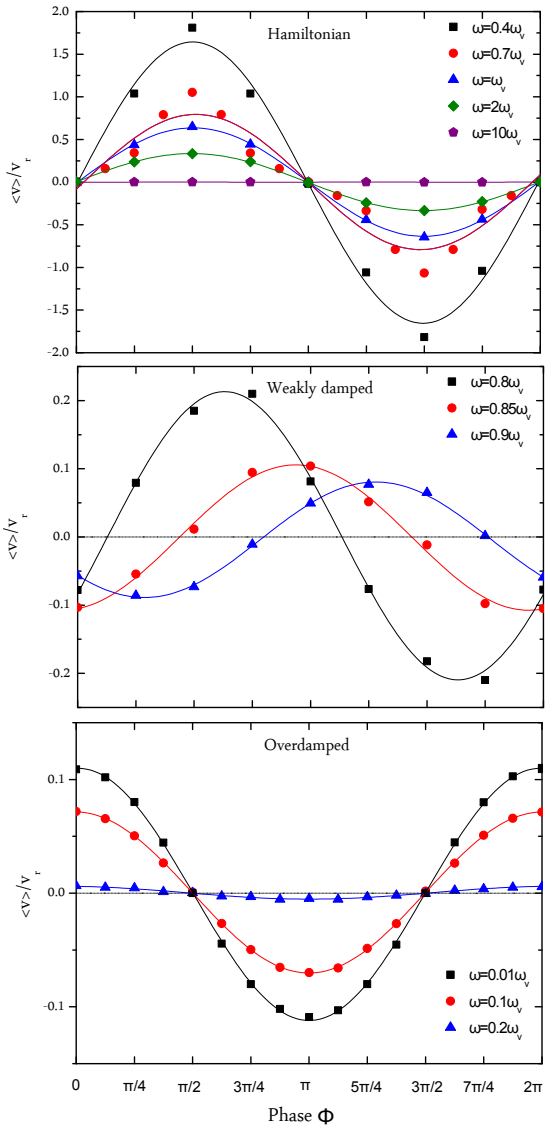

Figure 4.6: Numerical simulation of the average atomic velocity as a function of the phase between harmonics of the bi-harmonic force for different driving frequency values ω_d, with $\omega_v = k\,(2U_0/m)^{1/2}$ and $A_1 = A_2 = 1$. The top panel shows the atomic current behaviour in the Hamiltonian regime. The force amplitude is $F_0 = 0.2U_0k$ where U_0 is the potential depth created by optical lattice. The middle panel shows the weakly damped regime in which the numerical parameters are fixed to the following parameters: the force amplitude is $F_0 = 0.2U_0k$, the friction coefficient $\alpha = 0.15\alpha_0$ and the noise strength $D = 1.944D_0$ where $\alpha_0 = mk\nu_0$, $D_0 = {\alpha_0}^2 v_0/k$ and $v_0 = (U_0/m)^{1/2}/10$. The lower panel shows the overdamped regime for a force amplitude $F_0 = U_0k$, $\alpha = 100\alpha_0$ and $D = 1.944 \times 10^3 D_0$. In the weakly damped case, numerical data were obtained in the framework of a simple model with linear friction, so the values of the velocity cannot be directly compared with the experimental ones. The lines are the best sine fit to the data.

Chapter 5

Vibrational mechanics in an optical lattice: controlling transport via potential renormalisation

This chapter presents my work on vibrational mechanics as investigated using a dissipative optical lattice with cold ^{87}Rb atoms. The results have been published in [98].

5.1 Introduction

In recent years, a lot of effort has been devoted to investigate the possibility of controlling atomic currents in periodic potentials by applying DC or AC fields [35, 83]. Here, we present a method for tuning the amplitude of a periodic potential exclusively by using an externally applied high frequency (HF) modulation. Its frequency has to be much larger than any other characteristic frequency of the optical lattice system. The periodic potential is renormalised and the renormalised potential depth becomes a function of the HF modulation amplitude. The potential amplitude follows a first order Bessel function with the modulation strength as argument and therefore the potential vanishes at specific strengths of the high frequency force, and recovers again multiple times. The mechanism behind this potential renormalisaton is called *vibrational resonance*. It

was introduced in 2000 for a bistable system [49] and the first experimental evidence was reported in 2003 [11]. This topic could be of particular interest in solid state materials where the tuning of the periodic potential is difficult if not impossible. Even though we demonstrated this effect with cold ^{87}Rb atoms in a dissipative optical lattice, it is a very general phenomenon and could be implemented in any other system with a periodic potential. The dissipative optical lattice is a very convenient system to study the transport and the potential properties under a high frequency drive because all its parameters are very well understood and controllable [31]. This chapter describes the vibrational resonance phenomenon. It starts with an introduction to the Kapitza pendulum to gain some intuition about vibrational mechanics. Then, after a brief discussion of the experimental setup our experimental results are presented.

5.2 Kapitza pendulum

A normal undriven pendulum is in its stable position when the potential energy is minimised. The centre of mass of the pendulum is below the pivot point and oriented along the direction of gravity. However, if an amplitude modulation is applied to the pivot point with a frequency much larger than the natural frequency of the pendulum, another stable position arises above the pivot point. This kind of dynamic behaviour was first investigated theoretically in 1908 by Stephenson. Then, in 1951, it was demonstrated experimentally by the Russian Nobel prize laureate Pyotr Kapitza, who also developed the theory explaining this phenomenon. The physical device is now known as *Kapitza pendulum* or *normalised* or *inverted pendulum*. The vibration creates a new potential energy minimum making the inverted pendulum stable for a range of natural frequencies and oscillating amplitudes. Those are exclusively determined by the high frequency driving parameters [33]. This counterintuitive behaviour can be easily understood by analysing the Lagrangian of the driven system. It is common to introduce a new set of variables incorporating the driving of the pivot point. The orientation of the coordinate system can be seen in figure 5.1. The position of the pendulum in the xy plane is:

$$x = l \sin \theta, \tag{5.1}$$

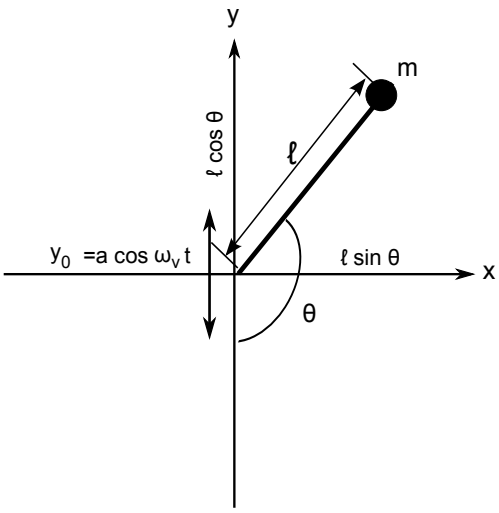

Figure 5.1: The Kapitza pendulum is a non-linear pendulum with mass m and length l. Its centre of mass is above the pivot point. An undriven inverted pendulum is unstable. Without support, it will orient itself along the direction of gravity (y axis) below the pivot point. The potential energy is minimised and the position is stable. Applying now a high frequency modulation of the form $y_0 = a\cos\omega_v t$ with frequency ω_v and amplitude a, the centre of mass of the pendulum can stabilise above the pivot point as well.

$$y = -l\cos\theta - a\cos\omega_v t, \tag{5.2}$$

where l is the pendulum length, θ is the angle between the pendulum and the axis along gravity. Here a and ω_v are the amplitude and the frequency of the pivot point vibration respectively. The second term of equation 5.2 represents the vertical harmonic oscillation $y_0(t) = -a\cos\omega_v t$ of the pivot point. In order to obtain the kinetic energy $E_k = \frac{m}{2}(\dot{x}^2 + \dot{y}^2)$, we find the derivatives of 5.1 and 5.2 to be:

$$\dot{x} = l\dot{\theta}\cos\theta, \tag{5.3}$$

$$\dot{y} = l\dot{\theta}\sin\theta + a\omega_v\sin\omega_v t, \tag{5.4}$$

then the kinetic energy becomes:

$$E_K = \frac{ml^2\dot{\theta}^2}{2} + mal\omega_v\sin(\omega_v t)\,\dot{\theta}\sin(\theta) + \frac{ma^2\omega_v^2}{2}\sin^2(\omega_v t)\,. \tag{5.5}$$

The potential energy is $E_P = mgy$, with g being the gravitational constant. Inserting the expression for the driven y-coordinate, we get:

$$E_P = -mg\,(l\cos\theta + a\cos\omega_v t)\,. \tag{5.6}$$

Combining equations 5.5 and 5.6 in the Lagrangian $L = E_K - E_P$ we obtain the following:

$$\begin{aligned} L = &\frac{ml^2\dot{\theta}^2}{2} + mal\omega_v \sin(\omega_v t)\,\dot{\theta}\sin(\theta) + \frac{ma^2\omega_v^2}{2}\sin^2(\omega_v t) \\ &+ mgl\cos(\theta) + mga\cos(\omega_v t)\,. \end{aligned} \tag{5.7}$$

The expression for L can be simplified by noticing that:

$$\sin(\omega_v t)\sin(\theta)\,\dot{\theta} = \omega_v \cos(\omega_v t)\cos(\theta) - \frac{d}{dt}\left[\sin(\omega_v t)\cos(\theta)\right], \tag{5.8}$$

and then dropping total time derivative terms. Equation 5.7 is then rewritten as:

$$L = \frac{ml^2\dot{\theta}^2}{2} + ml\cos\theta\left(g + a\omega_v^2\cos\omega_v t\right). \tag{5.9}$$

The angle θ from equation 5.9 is the only degree of freedom in this Lagrangian. The equation of motion is then given by the Euler-Lagrange equation:

$$\frac{\partial L}{\partial\theta} - \frac{d}{dt}\left(\frac{\partial L}{\partial\dot{\theta}}\right) = 0. \tag{5.10}$$

Inserting 5.9 into 5.10 leads to:

$$-ml\left(g + a\omega_v^2\cos\omega_v t\right)\sin\theta - \frac{d}{dt}\left(ml^2\dot{\theta}\right) = 0. \tag{5.11}$$

Re-arrangement of the terms in equation 5.11 gives the solution:

$$\ddot{\theta} = -\frac{\sin\theta}{l}\left(g + a\omega_v^2\cos\omega_v t\right). \tag{5.12}$$

The key to understand the inverted dynamics of Kapitza's pendulum is to separate the different time scales. One slow component θ_0, represents the slow variation of the angle of the pendulum. The other component, ξ, is the rapidly oscillating component due to the driving of the pivot point. The overall angle θ is given by:

$$\theta = \theta_0 + \xi. \tag{5.13}$$

Thus, the equation of motion 5.12 of the driven pendulum becomes:

$$\ddot{\theta} = \ddot{\theta_0} + \ddot{\xi} = -\frac{g \sin(\theta_0 + \xi)}{l} - \frac{a\omega_v^2}{l} \sin(\theta_0 + \xi) \cos(\omega_v t). \tag{5.14}$$

To derive an expression for ξ, we consider the limit of small amplitude ξ. By integrating twice the equation $\ddot{\xi} = -\frac{a\omega^2}{l} \sin\theta_0 \cos(\omega_v t)$, we obtain:

$$\xi = \frac{a}{l} \sin\theta_0 \cos\omega_v t, \tag{5.15}$$

Combining equation 5.12 and the second derivative of equation 5.15 we get $\ddot{\theta_0} = \ddot{\theta} - \ddot{\xi}$. A Taylor approximation[1] of $\sin(\theta_0 + \xi)$ leads to the following:

$$\begin{aligned} \ddot{\theta_0} = -\frac{g}{l} \sin\theta_0 - \frac{\xi \cos\theta_0}{l} \left(g + a\omega_v^2 \cos\omega_v t\right) \\ -\frac{a}{l} \left[\ddot{\theta_0} \cos\omega_v t \cos\theta_0 - \dot{\theta_0}^2 \sin\theta_0 \cos\omega_v t - 2\dot{\theta_0}\omega_v \cos\theta_0 \sin\omega_v t\right]. \end{aligned} \tag{5.16}$$

After averaging over one period of the rapid oscillation, and re-arranging the terms of equation 5.16, the equation of motion of the slow component is given by:

$$\ddot{\theta_0} = -\frac{g}{l} \sin\theta_0 - \frac{1}{2} \left(\frac{a\omega_v^2}{l}\right)^2 \sin\theta_0 \cos\theta_0. \tag{5.17}$$

This equation describes the movement of the centre of mass of the pendulum in an effective potential U_{eff}:

$$ml^2 \ddot{\theta_0} = -\frac{\partial U_{eff}}{\partial \theta_0}. \tag{5.18}$$

where:

$$U_{eff} = -mgl \cos\theta_0 + m \left(\frac{a\omega_v \sin\theta_0}{2}\right)^2. \tag{5.19}$$

The first term of equation 5.19 results from gravity. The second term represents the renormalisation of the potential by the fast oscillating field. If the oscillating force exceeds the gravitational force, i.e. the condition:

$$\frac{a^2\omega_v^2}{4gl} > \frac{1}{2}, \tag{5.20}$$

[1] $\sin(\theta_0 + \xi) \approx \sin\theta_0 + \xi \cos\theta_0$.

is fulfilled, the inverted position of the pendulum will be stable. One can see from equation 5.19 that the effective potential U_{eff} possesses two minima. One minimum corresponds to a new equilibrium position in the inverted pendulum, which appears as a result of the fast oscillating force. This is in agreement with the condition 5.20. The other minimum corresponds to the other stable position in the normal pendulum with 5.20 less than 1/2 [40].

5.3 Model and definitions of the potential renormalisation

We say that an optical potential is renormalised by a high frequency field when its amplitude and the other spatially dependent parameters become a function of the amplitude of the applied fast modulation. As we will see, for specific values of this amplitude the potential can even disappear completely and reappears when the amplitude is increased. To understand this effect for the case of atoms in an optical lattice, we have to look at the Fokker-Planck equation used to describe the atomic dynamics in a 1D $lin\perp lin$ optical lattice with the simple transition $J = 1/2 \longrightarrow J' = 3/2$. The probability density of an atom inside an optical lattice $P_{\pm}(z, p, t)$ in the ground state sublevel $|g, \pm 1/2\rangle$ with position z, momentum p and atomic mass m, obeys [44]:

$$\left[\frac{\partial}{\partial t} + \frac{p}{m}\frac{\partial}{\partial z} - U'_{\pm}(z)\frac{\partial}{\partial p} + F(t)\frac{\partial}{\partial p}\right] P_{\pm} = -\gamma_{+\to-}(z)P_{\pm} + \gamma_{-\to+}(z)P_{\mp} + \frac{\partial^2}{\partial p^2}\left[D_{\pm}(z)P_{\pm} + L_{\pm}(z)P_{\mp}\right], \tag{5.21}$$

where $U'_{\pm}(z) = dU_{\pm}(z)/dz$ is the derivative of the optical potential produced by the laser fields with wave vector k, as given in equation 3.21. $F(t)$ is the time-dependent driving force which is produced by modulating the phase of one of the lattice beams. The optical pumping rate $\gamma_{+\to-}(z)$ and $\gamma_{-\to+}(z)$ are for the transitions $|g, +1/2\rangle \longrightarrow |g, -1/2\rangle$ and $|g, -1/2\rangle \longrightarrow |g, +1/2\rangle$ respectively, with Γ' being the photon scattering

rate. These rates are given by:

$$\gamma_{\pm\to\mp}(z) = \frac{\Gamma'}{9}[1 \pm \cos(2kz)]. \tag{5.22}$$

The term:

$$D_{\pm}(z) = \frac{7\hbar^2 k^2 \Gamma'}{90}\left[5 \pm \cos(2kz)\right], \tag{5.23}$$

represents the diffusion coefficients due to random momentum jumps when the atom absorbs a circularly polarised photon and then relaxes to the same ground state sublevel (i.e. the atomic state does not change) [44]. $L_{\pm}(z)$ is a term proportional to the random momentum jumps and describes the fluorescence cycles when the atom undergoes a transition between the internal magnetic sublevels. It is given by:

$$L_{\pm}(z) = \frac{\hbar^2 k^2 \Gamma'}{90}\left[6 \mp \cos(2kz)\right]. \tag{5.24}$$

The normalisation condition is:

$$\int \mathrm{d}z \int \mathrm{d}p \left[P_{-}(z,p,t) + P_{+}(z,p,t)\right] = 1. \tag{5.25}$$

To renormalise the potential, we now introduce a high frequency driving force. It is due to a phase modulation of one of the lattice beams and it is given by:

$$F_{\mathrm{HF}}(t) = A_{\mathrm{HF}} \sin(\omega_{\mathrm{HF}} t + \varphi), \tag{5.26}$$

where ω_{HF} is the driving frequency which is supposed to be much higher than all characteristic frequencies in the system, i.e. the vibrational frequency of the lattice or the scattering rate.
Integrating ($m\ddot{z} = F_{HF}$) twice with respect to time gives an expression for the spatial variable z describing the fast atomic dynamics: $z(t) = -r\sin(\omega_{\mathrm{HF}} t + \varphi)$. With r being the oscillation amplitude, or the so-called high frequency ratio (HF-ratio), given by:

$$r = \frac{A_{\mathrm{HF}}}{m\omega_{\mathrm{HF}}^2}. \tag{5.27}$$

In an optical lattice, the potential well position can be controlled by changing the phase of the lattice beams. We modulate the phase according to $\alpha = \beta\sin(\omega_{HF} t + \varphi)$ where β is the modulation index in radians.

The second derivative with respect to time is given by:

$$\ddot{\alpha} = -\beta\omega_{HF}^2 \sin\left(\omega_{HF}t + \varphi\right), \tag{5.28}$$

Therefore, the inertial force experienced by the atom is:

$$F = \frac{m}{2k}\beta\omega_{HF}^2 \sin\left(\omega_{HF}t + \varphi\right), \tag{5.29}$$

i.e. the force amplitude is $A_{HF} = \frac{m}{2k}\beta\omega_{HF}^2$. Thus, the high frequency ratio r is related to the phase modulation index β by:

$$r = \frac{\beta}{2k}. \tag{5.30}$$

Hence, the asymptotic limit $\omega_{HF} \longrightarrow \infty$ and $A_{HF} \longrightarrow \infty$ will be considered with finite amplitude to frequency ratio r. The slow position variable $\hat{z}$ is obtained by subtracting the fast oscillating term $-r\sin\left(\omega_{HF} + \phi\right)$ from the position z:

$$\hat{z}\left(t\right) = z\left(t\right) + r\sin\left(\omega_{\mathrm{HF}}t + \varphi\right). \tag{5.31}$$

The Fokker-Planck equation for the new variables can be written as:

$$\left[\frac{\partial}{\partial t} + \frac{\hat{p}}{m}\frac{\partial}{\partial \hat{z}} - \hat{U}'_{\pm}(\hat{z},t)\frac{\partial}{\partial \hat{p}} + F_d(t)\frac{\partial}{\partial \hat{p}}\right]\hat{P}_{\pm} = -\hat{\gamma}_{+\to-}(\hat{z},t)\hat{P}_{\pm} + \hat{\gamma}_{-\to+}(\hat{z},t)\hat{P}_{\mp} + \frac{\partial^2}{\partial \hat{p}^2}\left[\hat{D}_{\pm}(\hat{z},t)\hat{P}_{\pm} + \hat{L}_{\pm}(\hat{z},t)\hat{P}_{\mp}\right], \tag{5.32}$$

here $\hat{P}_{\pm}$ is given by $\hat{P}_{\pm} = m\frac{d\hat{z}}{dt}$, with $\hat{U}'_{\pm}(\hat{z},t) = U'_{\pm}[\hat{z} - r\sin(\omega_{\mathrm{HF}}t + \varphi)]$. The procedure has to be applied to $\hat{\gamma}_{\pm}(\hat{z},t)$, $\hat{D}_{\pm}(\hat{z},t)$ and $\hat{L}_{\pm}(\hat{z},t)$. The probability density is unaffected by the fast modulation so that $P_{\pm} = \hat{P}_{\pm}$.

Averaging equation 5.32 over several high frequency periods removes the fast time dependence of the spatial parameters. This corresponds to an average over the phase φ in equation 5.31 which should not affect the slow dynamics. A generalised Fokker-Planck equation is thus obtained

with the following renormalised coefficients:

$$\begin{aligned}
\bar{U}_{\pm}(\hat{z}) =& \frac{U_0}{2}[-2 \pm \mathrm{J}_0(2kr)\cos(2k\hat{z})], \\
\bar{\gamma}_{\pm\to\mp}(\hat{z}) =& \frac{\Gamma'}{9}[1 \pm \mathrm{J}_0(2kr)\cos(2k\hat{z})], \\
\bar{D}_{\pm}(\hat{z}) =& \frac{7\hbar^2k^2\Gamma'}{90}[5 \pm \mathrm{J}_0(2kr)\cos(2k\hat{z})], \\
\bar{L}_{\pm}(\hat{z}) =& \frac{\hbar^2k^2\Gamma'}{90}[6 \mp \mathrm{J}_0(2kr)\cos(2k\hat{z})],
\end{aligned} \tag{5.33}$$

where:

$$\mathrm{J}_0(2kr) = \frac{1}{2\pi}\int_0^{2\pi} \mathrm{d}\phi_0 \, \cos(2kr\sin\phi_0), \tag{5.34}$$

is the first order Bessel function. The system is effectively renormalised by the high frequency drive in the asymptotic limit $\omega_{HF} \to \infty$. The same conclusion can be reached by considering the lowest order of a multiple time scale formalism utilising the expansion parameter $\epsilon = \omega/\omega_{\mathrm{HF}}$ [9]. As it will be presented in the following, we compared our experimental findings with numerical simulations of the presented Fokker-Planck equation. The simulations were conducted both with finite and infinite frequency and amplitude of the high frequency field using equations 5.21 and 5.32 respectively.

5.4 Experimental setup

The analysis in the previous section shows that the optical potential is renormalised in the asymptotic limit where the frequency and the strength of the drive are infinite. To provide experimental evidence, we need to consider finite driving values away from infinity that are experimentally accessible.

Two experiments were performed on the phenomenon of potential renormalisation and the experimental findings were supported by numerical simulations by David Cubero. The first evidence of potential renormalisation was found by studying the spatial diffusion of the cold rubidium atoms in the optical lattice. The second detection of the phenomenon makes use of the ratchet effect. The observation of a generated current through the optical lattice while varying the amplitude of the high fre-

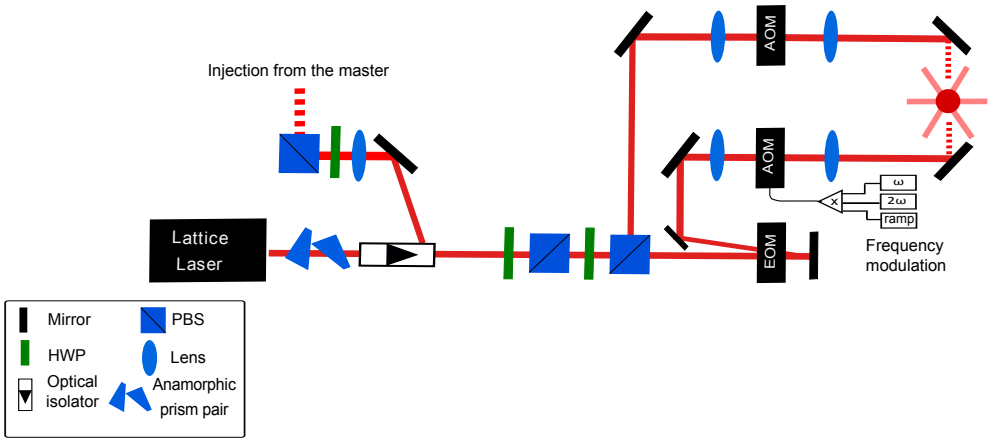

Figure 5.2: The vibrational ratchet setup consists of two counter-propagating laser beams to produce the 1D *lin* ⊥ *lin* optical lattice. The schematic is essentially the same as the one depicted in figure 4.1 of the current reversal experiment described in chapter 4, but with an additional double pass EOM to apply a high frequency phase modulation to the optical lattice.

quency drive holds information about the effective potential.

I built the experimental setup that was used for both experiments. It is shown in figure 5.2. The optical lattice beams are produced by a slave laser. It is injected by the MOT master laser (described in chapter 2 and the setup is illustrated in figure 2.4). The slave's output beam is divided by a PBS cube into the two lattice beams. Their respective power can be balanced using a half wave plate. To enable control over the frequency and the intensity, and also to be able to quickly switch the lattice on and off we introduced an AOM in each of the beams. This also provides the correct detuning of $\Delta = -13.5\Gamma$ for the lattice.

To study the directed transport, it is required to modulate one of the lattice beams to produce the bi-harmonic force (as discussed in 3.5). This is achieved by applying a bi-harmonic signal to the frequency input of the AOM. For the diffusion study this was not necessary. To apply the high frequency force, an Electro-Optical Modulator (EOM) in double-pass configuration is used in the setup. It modulates the phase of one of the lattice beams with a high frequency. The sinusoidal signal to the EOM comes from a function generator[2].

Figure 5.3 and 5.4 show the experimental sequence for the diffusion

[2]3220A, 20MHz Function/Arbitrary Waveform Generator from Agilent Technologies.

and directed transport study respectively. Both start with loading the atoms into the science MOT from the LVIS part of the setup. Typically this lasts for about 2 s. Then, the LVIS beams are switched off and the MOT is compressed by increasing the magnetic field gradient from about 20 G/cm to 40 G/cm over a 50 ms period. Then a molasses phase is applied for 8 ms to reduce the temperature of the atoms even further. This is done by switching off the magnetic field and simultaneously increasing the laser detuning to $\Delta = -6\Gamma$ to reduce the scattering rate. After that, the MOT beams are switched off completely and the lattice beams are turned on. After a millisecond thermalisation without driving, the fast modulation with frequency ω_{HF} is linearly ramped on within 1 ms to its final strength of A_{HF}. To investigate the atomic diffusion, the cloud is let to diffuse inside the strongly modulated optical lattice for different times between 1-16 ms. Then, the cloud dimension is recorded via fluorescence imaging and its width determined from fitting the image with a 2D Gaussian function. For the directed transport study, after the full high frequency drive is applied, the bi-harmonic modulation is ramped up within 4 ms to avoid any kind of switching effects. Then, after few milliseconds driving of the optical lattice with the bi-harmonic force, the centre of mass and the width of the atomic cloud is determined again by fitting a fluorescence image with a 2D Gaussian.

5.4.1 Imaging system

Imaging the atoms inside the optical lattice is essential to investigate the optical potential renormalisation. The atoms in the lattice are imaged using a CCD camera[3] with a 6x magnification lens[4] focused on the MOT. The camera is connected to the computer via a FireWire cable. Normally, the imaging is the final stage of the sequence. It consists of three steps. In the first, the image is acquired with the atoms present by turning on the MOT beams tuned on resonance to the atomic transition. The exposure time delivering the best signal to noise ratio was determined to be 4 ms. Then, the MOT beams were turned off for 50 ms with the camera shutter closed. During this time, the atoms in the cloud fall under

[3] AVT Guppy F-038 B NIR from Allied Vision Technology
[4] Zoom 7000 Macro, EFL 18-108 mm from Navitar.

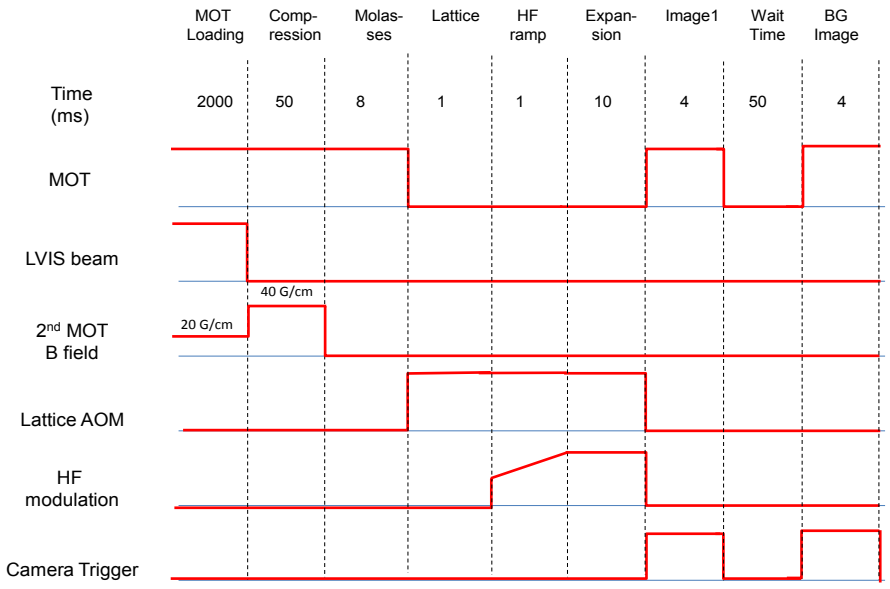

Figure 5.3: Experimental time sequence used to study the spatial diffusion of the atoms.

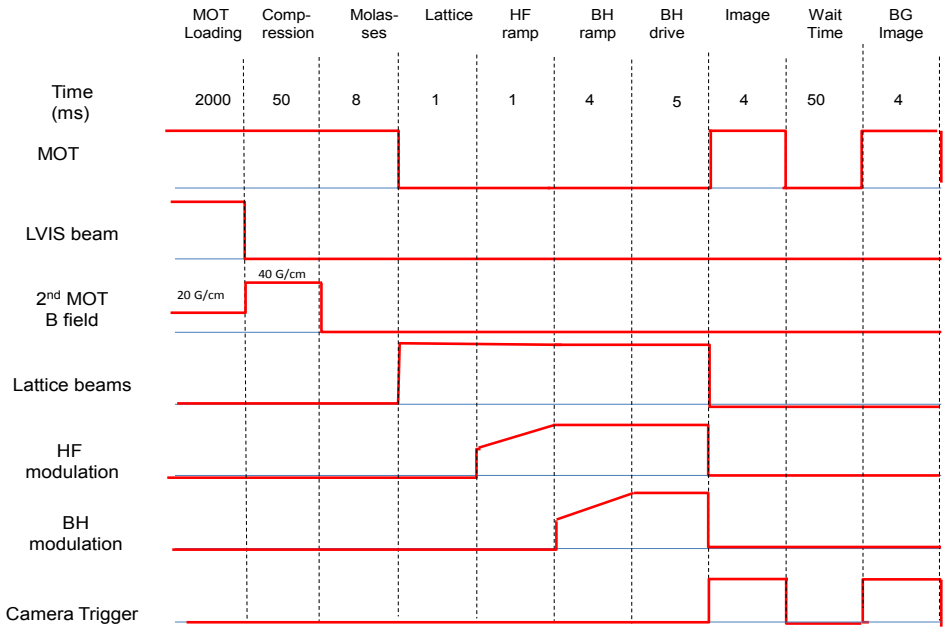

Figure 5.4: Experimental time sequence used to study the directed transport of the atoms in a strongly modulated optical lattice.

gravity, out of the imaging region of the setup. Then a second image was taken, again with the MOT beams on but this time without atoms as a background. Both images were subtracted automatically in Labview and the result fitted with a 2D Gaussian via a Matlab routine. The trigger for the image acquisition came from the experimental control computer to synchronise with the experimental sequence. Initially the camera was calibrated by taking a picture of a ruler placed in the focus of the camera at the same distance as the MOT.

5.4.2 Electro-Optical Modulator (EOM)

For the realisation of the high frequency modulation, a broadband Electro-Optical phase Modulator (EOM)[5] is introduced in the beam path of one of the optical lattice beams. The EOM consists of a nonlinear material exhibiting birefringence induced by a varying electric field. Its principle of operation is the linear electro-optic, or Pockel effect: a linear response of the refractive index with varying electric field applied to a crystal that lacks inversion symmetry.
Changing the voltage applied to the crystal changes the optical path length and therefore induces a phase shift to the transmitted beam. The electro-optic medium used for this thesis is a magnesium oxide doped lithium niobate ($LiNbO_3$) crystal. The maximum voltage that can be applied to this kind of crystal is 210 V. With a phase change per Volt of 0.015 rad/V at 1064 nm this corresponds to a maximum modulation depth of 3.15 rad. This value differs for different wavelengths. To apply the modulation a home built high-frequency amplifier is used following the design described in reference [68]. The amplifier can produce a maximum sine wave amplitude of 550 Vpp with a bandwidth of 1.3 MHz.

EOM characterisation To evaluate the amplitude of the high frequency force used to renormalise the optical lattice, the EOM is characterised by analysing the beat signal of the modulated beam and an unmodulated beam. We therefore apply a sinusoidal voltage oscillation to the EOM:

$$U(t) = U_{HF} \sin(\omega_{HF} t), \tag{5.35}$$

[5] 4002-M from New Focus.

where U_{HF} is the peak-to-peak amplitude of the applied voltage. This modulation produces a phase shift $\alpha(t) = \beta U(t)$. The electric field of the rapidly modulated laser beam is given as:

$$E_{mod}(x,t) = \frac{E(x)}{\sqrt{2}}\left[e^{-i\omega t}e^{-i\beta\sin(\omega_{\mathrm{HF}}t)} + \text{c.c.}\right], \tag{5.36}$$

where $e^{-i\omega t}$ represents the unmodulated oscillation of the laser beam's electric field. The other exponential $e^{i\beta\sin(\omega_{HF}t)}$ is the time dependent term that originates from the high frequency drive. For small modulation indices β the first terms of the Taylor expansion of the exponential are given by:

$$E_{mod}(t) = \frac{E(x)}{\sqrt{2}}e^{-i\omega t}\left[1 + i\beta\sin\omega_{HF}t + \text{c.c.}\right], \tag{5.37}$$

which gives after substitution with Euler's formula:

$$E_{mod}(t) = \frac{E(x)}{\sqrt{2}}e^{-i\omega t}\left[1 \pm \frac{\beta}{2}e^{i(\omega\mp\omega_{HF})t} + \text{c.c.}\right]. \tag{5.38}$$

It can be seen from 5.38 that a small phase modulation results in a pair of symmetric sidebands around the carrier frequency with frequencies $\omega \pm \omega_{HF}$.

For arbitrary phase modulations, there are infinite sidebands and the amplitude of the n-th sideband is given by the n-th order Bessel function. This can be seen from the the Jacobi-Anger identity:

$$e^{ix\sin\theta} = \sum_{n=-\infty}^{\infty} J_n(x)\, e^{in\theta}. \tag{5.39}$$

To calibrate the EOM and determine the modulation depth and thus the high frequency force amplitude, the sideband amplitude had to be determined for different applied oscillations with amplitude U_{FG} for the setup shown in 5.5. We generate a beat signal of a modulated and an unmodulated beam with a frequency difference of +73 MHz. This is easily achievable using an AOM and passing the first order through the double pass EOM and then combines it again with the 0-th order using a non-polarising beam splitter. An additional half wave plate is used to match the polarisation orientation of both beams and optimise their interfer-

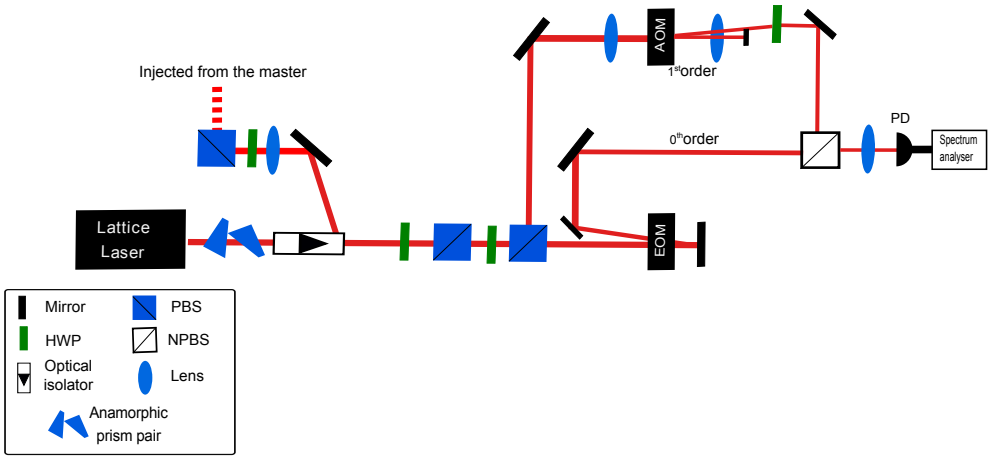

Figure 5.5: The experimental schematic for EOM calibration.

ence on a fast photodiode[6]. The resulting beat signal oscillates with a frequency equal to the difference between the beams' frequencies and the sideband amplitude and can be analysed by a spectrum analyser[7].

Since the zeroes of the Bessel function correspond to specific modulation depths β and also to the disappearance of specific sidebands, we can extract the applied modulation amplitudes U_{FG} when the sidebands vanish in the spectrum. Thus, the modulation depth β can be determined. These data were taken for three different high modulation frequencies and the result is shown in the left graph of figure 5.6. The modulation depth β is determined from the slope of the linear fit for the data. It can be seen that above the value of $U_{FG} = 3\,Vpp$, the response is not linear anymore. It corresponds to the maximum voltage of the amplifier and forms an upper limit to the modulation depth accessible in the experiment. The amplifier goes into saturation. From evaluating the modulation depth, we are able to calculate the high frequency force amplitude and therefore the ratio r from equation 5.30 which is used to renormalise the optical potential. The right graph of figure 5.6 shows the modulation depth per applied driving voltage for different frequencies as derived from fitting the data on the left. It shows that the bandwidth of the whole system is well above 1.3 MHz.

[6]Hamamatsu, GaAs MSM Photo detector G4176-03
[7]Anritsu MS2718B Spectrum analyser 9 kHz-13 GHz

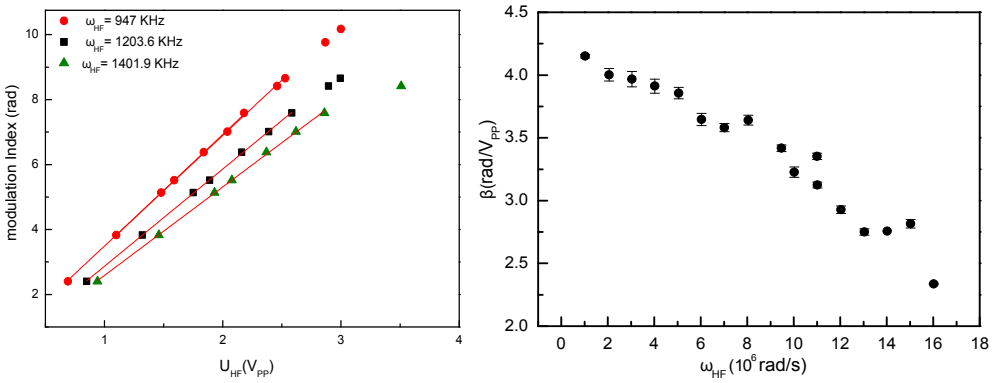

Figure 5.6: EOM calibration. Left: The modulation index represented by the zeroes of the Bessel function as a function of the applied modulation amplitude U_{FG} for three different high frequencies ω_{HF}. The linear fit is taken in order to obtain the modulation depth β per the applied peak to peak voltage. The graph shows nonlinear response after 3 Vpp which is an upper limit for the achievable modulation depth. Right: The extracted slopes of the left graph show the modulation depth per voltage as a function of the high frequency and display the low pass characteristics of the involved electronics.

5.5 Experimental results

To provide evidence of how the optical potential of the 1D lattice is renormalised using the high frequency oscillating field, two experiments were conducted. The first experiment deals with the diffusion properties of a cold atomic cloud in the driven lattice while the second observes the directed transport of the atoms as generated by the ratchet effect. Since the asymptotic limit is not accessible experimentally, we consider a finite high frequency much larger than the vibrational frequency of the atoms in the optical potential. The comparison between the two cases was performed numerically by Dr. Cubero. Both methods will be discussed in the following subsections.

5.5.1 Diffusion properties

The potential renormalisation is detected by examining the atomic spatial diffusion through the optical lattice. The atomic diffusion shows a strong dependence on the optical potential depth. The diffusion increases for decreasing potential depth and shows different diffusion types. The dependence of the diffusion on the lattice depth was investigated in [45, 59]. The spatial diffusion can be characterised by the time evolution

of the squared width as given by:

$$\Delta x^2(t) = \left\langle x^2(t) \right\rangle - \left\langle x(t) \right\rangle^2 \propto t^{\alpha_{diff}}, \tag{5.40}$$

in the limit $t \to \infty$, where α_{diff} is the diffusion exponent. According to the definition in 5.40, the atomic diffusion is called normal when $\alpha_{diff} = 1$, whereas the diffusion becomes anomalous for $\alpha_{diff} \neq 1$. It is well investigated in [39, 45, 59] for a system similar to ours, where two different regimes can be distinguished. The behaviour changes at the critical potential depth $U_{0,\mathrm{crit}} \sim 100\, E_r$ with the recoil energy given as $E_r = \hbar^2 k^2 / 2m$. For a deep potential depths with $U_0 > U_{0,\mathrm{crit}}$ the atomic diffusion is normal. Whereas, in a shallow potentials with $U_0 < U_{0,\mathrm{crit}}$, the system exhibits superdiffusive motion, with $\alpha_{diff} > 1$ [45]. It is expected to observe this transition of the atomic dynamics from normal to superdiffusion when the renormalised potential becomes smaller than the critical potential depth.

The experimental sequence is depicted in figure 5.3. After imaging the cloud by fluorescence imaging and then fitting the data with a 2D Gaussian, the width and the centre of mass of the cloud are obtained. The data were acquired for different expansion times inside the strongly oscillating lattice. Each data point corresponds to an average of 10 data. The expansion time range is restricted by atom loss, mostly attributable to the high frequency modulation that leads to a vanishing optical potential. The atoms are simply falling out of the lattice region. Hence, the atomic diffusion in the lattice cannot be observed for a very long time. The limited temporal range prevents deriving an accurate value of the diffusion exponents α_{diff}, which was required to investigate superdiffusive motion.

Consequently, to study the spatial diffusion experimentally, we had to consider an effective diffusion coefficient D which is less affected by atom loss than α_{diff}. The effective diffusion coefficient is given as:

$$\Delta x^2(t) = \left\langle x^2(t) \right\rangle - \left\langle x(t) \right\rangle^2 = 2Dt. \tag{5.41}$$

The effective diffusion coefficient is obtained from the slope of the linear fit with the function given in 5.41 for the data between the atom

cloud width and the diffusive expansion time of the cloud. Figure 5.7 shows an example for these data for different HF-ratios. It can be shown from the figure, without HF modulation (i.e. undriven optical lattice), the behaviour of the atomic cloud expansion is linear with increasing time. This suggests the normal diffusion region. Increasing the HF ratio causes the appearing of nonlinear behaviour which indicates reaching the anomalous diffusion regime. With further increasing the HF amplitude, the linear behaviour re-appears implying the re-establishment of normal diffusion.

The experimental results for the effective diffusion coefficient $D(r)$ as a function of the high frequency ratio r are displayed in the left graph of figure 5.8. It can be seen that the atomic diffusion is considerably modified by the HF field. The experimental results for the effective diffusion coefficient $D(r)$ as a function of the high frequency ratio r are displayed in the left graph of figure 5.8. It can be seen that the atomic diffusion is considerably modified by the HF field. Increasing the HF amplitude, represented by the high frequency ratio r, causes increasing the effective diffusion coefficient D. Its maximum value matches the zero of the Bessel function and corresponds to shallow potentials. This indicates superdiffusive motion for the atoms in the optical lattice. If the HF amplitude increases further, the diffusion decreases indicating normal atomic dynamics in deep potential depths. The minimum of the diffusion coincides with the maximum of the Bessel function. This mechanism illustrates the renormalisation of the optical potential.
In order to probe an inaccessible frequency regime in the asymptotic limit where $\omega_{HF} \to \infty$ and $A_{HF} \to \infty$, a numerical analysis was done by Dr. Cubero using Monte Carlo simulation. He investigates the spatial diffusion for a 1D optical lattice of atom with the transition $J = 1/2 \to J' \to 3/2$. The aim of this numerical study is to predict the diffusion behaviour.
Two different HF regimes were investigated: infinite and finite frequency and amplitude, in order to confirm the validity of the experimental approach. The right graph of figure 5.8 shows the dependence of the diffusion exponent α_{diff} on the high frequency drive.
Normal diffusion $\alpha_{diff} = 1$ occurs when the potential depth is large. Af-

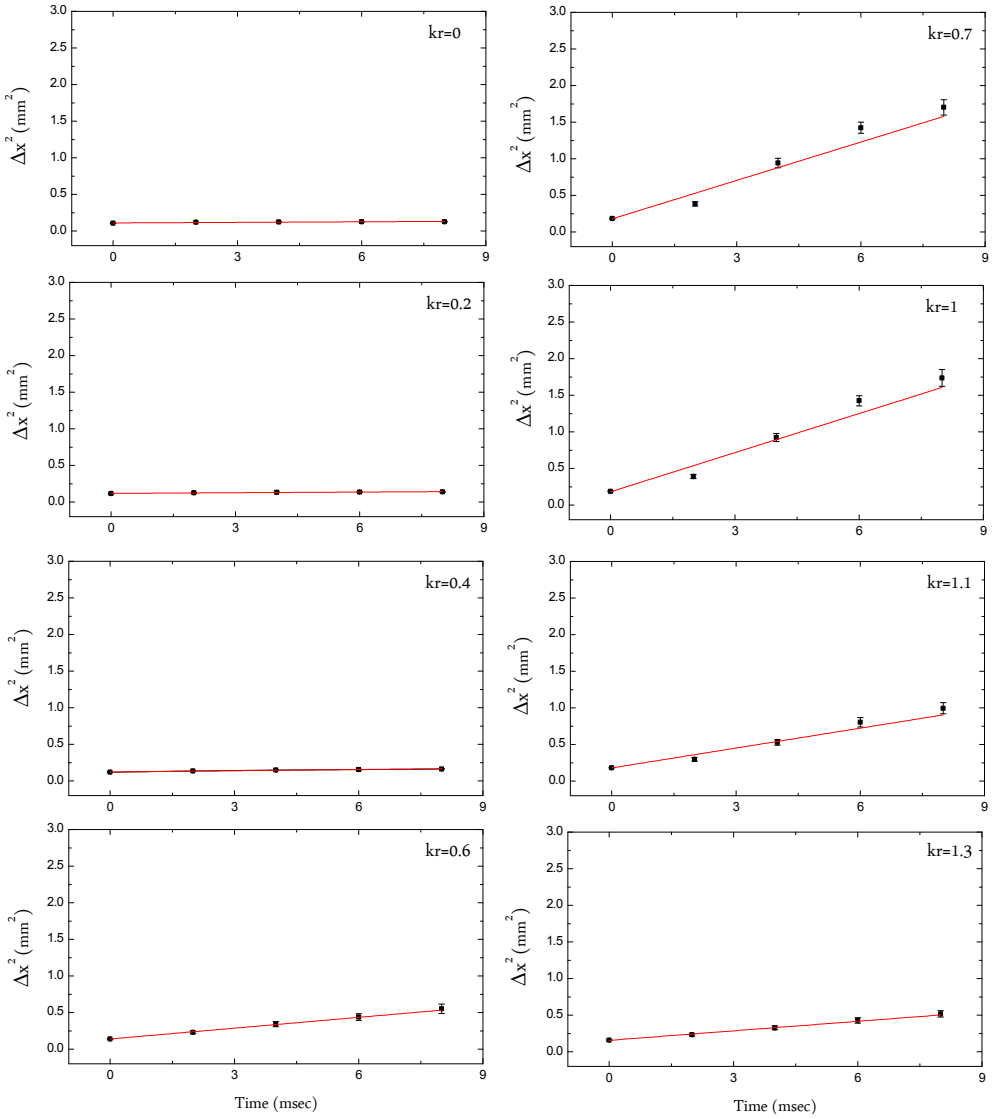

Figure 5.7: The atomic cloud width as a function of the diffusive expansion time. These data are taken with different HF ratios inside a strongly modulated optical lattice. The HF frequency is 7.5×10^6 rad/sec. The red line is the linear fit to the data.

ter that, increasing the high frequency ratio further causes an increase in the diffusion exponent $\alpha_{diff} > 1$, indicating superdiffusive motion. The diffusion exponent approaches its maximum at $\alpha_{diff} = 3$. This can be attributed to the heating of the atom because the photon scattering process carried on even with a vanishing optical potential. Therefore, the sub-Doppler cooling mechanism ceases. Two data sets were simulated for an infinite limit $\omega_{HF} = \infty$, but with different scattering rates, and another data set corresponds to the finite case $\omega_{HF} = 20$. It is

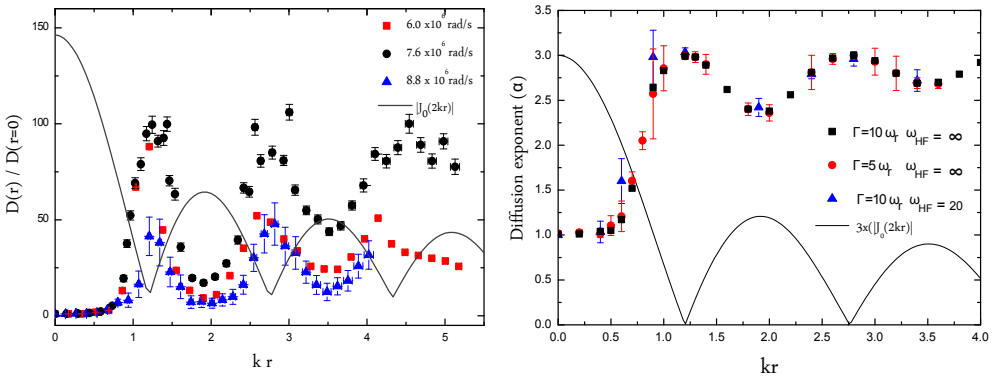

Figure 5.8: The experimental and theoretical results of the diffusion properties study for a modulated optical lattice. Left: The experimental results for the effective diffusion coefficient D as a function of the HF ratio r for three different ω_{HF} values. The data are rescaled by the diffusion coefficient for the undriven lattice $D_{(r=0)}$ which is between $1.5\lambda^2/\mu m$ and $7.5\lambda^2/\mu m$. The vibrational frequency of the atoms at the bottom of the optical potential, which is calculated from the laser beam size measurements, is $\omega_v = (9\pm1).10^5$ rad/s. Three data set are measured for different $\frac{\omega_{HF}}{\omega_v}$ ratios: (6 ± 1), (8 ± 1) and (9 ± 1). The black line shows the Bessel function $J_0\,(2kr)$. Right: Numerical analysis obtained by Monte Carlo simulations. The spatial diffusion exponent α_{diff} is plotted as a function of the HF ratio r for an optical lattice with a depth of $U_0 = 200E_r$. Two data sets are displayed for two different scattering rates $\Gamma' = 5\omega_r, 10\omega_r$ in the infinite limit, where ω_r is the recoil frequency. The third data set is for $\Gamma' = 10\omega_r$ for a finite ratio $\frac{\omega_{HF}}{\omega_v} = 20$. The black line shows the Bessel function $J_0\,(2kr)$. The error bars correspond to the finite statistics of the Monte Carlo simulation.

found that there is not much difference between diffusion of the finite and infinite applied high frequency to the optical lattice. However, ω_{HF} has to be much higher than the vibrational frequency. In conclusion, both experimental and theoretical results represented by D and α_{diff}, showed the renormalisation of the optical potential as determined by the high frequency drive. The diffusivity behaviour follows the periodicity of the Bessel function $J_0\,(2kr)$. The result also displays the superdiffusion regime where the diffusion maxima match the minima of the potential depth at a given high frequency.

5.5.2 Directed transport

The observation of directed transport is the second detection scheme that we used to probe the optical potential renormalisation by the high frequency field. As explained in chapter 3, a directed current of atoms in the optical lattice can be generated by a bi-harmonic driving force

of the form 3.6. Hence, studying the potential renormalisation requires applying a bi-harmonic drive in addition to the high frequency driving given in 5.26, which has a frequency $\omega_{HF} >> \omega_d$. As established in 5.5.1, the high frequency field renormalises the optical potential. Therefore, the directed current is affected by the high oscillating field and it is expected to vanish whenever the renormalised potential vanishes.

The experimental procedure follows the sequence in figure 5.4. The bi-harmonic signal that modulates the frequency of one of the lattice beams, is ramped up adiabatically in 4 ms to the final amplitude. Then, the cloud is imaged by fluorescence imaging after 5 ms of full amplitude driving. Since the directed current and thus the atom velocity is required to be investigated in the current experiment, the centre of mass position of the cloud is the quantity of our interest. The position of the centre of mass was taken for different driving times of the bi-harmonic force. These measurements were repeated ten times with a varying phase difference of the bi-harmonic drive between $\phi = 0$ and $\phi = 2\pi$. Then, the velocity of the centre of mass of the cloud is obtained from the linear fit of the data between the position and the driving time for a given phase. The result is shown in figure 5.9 for different amplitudes of the high frequency drive. These data were fitted with the function 4.2 which can extract the maximum velocity amplitude v_{max} from the fit result. It is clearly shown that the directed current is influenced considerably by the high oscillating field. In the absence of the HF field ($kr = 0$), the current shows sinusoidal behaviour as expected of the ratchet current. At increasing high frequency amplitude, v_{max} starts to decrease until it vanishes at $kr = 1.27$. For further increases in the high oscillating field, the sine like curve appears again. Therefore, v_{max} is an accurate indication the renormalisation of the optical potential.

The whole set of results of the directed current as a function of the high oscillating field ratio r is displayed in figure 5.10. As can be seen from the figure, the maximum velocity amplitude is strongly affected by the high frequency amplitude. The experiment was performed for three different ω_{HF} whose highest value was $\omega_{HF} = 10\omega_v$ which is limited by the EOM bandwidth. The behaviour of all the three HF frequencies is consistent and follows the periodicity of the Bessel function. At the zeroes of the Bessel function, the ratchet current is zero, while at the

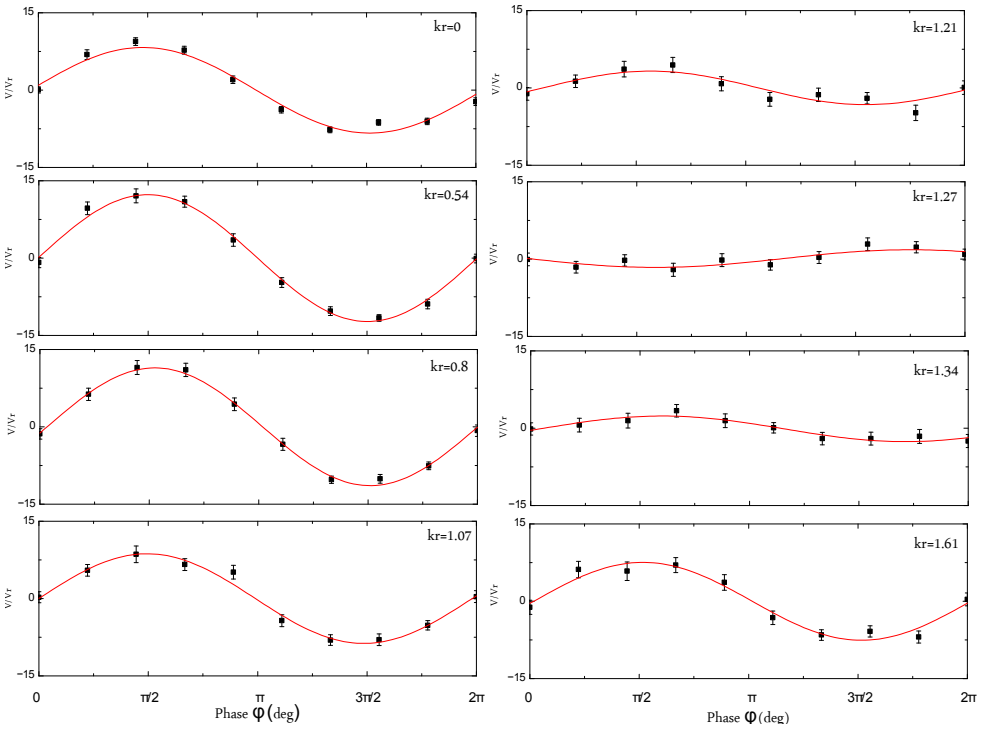

Figure 5.9: The velocity of the centre of mass of the cloud as a function of the relative phase between the harmonics of the driving force for different HF ratios r. The red curves shows the fit with the function given in 4.2 and v_{max} is the maximum velocity amplitude which is used to monitor the potential renormalisation. Without high frequency driving, $r = 0$, the behaviour is sinusoidal as shown in the first panel. When the high frequency drive increases, the potential amplitude gets smaller until it vanishes around $kr = 1.27$. With further increasing of the high frequency amplitude, the velocity amplitude appears again, which means that the optical potential is renormalised. The frequency of the HF field is $\omega_{\mathrm{HF}} = 8.8 \times 10^6\,\mathrm{rad/s}$ while the driving frequency of the bi-harmonic force is $\omega_d = 9.4 \times 10^4\,\mathrm{rad/s}$.

maxima the atomic current appears with a maximum amplitude for a given high frequency ratio kr.

Numerical simulations were produced by Dr. Cubero and they confirm our results and also probe the regime inaccessible in our experiment. The numerics were done for the infinite limit of the high frequency $\omega_{HF} \to \infty$. Figure 5.10 shows the numerical results for finite and infinite high frequencies. No significant difference is observable between data for $\omega_{HF} = 20\omega_v$ and $\omega_{HF} = \infty$. We notice that the first maximum of the atomic current is at about $kr = 0.75\,\mathrm{rad}$. This can be interpreted as a result of the superimposed resonance between vibrational levels. The renormalised vibrational frequency matches the driving frequency of the

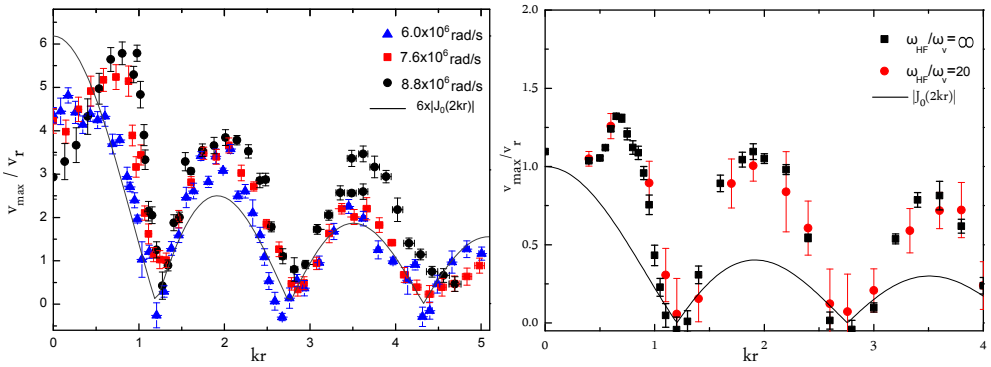

Figure 5.10: The experimental and numerical results of the maximum current amplitude, rescaled by the recoil velocity v_r, as a function of the high frequency drive ratio r for different HF frequencies. Left: The maximum amplitude velocity is obtained by fitting the data shown in figure 5.9 with the function 4.2. The measurements were repeated for three different frequencies of the high frequency drive $(6, 7.6, 8.8) \times 10^6\, rad/s$ which makes the HF frequency bigger than the vibrational frequency of the atom in the potential by a factor $\frac{\omega_{HF}}{\omega_v} = (6.6 \pm 0.1), (8.4 \pm 0.1), (9.7 \pm 0.1)$ respectively. The bi-harmonic drive parameters are $A = 1, B = 2$, $\omega_d = 9.42 \times 10^4$ and $F_0 = 112\hbar k\omega_r$. Right: Numerical results obtained by David Cubero using Monte Carlo simulation methods. The maximum amplitude of the current $v_{\max}$ is rescaled by the recoil velocity v_r and is presented as a function of the HF ratio r in the presence of a bi-harmonic drive of the form 3.6 where $A = B = 1$, $F_0 = 140\hbar k\omega_v$ and $\omega_d = \omega_v$. The data were analysed for two driving frequency values: one for the infinite limit ω_{HF} and the second for finite driving frequency $\omega_{\mathrm{HF}} = 20\omega_v$. Both cases with $\Gamma' = 10\omega_r$ scattering rate. Experimental and theoretical data set show an agreement in the atomic current behaviour with different HF frequency modulation. Applying the high frequency force progressively induces the renormalisation of the optical potential which corresponds to the Bessel function periodicity. The solid line is the absolute value of the first kind Bessel function which serves as a guide for the eye.

bi-harmonic force. The results of the second detection method confirm that the optical potential is renormalised by applying a high frequency field.

5.6 Summary

This chapter described the experiment I conducted to investigate the vibrational resonance phenomenon in a 1D optical lattice with ^{87}Rb atoms. The aim of this experiment was to provide evidence of how to tune the periodic potential of the optical lattice by applying a HF force with a frequency much higher than any other frequency in the system. The high

frequency force was implemented in the experiment by modulating the phase of one of the lattice beams. The potential is renormalised as a result. It increases and then decreases until it vanishes and reappears again, while increasing the high frequency amplitude represented by the HF ratio r. I conducted two experiments to detect the potential renormalisation by a HF field. The first experiment examines the diffusion properties of the atom inside the optical lattice. It was found that by increasing the HF-ratio r, a transition from normal to superdiffusion is observed. Due to the limited temporal range which leads to the atom loss in the very long diffusive time of the cloud, an effective diffusion coefficient D is introduced since it is less sensitive to the atom loss. To be able to support our experimental results, a numerical analysis was done by our collaborator David Cubero to examine the atomic diffusion properties in the long time using the diffusion exponent α_{diff}. Both experimental and theoretical results demonstrated the control of the atomic diffusion by tuning the frequency of the HF field. The second detection method investigates the directed transport generated by a bi-harmonic driving. The results showed the dependence of the atomic current amplitude on the high frequency ratio r. Again numerical analysis was performed, and both experimental and theoretical results showed an agreement in the potential behaviour whose renomalisation corresponds to the Bessel function periodicity. Both detection methods confirmed the possibility of renormalising the optical potential by applying a high frequency field. The mechanism used here is very general and can be used in many other systems.

Chapter 6

BEC: Realisation and Characterisation

This chapter presents the theoretical background as well as the first experimental demonstration of Bose-Einstein condensation at UCL. The BEC is created in a magnetic trap in the Quadrupole-Ioffe configuration (QUIC). This kind of trap combines an anti-Helmholtz quadrupole field with an offset field produced by a single coil perpendicular to the quadrupole field axis. The sequence of the experiment follows the standard procedure used to create BECs in QUIC traps. First the atoms are cooled and trapped in a magneto-optical trap achieving temperatures of the order of several μK. Next, the atoms are cooled in an optical molasses to reach Lower temperatures while conserving the density. After that, the atoms are loaded into a magnetic quadrupole trap followed by compression and transport into the QUIC trap. In the quadrupole trap evaporative cooling is performed by using radio frequency, reaching the phase transition to a BEC in the QUIC trap. The chapter is organised as follows: first it gives a brief theoretical introduction to BECs, then it details the construction and improvements of the MOPA laser system, which was needed to achieve higher atom numbers, finally the experimental setup and the imaging system is described and the first experimental results on Bose-Einstein condensation are presented.

6.1 Introduction to BEC

Bose-Einstein condensation is a macroscopic quantum phenomenon. Since the first prediction by Einstein in 1924, the first experimental realisation of the BEC in dilute gases was in 1995 for ^{87}Rb atoms [1]. Then, this work was followed by many experimental demonstrations [6, 7]. In quantum mechanics, atoms are known to be either half integer spin fermions, which cannot occupy the same quantum state according to the Pauli exclusion principle, or integer spin *bosons* without restriction on the number of atoms occupying the same quantum state. If a vapour of bosonic atoms is cooled to a very low temperature, and then the particles' separation is comparable to the thermal de Broglie wavelength, the wave packets of the atoms overlap. Therefore, it is not possible to distinguish different atoms. Thus, the system approaches the quantum degeneracy and follows the Bose-Einstein statistics. The phase-space density (PSD) denoted by ρ, defined as the particles number in a cubic volume of the thermal de Broglie wavelength, is used as a quantity to measure the degree of the quantum degeneracy of a system [24, 73]:

$$\rho = n\lambda_{dB}^3, \tag{6.1}$$

where n denotes the atom number density $n = N/V$, and λ_{dB} is given by:

$$\lambda_{dB} = \frac{h}{\sqrt{2\pi m k_B T}}. \tag{6.2}$$

where h is Planck's constant, m is the atomic mass, k_B is Boltzmann's constant and T is the temperature in Kelvin. In the case of a bosonic gas confined in three dimensions, the atoms can accumulate in the lowest energy quantum state when the phase space density ρ approaches 2.6 [47]. Laser cooled atoms are neither cold nor dense enough to generate a sufficient phase space density for the BEC transition. The breakthrough in Bose-Einstein condensation happened with the implementation of magnetic traps and evaporative cooling, which enabled far lower temperatures and higher densities than previously reached.

6.2 Upgrading the laser system

As explained in chapter 2, cooling and trapping of neutral atoms requires a stable source of laser light, with narrow linewidth and precise tunability [77]. In addition, a high power laser is also crucial to achieve a large number of trapped atoms for Bose-Einstein Condensation experiments in which an initial high particle number is indispensable. Many parameters contribute to the amount of trapped atoms, such as the optical alignment, the frequency detuning, the polarisation and the magnetic field gradients. In addition, it is well known that larger cooling beams ($\approx 2.5\,\text{cm}$ in our experiment) increase the capture cross section and therefore the atom number in the trap. Thus, a high power laser is necessary. Furthermore, upgrading the vacuum system to a double MOT chamber is another reason why a high power laser becomes important. Therefore, the laser system, based on a diode laser with 80 mW maximum output power, is replaced by a Master Oscillator Power Amplifier (MOPA) system. It is a master laser which is fed through a 2 W tapered amplifier, achieving up to 500 mW of single mode usable cooling light at 780 nm.

6.2.1 MOPA construction

Since the power provided by the diode laser is insufficient for a BEC experiment, I assembled a Master Oscillator Power Amplifier (MOPA) laser system. The master oscillator is the master laser that seeds a GaAs tapered amplifier[1] in a DHP (Divided High Power) heat sink frame. This configuration amplifies the power from a few milliwatts to up to 2 W [104].

Without injection, the tapered amplifier gain profile has a width of $\approx$11 nm. When it is injected by a seed laser, the output gain is narrowed down to the same wavelength of the seed laser (780 nm). The action of the amplifier relies on the chip design which consists of two gain sections: ridge and taper sections. The ridge stage works as a waveguide for the input seed laser from the rear facet. This narrow section selects only the laser mode TEM_{00} and suppresses the undesired laser modes. The taper section is an amplification region with an output gain guide for

[1] m2k-TAL-0785-2000

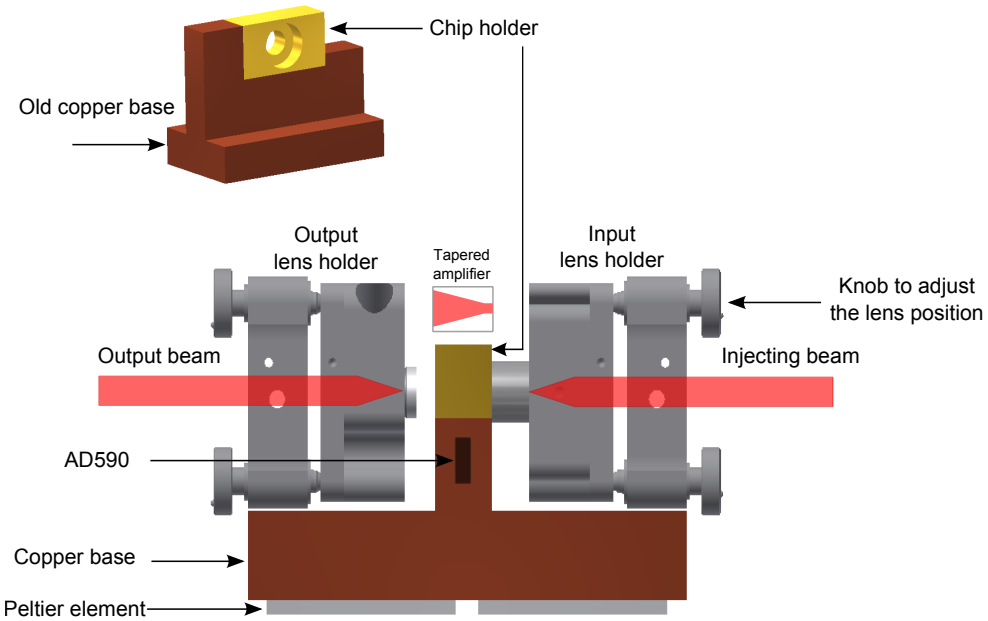

Figure 6.1: Design of the MOPA construction. Upper figure: The old design of the tapered amplifier holder. Only the amplifier chip is mounted on the copper base while the modified fibre launchers, used to mount the lenses and enable three dimensional adjustment, are placed on an aluminium heat sink. Only the copper base is temperature stabilised. The thermal variation in this design influences the output power stability. Lower figure: The new design of the holder with longer copper base than the previous design. Both the amplifier chip and the lens mounts are placed on the copper base and their temperature is stabilised. Two Peltier coolers are used to ensure that the temperature of the whole copper base is controlled.

the broad pumped area with output facet dimensions $(256 \times 1.1)\ \mu m^2$. On the contrary to laser diodes with small facets that can be damaged with high intensity, the tapered amplifier, with its wide output facet, does not suffer from this problem. Both output and input facets have anti-reflection coating with less than 0.01% reflectivity to prevent lasing of the chip itself without seeding.

6.2.2 MOPA design

The amplifier is mounted on a homemade copper block with large thermal conductivity as displayed in figure 6.1. The maximum output power that can be obtained from our chip can differ from 2 W depending on many parameters such as the power of the injection beam, the chip temperature, the injection current and also the seeding beam polarisation.

Temperature stabilisation is required since the gain and therefore the output power depend strongly on the temperature of the chip. The stabilisation also prevents thermal breakdown of the chip which produces a considerable amount of heat during operation.
The old MOPA design (shown in the upper part of figure 6.1) displayed long term power fluctuations, which affected the operation of the experiment. In that design, only the tapered amplifier was placed on a temperature stabilised copper base whereas the lenses holders were fixed directly on the aluminium block used as a heat sink. This configuration leads to undesirable behaviour when the temperature in the lab changes. The lens mounts change their temperature, with a corresponding thermal expansion, resulting in misalignment of the seed beam with a corresponding drop in the output power. To optimise the performance of the MOPA, I improved the design in which both the amplifier chip and the lens mounts are fixed on a temperature stabilised copper base as shown in the lower part of figure 6.1. The resulting temperature and therefore power stability was far better than before. The copper base is housed inside an anodised aluminium box which acts as a heat sink. The temperature is stabilised by two Peltier elements[2] connected in parallel and placed between the copper base and the aluminium block with thermal paste to increase the thermal conductivity between the surfaces. A temperature sensor[3] is attached to the copper block close to the chip. A temperature controller[4] is used to control and monitor the temperature of the amplifier chip.
Two aspheric lenses are utilised to collimate the input and output of the tapered amplifier: the input lens from Thorlabs[5] has a numerical aperture of 0.5 while the output lens from Melles Griot[6] has a higher numerical aperture of 0.62. Owing to the tapered gain region from the output facet, a higher numerical aperture lens is required. Both input and output lenses have 8 mm focal length. A fibre launcher[7] is modified to mount both lenses. This arrangement offer fine adjustment over five

[2]MULTICOMP-MCPE1-12707AC-S from Farnell
[3]AD590
[4]TED200C from Thorlabs
[5]C240TME-B from Thorlabs
[6]GLC-8.0-8.0-830 from Melles Griot
[7]Newfocus 9095 from Newport

degrees of freedom, good injection of the input beam and appropriate collimation of the output light. Since the emitted beam from the tapered amplifier is quite astigmatic and divergent, the vertical direction of the beam is collimated by the output lens inside the amplifier housing. A 100 mm cylindrical lens is utilised in order to collimate the stronger divergence in the horizontal plane. The beam shape is roughly circular, which enables coupling into a single mode optical fibre with 60% coupling efficiency.

To inject the tapered amplifier most of the master oscillator light is used, the remaining fraction being used for the DF-DAVLL. The injection is first achieved at low driving current of the amplifier. The procedure starts by sending, using an ultra stable mirror mount[8], the seed laser beam to the input facet of the tapered amplifier and overlapping it with the back reflection. The back reflection results from spontaneous emission, which is the only dominant mechanism at very low current. To be able to understand the behaviour of the amplifier when driving it with different currents, I measured the output power as a function of the driving current. These measurements were taken with and without seeding the chip and for different chip temperatures. Figure 6.2 shows the dependence of the power output of the tapered amplifier on its current. Without injection, the maximum output power of the MOPA is about 50 mW. A threshold behaviour over the range (0-1.5) A can be observed similar to a diode laser. Thus, the emission starts from 1.25 A and 1.5 A with and without injection respectively. According to the manufacturer datasheet, the typical operation current without injection is 2 A. When the MOPA is injected, it can be operated with up to 4 A, which supplies about 2 W of laser power.

6.2.3 MOPA experimental setup

The master oscillator in our MOPA system is an external cavity diode laser in Littrow configuration as described in chapter 2. This laser is used to inject the tapered amplifier with a few milliwatts (15 mW in our MOPA system) of narrow linewidth laser light at 780 nm.

[8]Polaris-k1 kinematic mirror mount

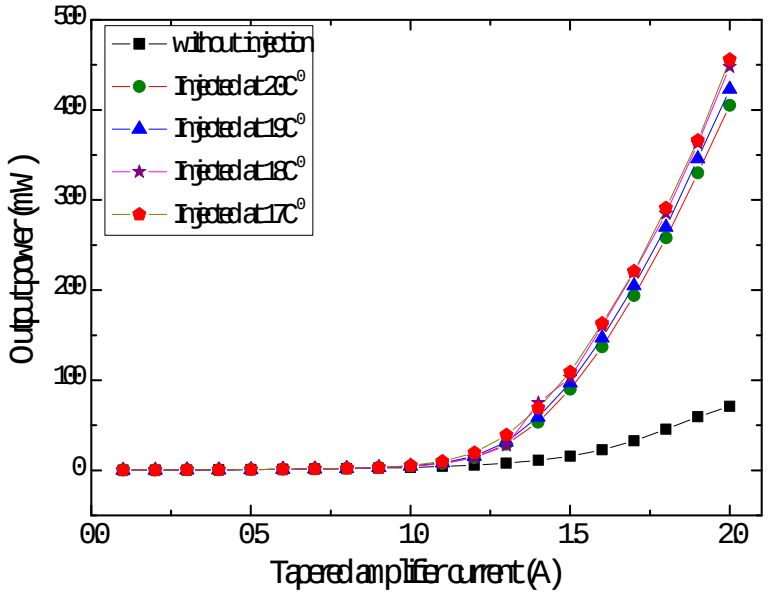

Figure 6.2: MOPA output power as a function of the current of the tapered amplifier for different temperatures. Without injection, the maximum output power is about 50 mW. The data sets for the injected MOPA were taken with 15 mW seed power.

The optical setup of the MOPA system is shown in figure 6.3. The output beam from the master laser passes through an optical isolator with isolation of 40 dB in order to prevent the optical feedback into the seed laser. Then, a fraction of the laser beam passes through an AOM in a double pass configuration to shift the frequency down by about 200 MHz before it is sent through a Doppler-free DAVLL setup to produce an error signal. By using the downshifted beam, the laser is then locked to the $5^2S_{1/2}F = 2 \rightarrow 5^2P_{3/2}F = 2, 3$ crossover feature for the ^{87}Rb D_2 line resulting in a final frequency detuning of the unshifted beam of around +66 MHz above the cycling transition $5^2S_{1/2}F = 2 \rightarrow 5^2P_{3/2}F = 3$. This detuning is controllable by about $8\,\Gamma$ by changing the radio frequency applied to the AOM. The unshifted beam is then injected into the tapered amplifier. The injection is optimised by placing a half wave plate before the tapered amplifier to match the polarisation of the seeding beam with the polarisation of the tapered amplifier. After the amplifier, another optical isolator[9] with 60 dB isolation is introduced to prevent any harmful

[9]Conoptics Model 716 from Lambda Photometrics

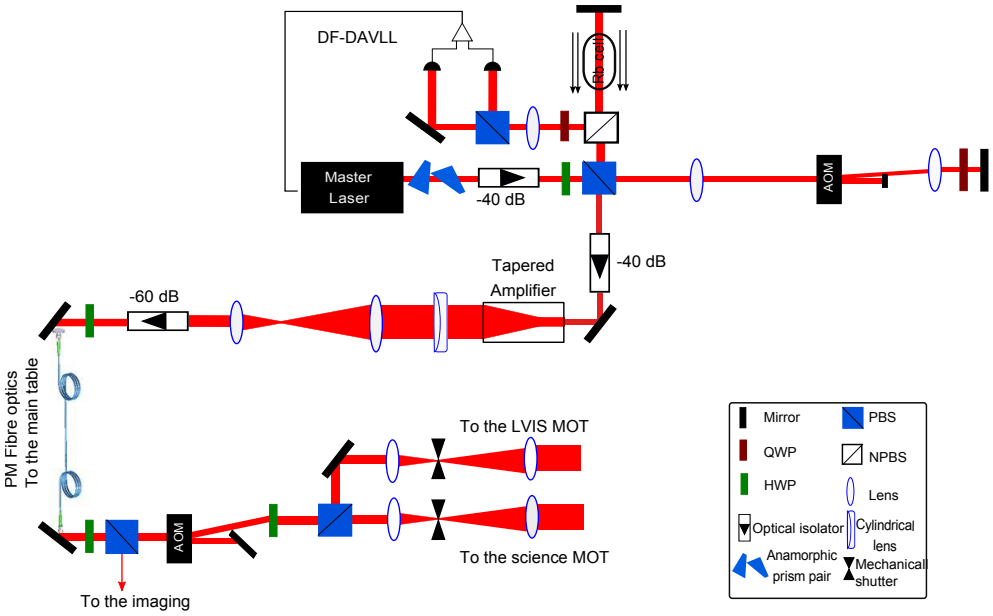

Figure 6.3: The experimental schematic for the MOPA system. The master oscillator is an external cavity diode laser in Littrow configuration. The output beam of the master laser passes through an optical isolator to prevent any back reflection into the laser diode. Then, the beam is split into two parts: one goes to inject the tapered amplifier. The other part is used to stabilise the laser frequency. This is done by sending the beam into a double pass AOM to shift the frequency down twice by 100 MHz. After that, the beam is sent into a DF-DAVLL frequency lock scheme.

back reflection into the tapered amplifier chip. The output profile of the MOPA in the vertical direction shows high contrast stripes. Therefore, in order to remove these features, we filtered the laser beam spatially by coupling it into a single mode polarisation maintaining fibre[10]. This fibre transfers the cooling light onto another optical table, which contains the vacuum system and the optics for both MOTs. The light used for the MOTs therefore has a Gaussian profile.

All the optical components used for locking the re-pumper laser are also located on the MOPA table. This is beneficial in several ways: the MOPA's box is enclosed and therefore more temperature stable. Also, all optical shutters are placed on the main table that contains the vacuum chambers, and do not disturb the locking signal. To achieve a higher power, the re-pumper laser is injected into a slave and then transferred to the main table by a single mode optical fibre. The re-pumper laser is locked to the transition $5^2S_{1/2}F = 1 \rightarrow 5^2P_{3/2}F = 2$ and there is no need

[10]P3-780PM-FC-5-Patch Cable from Thorlabs

for an AOM. The re-pumper beam is overlapped to the cooling beam as in the previous setup of figure 2.4. The schematic of the re-pumper laser setup is depicted in figure 6.5.

6.3 Imaging system

The atomic cloud in our science chamber is monitored via two different diagnostic techniques. The first is the fluorescence imaging which is based on collecting the fluorescence from the atoms, and gives the real time record of the state of the MOT. It does not require any probe beam. For a BEC experiment, absorption imaging is the most crucial technique as it provides detailed information about the atomic cloud such as temperature, width, position and atom number.

6.3.1 Absorption imaging

Absorption imaging is based on the observation of the shadow of the atomic sample by illuminating the cloud with a weak (≈5 mW) and short pulse (0.1 μs) of circularly polarised laser light. It is tuned on resonance with the ^{87}Rb D_2 line cycling transition ($5^2S_{1/2}F = 2 \rightarrow 5^2P_{3/2}F = 3$). When the probe beam passes through the atom cloud, the atoms scatter photons and the atomic sample appears as a shadow. A darker shadow means that more atoms absorb the imaging beam. The shadow is recorded by a CCD camera (details in the next section).
The incoming intensity I_0 of the probe light should be significantly less than the saturation intensity 1.67 mW/cm^2 for $\sigma_\pm$ polarised light. The attenuation of the probe beam passing through the atom cloud can be described by the Beer-Lambert Law:

$$I\left(\vec{r}\right) = I_0 e^{-OD(\vec{r})}, \tag{6.3}$$

where $OD\left(\vec{r}\right) = \int n\left(\vec{r}\right)\sigma_{abs}dz$ is called the optical depth, which indicates the absorption strength of the imaging laser beam at each pixel of the camera. $n\left(\vec{r}\right)$ is the density distribution of the cloud and σ_{abs} is the absorption cross section at resonance. By taking the logarithm of both

sides of equation 6.3, the optical depth of the cloud becomes:

$$OD\left(\vec{r}\right) = ln\left(\frac{I_0}{I\left(\vec{r}\right)}\right). \tag{6.4}$$

Experimentally, the optical depth is measured by taking three images. First, the atoms are imaged with the probe light (shadow image). Second, an image is taken without atoms when the magnetic field is off but the probe beam is on (light image). Then, a so-called dark image is recorded without probe beam and without atoms. Both second and third images were taken for renormalisation purposes in order to eliminate any offset value resulting from the background light or electronic noise. The optical depth is calculated for each pixel by subtracting the dark image from both the light and the shadow images and then taking the natural logarithm of their ratio, as in the following formula:

$$OD\left(\vec{r}\right) = ln\left(\frac{I_{light} - I_{dark}}{I_{shadow} - I_{dark}}\right). \tag{6.5}$$

The total optical depth is calculated from the integration of 6.5 for all the pixels. Images of the optical depth provide a 2D distribution of the atomic cloud. Fitting the atom cloud with a 2D Gaussian function, thus obtaining the cloud centre of mass from the fitting results, and then calibrating the camera (i.e. from pixels into micrometres scale) allows us to evaluate the atom number in the trap, which is given by:

$$N = \frac{1}{\sigma_{abs}} \int OD dx dy. \tag{6.6}$$

The absorption cross section σ_{abs} for resonant circular polarised light is calculated to be $(2.9\times10^{-9})\,\mathrm{cm}^2$, from the formula [93]:

$$\sigma_{abs} = \frac{3\lambda^2}{2\pi} \frac{1}{1 + \frac{I}{I_s} + \left(\frac{2\Delta}{\Gamma}\right)^2}. \tag{6.7}$$

where $\lambda = 780\,\mathrm{nm}$, $I << I_s$ and the light is on resonance ($\Delta = 0$).

6.3.2 The CCD camera

The shadow of the atomic cloud is monitored by a triggerable CCD camera[11] with a resolution of (1392×1040) pixels of size (6.45×6.45) μm^2. An objective is used to collect the probe light passing through the atomic cloud. To determine the width and the position of the atomic cloud, the camera has to be calibrated. This was achieved using a Time Of Flight (TOF) method, which is based on switching the trapping magnetic field off while allowing the atomic cloud to expand ballistically within different times. Then, the cloud's centre of mass is observed as a function of the time of flight. The data were fitted with a parabola function to obtain the calibration ratio of 2.98 μm per pixel which corresponds to the effective pixel size. This defines the magnification of the imaging system to be around 2.16. The cloud temperature can also be extracted from these measurements as will be explained in section 6.7. The spectral range of the camera operation is between (290-1100) nm.

For good imaging performance, saturation has to be avoided. Saturation happens when pixels lose their ability to host an additional charge. Therefore, it is necessary to use a very attenuated probe beam.

6.3.3 Imaging experimental setup

The imaging light is extracted from the setup described in figure 6.3. A small fraction (about 3%) of the outcoming cooling beam from the optical fibre is taken for the imaging system by using a pellicle beam splitter[12]. The optical setup of the absorption imaging is depicted in figure 6.4. Since the imaging beam fraction is taken before passing through the MOT's AOM, it has a frequency detuning of about +66 MHz as explained in subsection 6.2.3. Therefore another AOM is required to shift the imaging beam frequency down to resonance and to switch the beam intensity. Then, the shifted beam is coupled to a single mode optical fibre to be able to filter the beam spatially. Then, the beam is collimated by a 60 mm focal length lens before passing through the science cell. A half wave plate and a polarising beam splitter are positioned after the lens to reduce polarisation fluctuations as a result of temperature fluc-

[11] Digital 14 bit CCD Pixelfly camera from PCO.
[12] BP208 Pellicle beam splitter from Thorlabs

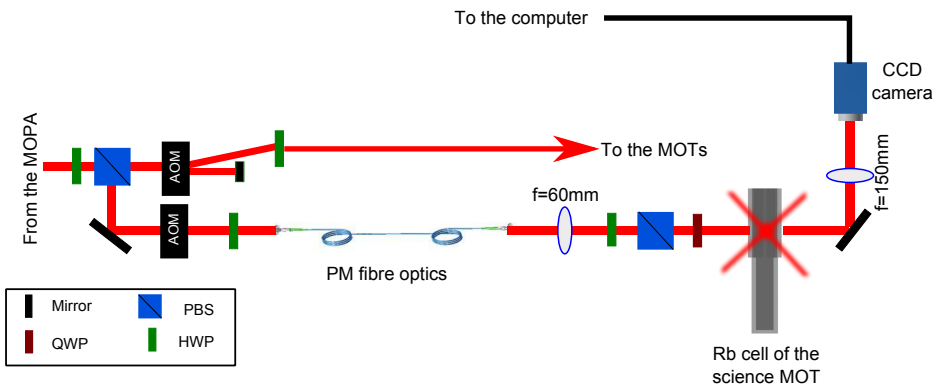

Figure 6.4: The experimental diagram of the absorption imaging system. The imaging beam passes through an AOM used to shift the imaging beam frequency down to resonance with the atomic transition and to switch the beam intensity. Then, the beam is coupled into a single mode optical fibre. The imaging beam is collimated by a 60 mm focal length lens. A HWP and a PBS are placed to reduce the polarisation fluctuations. For a circularly polarised beam, a quarter wave plate is inserted in the beam path before passing through the glass cell. Another lens of 150 mm focal length is used to focus the beam on to the CCD camera.

tuations and mechanical stress of the optical fibre. To ensure having a circularly polarised beam, a quarter waveplate is introduced in the beam path before entering the science cell. The collimated beam with a waist of (7.5 ± 0.1) mm and intensity $\approx 0.5\,\mathrm{mW/cm^2}$, passes horizontally through the science cell and images the shadow of the atomic cloud using a lens of 150 mm focal length. It is positioned about 240 mm after the glass cell onto the chip of the CCD camera. For high performance of the absorption imaging, the image of the cloud has to be focused to obtain the cloud size precisely. Therefore, I mounted the 150 mm focal length lens on a translation stage to be able to adjust the image of the cloud size in a micrometre scale. This arrangement enables us to determine the atom cloud temperature by monitoring the ballistic expansion of the cloud.

6.4 Quadrupole-Ioffe Configuration (QUIC) trap

A quadrupole magnetic field (QUAD) is produced by two coils arranged in the so-called anti-Helmholtz configuration. The two circular coils are

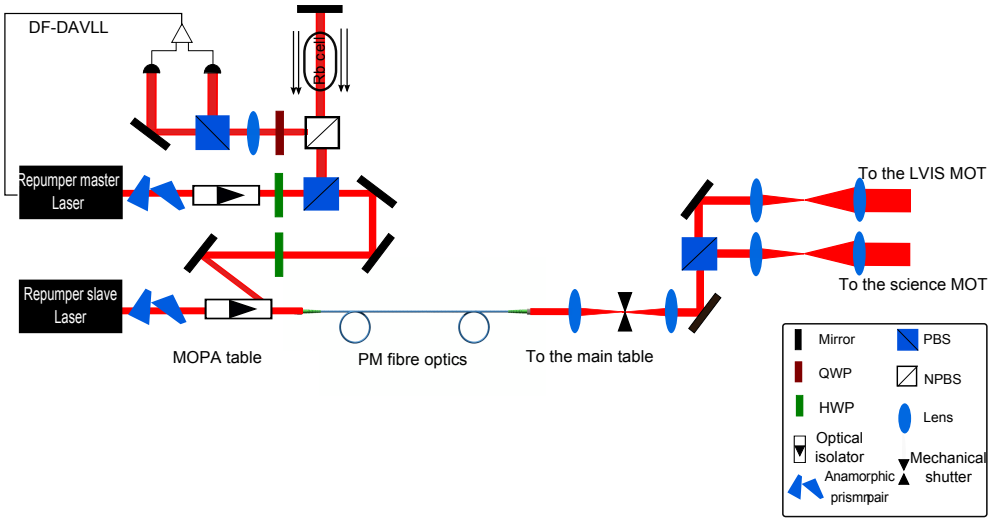

Figure 6.5: The experimental schematic for the re-pumper laser.

oriented along the same axis separated by a distance equal to the coil radius and having current flowing in opposite directions. At the point at which the magnetic fields of the two coils cancel each other, the magnetic potential has a minimum. Atoms from the magneto-optical trap can be efficiently loaded into the QUAD trap due to the common centres of the magnetic fields. However, close to the field zero, cold atoms can be ejected from the trap because the atomic magnetic moments cannot adiabatically follow the rapid change in the magnetic field direction. In other words, when the change in the magnetic field direction is faster than the Larmor frequency, the spin of the atoms cannot follow the external field. A Majorana spin-flip occurs [17, 75], which leaves the atom in an untrapped state. Therefore, it is necessary to make the change rate in the magnetic field direction smaller than the Larmor frequency to avoid Majorana transitions. In a BEC experiment, it is required to cool the atoms to very low temperatures, but this moves the atoms closer to the trap centre (B=0) and then Majorana spin-flips may take place. This atom loss channel reduces the atomic density, which is essential for achieving the evaporative cooling. Atom losses can be prevented by using a different trap configuration such as the TOP trap [75] or the so-called *Quadrupole-Ioffe trap* [21, 55].

Our method to magnetically trap the ^{87}Rb atom uses the QUIC trap [21, 55]. As shown in figure 6.7, the QUIC trap configuration consists of three coils: two quadrupole coils and one Ioffe coil. The low field seeker

atom experiences a linear optical potential, in which the quadrupole trap field increases linearly with the distance from the zero magnetic field. The atoms are then transferred into the potential of the QUIC trap, produced by turning on the Ioffe coil current. This turns the trap potential from linear into parabolic with a minimum magnetic field above zero in order to suppress Majorana spin-flip losses.
The schematic of the Ioffe coil is depicted in the upper part of figure 6.6 while the water cooling flow is shown in the lower part. The Ioffe coil has 100 turns of 0.5 mm copper wire and develops considerable heat when used. Its aluminium body (which is also used as a spacer for the quadrupole coils) is connected to the lab's water cooling system and stops the wire from burning. The maximum current used in our experiments is around 10 A which corresponds to a dissipation of about 70 W. Figure 6.8 shows the magnetic field of the quadrupole coils as a function of the displacement from the position of the trap zero. The measurements in blue data were taken with zero Ioffe current, and show a linear behaviour. The parabolic curve (black data) is obtained when switching the Ioffe current on with 2 A, thus removing the magnetic field zero. The magnetic field is measured using a magnetometer, which was calibrated so to subtract the magnetic field of the earth.

6.5 Experimental results

After setting up the experiment, data were taken to examine the behaviour of the atomic ensemble, starting with a magnetic trap life time measurement. This is followed by a description of our evaporative cooling sequence, an example of a temperature measurement and finally our first results on Bose-Einstein Condensation.

6.5.1 Magnetic trap lifetime

One of the crucial steps in our experiment is transferring the atoms from the MOT into the magnetic quadrupole trap efficiently. It is important to optimise each phase before the magnetic trap to obtain the highest atom number possible, sufficient phase space density and a maximised collision rate in the trap to ensure good evaporative cooling performance. This

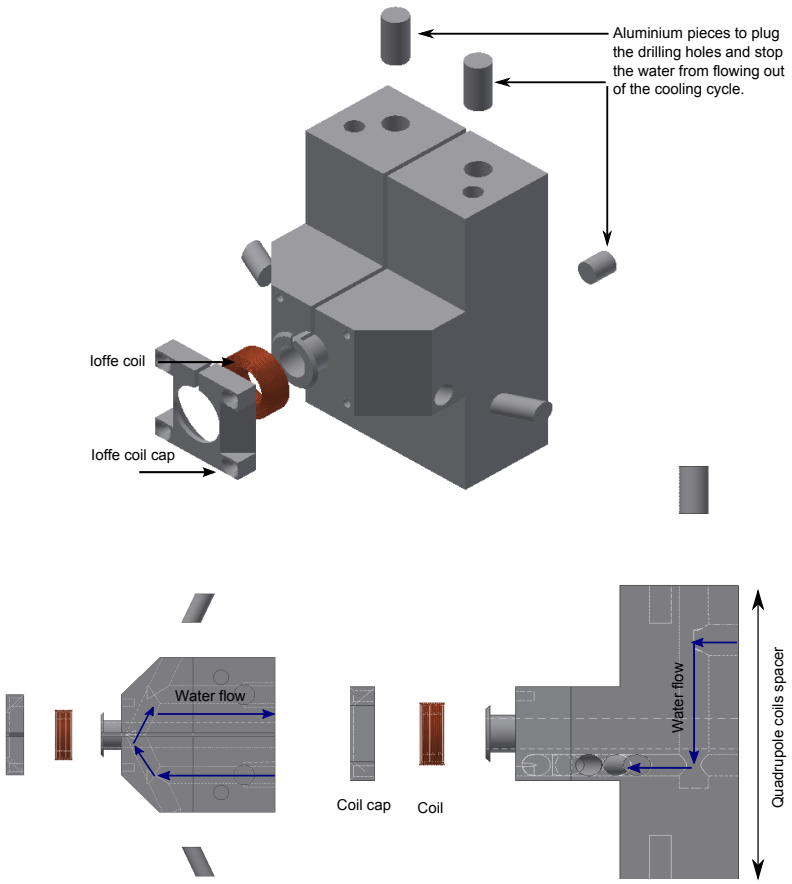

Figure 6.6: The schematic of the Ioffe coil assembly. Upper: The Ioffe coil with 100 turns is wound around a groove in the aluminium body. The cap is placed on the wire to improve the thermal conductivity to the main body of the Ioffe coil. The whole construction is slit to avoid induced eddy currents while switching the current. Lower: the side view of the Ioffe coil showing the water flow (the blue arrows) through the spacer used for cooling. Ioffe coil designed with a hole in the middle on the MOT axis to allow the imaging beam passing through the MOT. The Ioffe coil assembly was machined in the UCL workshop.

is necessary to achieve Bose-Einstein condensation. Another condition is a sufficient life time of the magnetic trap to enable the time consuming evaporation. The life time in the magnetic trap is mostly limited by collisions with hot atoms from the background gas and therefore is dependent on the vacuum conditions.

The experimental sequence shown in figure 6.9 shows how we load the magnetic quadrupole trap and determine its lifetime. First a dense and cold atomic cloud is prepared in the magneto-optical trap with a detuning of $\Delta = -1.6\,\Gamma$. In spite of the high atom number trapped in the MOT

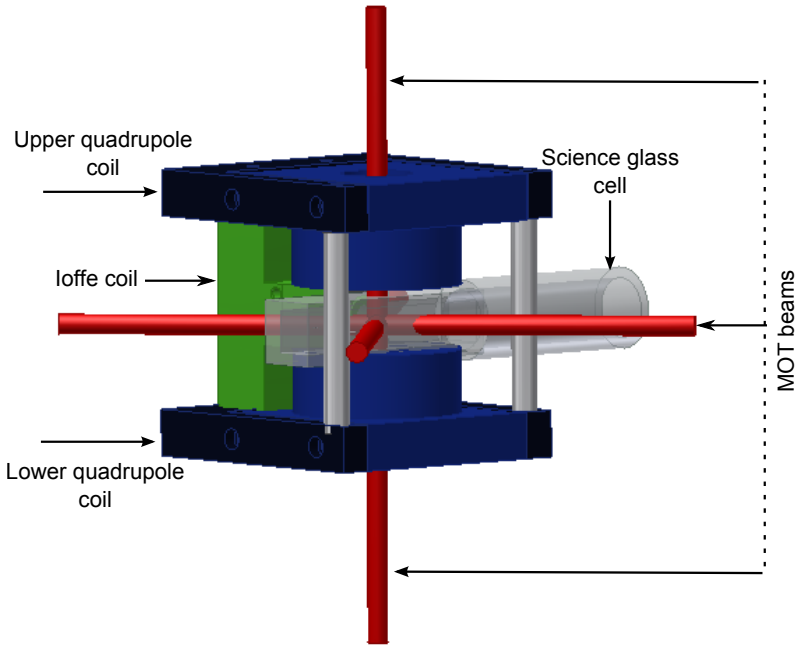

Figure 6.7: The Quadrupole-Ioffe Configuration (QUIC) consists of a pair of quadrupole magnetic coils in the anti-Helmholtz configuration with current flowing in opposite directions. The circular coils (in blue) are mounted along the same axis with a separation distance equal to the coil radius. The Ioffe coil (in green) is mounted such that the small coil is inserted close to the quadrupole trap zero while the coil body is used as a spacer for the quadrupole coils. The Ioffe coil is designed with a hole in the middle along the MOT axis to allow the imaging beam to pass through.

($\approx 2 \times 10^8$) in 3 s, the density of the atoms is not sufficient for the next phase towards the BEC (i.e. magnetic trap and evaporative cooling). A phase of compression of the MOT is therefore introduced. The LVIS beams are switched off and the trapped atoms are compressed for 50 ms [74]. This is done by doubling the magnetic field gradient from 10 G/cm to 20 G/cm to compress the trap, and increasing the laser detuning to $\Delta = -3\Gamma$. Since this phase heats the trapped atoms, an optical molasses phase is necessary to reduce the trap temperature. Therefore, the magnetic field is switched off to start a phase of optical molasses, which lasts for 10 ms at a detuning of $\Delta = -5\Gamma$. The optical molasses is optimised by balancing the intensity of the laser beams and ensuring the cloud is expanded evenly when switching off the MOT magnetic field. After the molasses phase, the atoms are distributed over all Zeeman sublevels.

For ^{87}Rb atom, there are five magnetic substates ($m_J = 0, \pm 1, \pm 2$) of

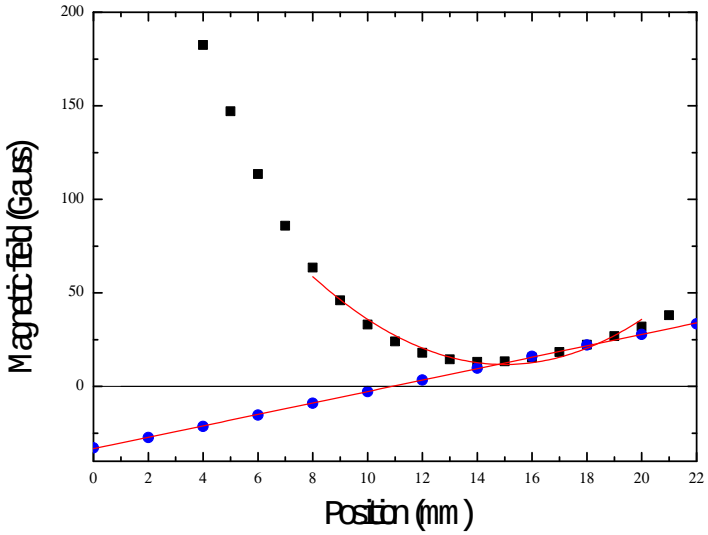

Figure 6.8: The QUIC trap coils characterisation. The blue data represent the magnetic field in Gauss as a function of the displacement from the trap centre measured by a magnetometer. The red line is the linear fit for these data. The Ioffe coil current is turned on so that the trap minimum is shifted from zero in order to avoid Majorana spin-flips. The red curve is the parabola fit to the data.

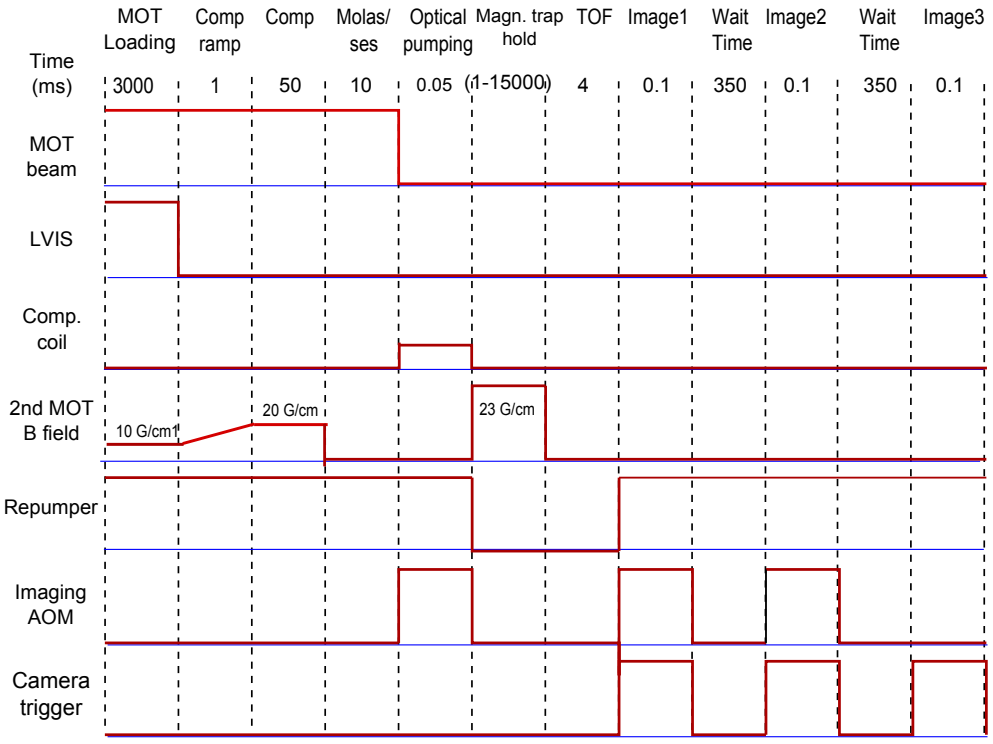

Figure 6.9: Time sequence of the magnetic trapping life time measurement.

the higher hyperfine ground state of which just two are trappable by a magnetic quadrupole trap. To increase the number of trappable atoms and thus the loading efficiency of the magnetic trap, the atoms are optically pumped into the low-field seeking $|F = 2, m_F = 2\rangle$ spin state. This is achieved by switching off the cooling beams while the imaging beam is briefly flashed on for 50 μs on resonance with the cycling transition. This mechanism is done with assistance of a small magnetic bias field (500 mG) parallel to the beam and some re-pumping light. The magnetic field is applied by increasing the current through the compensation coil pair on axis with the imaging beam. This process of optical pumping transfers the ground state population of the ^{87}Rb ensemble into the highest magnetic sublevel. 50 μs is sufficient for optical pumping since the life time of the ^{87}Rb $5^2P_{3/2}$ excited state is 26 ns [93] so that multiple optical pumping events can occur. The optical pumping mechanism enhances the number of atoms in the trap by increasing the amount of the trapped atoms to above 80%. Thus, this yields a number of atoms in the $|F = 2, m_F = 2\rangle$ state which are sufficient for the magnetic trap. After the pumping the magnetic field gradient is rapidly switched back on to trap the atoms. It is crucial that during the hold time in the magnetic trap all of the light (cooling, re-pumper and imaging beams) is switched off. This is achieved by using home built mechanical shutters to switch the beams on or off on a time scale of $\approx$2.5 ms and thus block any possible leakage through the AOMs. The hold time of the magnetic trap is then varied between 1 and 150 s in order to measure the lifetime of the atoms in the magnetic trap. After the hold time the magnetic field gradient is switched off and the cloud is left to expand freely for 4 ms to accommodate for any kind of magnetic field switching decay. Then the remaining atoms are imaged with the imaging beam. The results of a typical lifetime measurement can be seen in figure 6.10. The left graph of figure 6.10 shows the atom number in the MOT for different loading times. This graph was taken to optimise the loading of the atoms from the MOT into the magnetic trap. Longer loading times increase the atom number in the MOT but produce large fluctuations which appear in the graph as large error bars. Accordingly, the life time measurement of the magnetic trap is done with only a 3 s loading time as illustrated in the right graph of figure 6.10. This prevents the fluctuations in the ini-

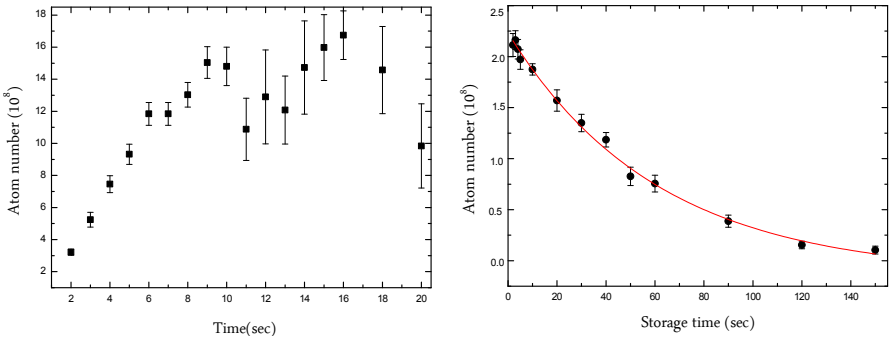

Figure 6.10: Left: The atom number in the MOT is observed with different loading times. The number of atoms is determined by the absorption imaging method (explained in 6.3.1). The data were taken to optimise the MOT loading into the magnetic trap and to determine the best loading time with less fluctuation. Larger error bars are observed for longer loading times, which are attributed to the instability of the MOT with high atom number. The loading time is chosen to be 3 s since the MOT fluctuates less here. Right: The atoms are held for different storage times in the magnetic trap. The atom number decreases exponentially with time due to the collisions with the background gas. A fit of the data reveals a lifetime of (60.8 ± 4.6) s.

tial atom number. The number of atoms in the magnetic trap decrease exponentially with the hold time. A fit of the atom number over this time revealed a lifetime of the magnetic trap of (60.8 ± 4.6) s which is sufficient for evaporative cooling and Bose-Einstein condensation. The exponential fit is expected for real atomic systems due to the trap losses mechanism. This can be attributed to the inelastic collisions. Therefore, it is related to the residual background gas in the vacuum system.

6.6 Evaporative cooling

The evaporative cooling is the final cooling stage to reach the quantum phase transition in all experiments of Bose-Einstein condensate accomplished so far. This is achieved when the atoms become indistinguishable with a separation comparable to de Broglie wavelength λ_{dB} (as defined in 6.1). The principle of the evaporative cooling is based on the idea that the high energetic and spin polarised atoms confined in a magnetic trap are removed selectively from the tail of the Maxwell-Boltzmann distribution. The remaining atoms are re-thermalised by elastic collisions re-establishing a Maxwell-Boltzmann distribution but with lower temperature and higher phase space density. For an ideal gas, the only

mechanism to remove atoms is by evaporation. Whereas, in the real case, atoms escape from the potential trap by both evaporation and undesirable inelastic collisions. Since the evaporation reduces the system's temperature, the number of atoms whose energy is larger than the truncated energy decrease. This slows down the evaporation process. Therefore, it is necessary to lower the potential depth to keep pace decreasing the atoms energy. When this cooling process is successively repeated, the hotter atoms are enforced to leave the trap reducing its temperature dramatically via the so-called *forced evaporative cooling*. In this mechanism, the RF radiation functions as an evaporative *RF-knife* lowering the depth of the confining potential. A comprehensive review on evaporative cooling was given by Ketterle and Druten [48]. The first demonstration of the RF-induced evaporative cooling of magnetically trapped atoms was reported by Pritchard in 1988 [60].

6.6.1 RF-induced evaporative

The evaporative cooling is implemented in our setup by applying radiofrequency (RF) radiation to the confined ^{87}Rb atoms in a magnetic trap. The radiofrequency ejects atoms from the trap by inducing spin-flips and thus driving transitions from the trapped state $|F = 2, m_F = 2\rangle$ into untrapped states $|F = 2, m_F = 0, -1, -2\rangle$. This turns the attractive trapping force into a repulsive force. The radiofrequency ω_{RF} is progressively reduced so that atoms with corresponding energy undergo a spin flip transition and are expelled from the trap. While, atoms with lower energy remains trapped. Figure 6.11 illustrates the schematic of the evaporative cooling with the hyperfine states of $|F = 2\rangle$.
For successful evaporative cooling, decreasing the number of atoms should be accompanied by increasing the elastic collisions rate to reach the *run-away evaporation*.

6.6.2 Experimental procedure

Experimentally, the RF radiation is generated by a four turns radio frequency antenna on axis with the quadrupole coils. The coil is positioned 1.5 cm away from the atomic sample and is directly attached to the glass

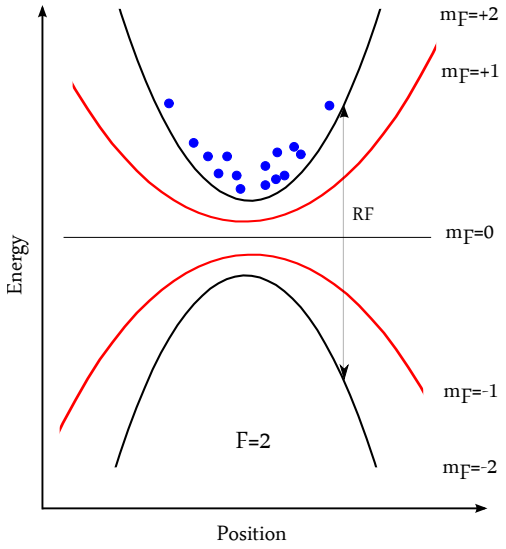

Figure 6.11: Schematic of the RF-induced evaporative cooling for ^{87}Rb atoms confined in a magnetic trap. The radiofrequency radiation drives transitions from trapped state $|F = 2, m_F = 2\rangle$ to untrapped states $|F = 2, m_F = -1\rangle$ and $|F = 2, m_F = -2\rangle$. The frequency ω_{RF} is progressively reduced so to implement the RF knife to eject the most energetic atoms in the trap.

cell. In the experiment, it is necessary to investigate the best frequency ramp which allows us to control the threshold energy and then maintain the runaway evaporation regime. This was achieved via a function generator[13]. The start and final evaporative frequencies are determined in our experiment by observing the atom number as a function of different frequencies. This suggested that the RF starts at a frequency of 30 MHz to start removing the hotter atoms. The final radiofrequency is set to be 0.45 MHz when the BEC is observed. The generated RF is swept logarithmically down in two stages [55]. First, the RF frequency is ramped down with the atoms in the quadrupole trap from the initial value of 30 MHz to 10 MHz in 5 s. Then the atoms are transferred into the QUIC trap by ramping up the QUIC current to its final value in 350 ms. The second evaporation stage happens with the atoms in the QUIC trap and lasts 13 s during which the RF is ramped logarithmically from 10.5 MHz to the final value around 0.45 MHz. It starts at a slightly higher frequency than the end frequency of the QUAD trap evaporation to accommodate for the lifted trap bottom in the QUIC trap and provide a seamless evaporation sweep. The RF frequency is optimised in term of

[13]SMT02 signal generator (5kHz-15GHz) from Rohde & Schwarz

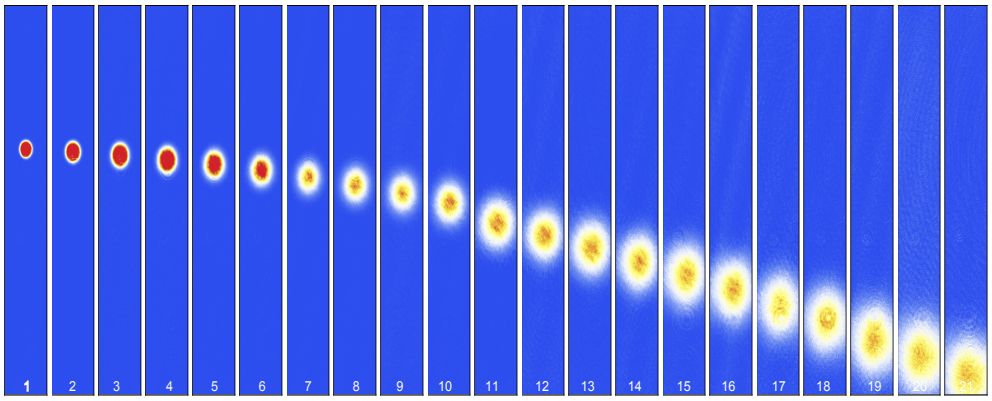

Figure 6.12: Absorption images for different times of flight of the atomic sample. The time is indicated in each image in ms. The temperature of the displayed cloud is around the recoil temperature. Clearly visible is the parabolic drop according to the acceleration under gravity as well as the expansion of the ensemble due to its Gaussian velocity distribution. In the first images the cloud is optically thick and the displayed optical density saturates. The data were taken above the phase transition.

the phase space density and the atom number so to reach the runaway evaporation regime.

6.7 Temperature measurement

The reduction of the temperature of the atomic cloud is crucial during the evaporative cooling sequence. To measure the temperature of the atomic sample we use the standard time of flight method [8]. After the cooling stages of the trapped ^{87}Rb, the magnetic field and all the laser beams are switched off so that the cloud can expand freely according to its velocity distribution and fall down under gravity. As an example of a temperature measurement, figure 6.12 shows absorption images for different times of flight between $(1 - 21)$ ms (plus an additional delay of 2 ms to account for switching delays). For each image the cloud is fitted with a 2D Gaussian to extract its width and position. The width is then plotted as a function of the expansion time. The data were fitted by a linear function to obtain the velocity of the cloud in both directions. For the particular example shown in figure 6.12 the expansion velocity was determined as $v_x = (5.98 \pm 0.08)$ mm/s and $v_y = (5.78 \pm 0.07)$ mm/s. From that, the temperature can be calculated with $T = \frac{mv^2}{k_B}$ to $T_x = (374 \pm 7)$ nK and $T_y = (350 \pm 5)$ nK, which is a temperature roughly around the recoil

temperature for ^{87}Rb ($T_r = 362\,\mathrm{nK}$). The atomic velocity distribution of this thermal ensemble is still Gaussian and its phase space density slightly above the BEC transition.

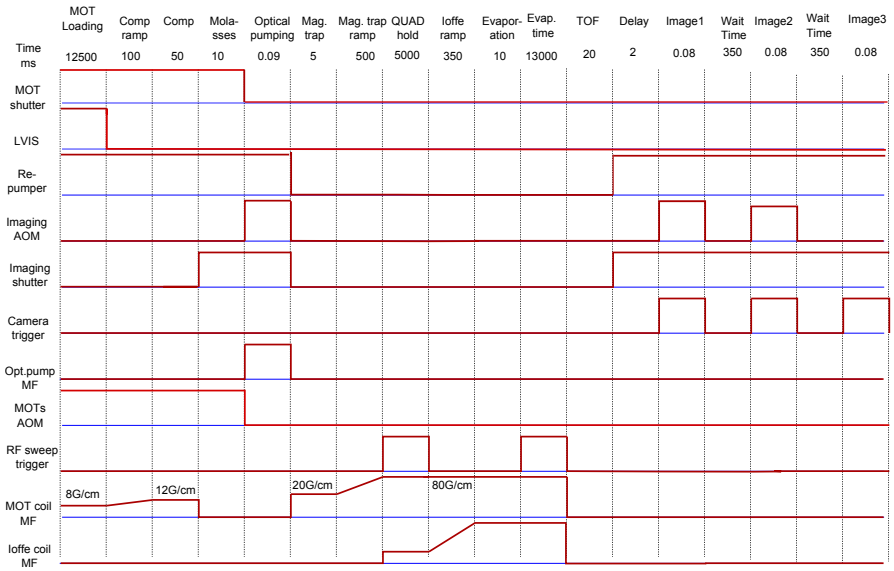

Figure 6.13: The experimental sequence for the transition to Bose-Einstein condensate.

6.8 Observation of Bose-Einstein Condensation

The phase transition to a Bose-Einstein condensation occurs when the phase space density of the ensemble, which is the product of particle density and their thermal de Broglie wavelength cubed, becomes larger than 2.612. The key factors here are temperature and atom number in our magnetic trap after the evaporation sequence. The phase space density can be increased by reducing the final radio frequency of the sweep. The experimental sequence producing a ^{87}Rb BEC in our experiment is shown in figure 6.13. The atomic condensate is observed by switching the magnetic field off to let the cloud expand ballistically over 22 ms. Then absorption images of the cloud can be used to observe the phase transition when the final evaporation frequency is reduced. Figure 6.14 shows a combined 3D plot of five successive absorption images. The same data set can be seen in figure 6.15 in a further analysis involving the

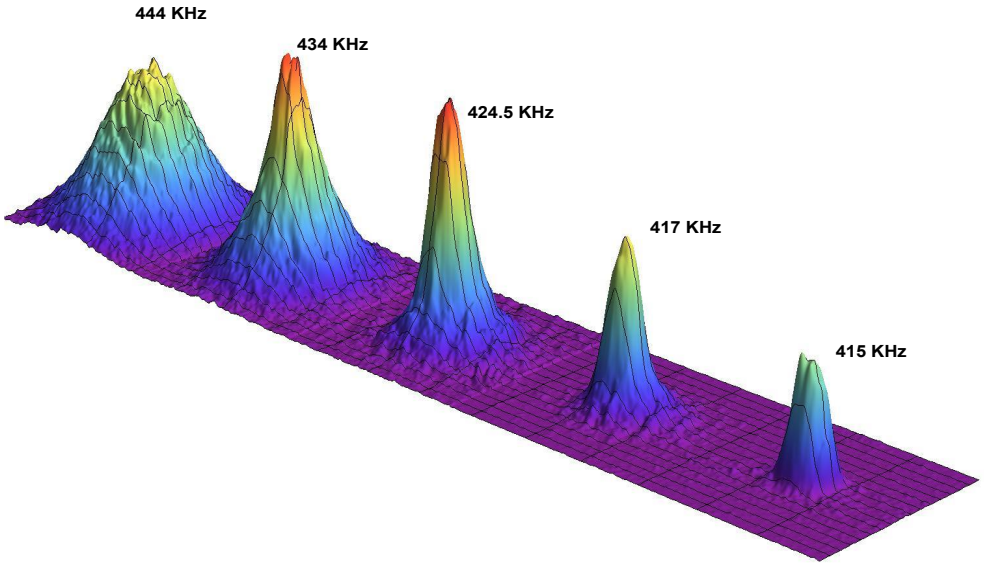

Figure 6.14: A selection of 3D plots of the optical density after 22 ms time of flight for different final evaporation frequencies. The transition from a thermal cloud of atoms, as represented by a Gaussian distribution function over a bi-modal distribution, to a pure parabolic density function of a pure BEC can be clearly seen.

profile of the cloud and its fit with the sum of a Gaussian and a parabolic function. While the first image of the set shows a thermally distributed cloud (with its Gaussian shape as an indicator of that), reducing the final radio frequency produces a fraction of the atoms in the ground state of the trap. This is the onset of Bose-Einstein condensation and the velocity distribution becomes bimodal which is a combination of a thermal and a condensate distribution. Most atoms are still thermal with a Gaussian velocity distribution, but in the centre of the distribution another part with a parabolic distribution due to the magnetic trap profile is formed. Evaporating further reduces the amount of atoms in the thermal portion and increases the BEC part until in the last image, at a frequency of 415 kHz, the distribution becomes purely parabolic and we are left with a nearly pure Bose-Einstein condensate.

6.9 Summary

This chapter illustrated our realisation of a Bose-Einstein condensate. It started with a brief introduction to the theory of BEC, and went on to describe the new laser setup including its upgrade from a diode laser into

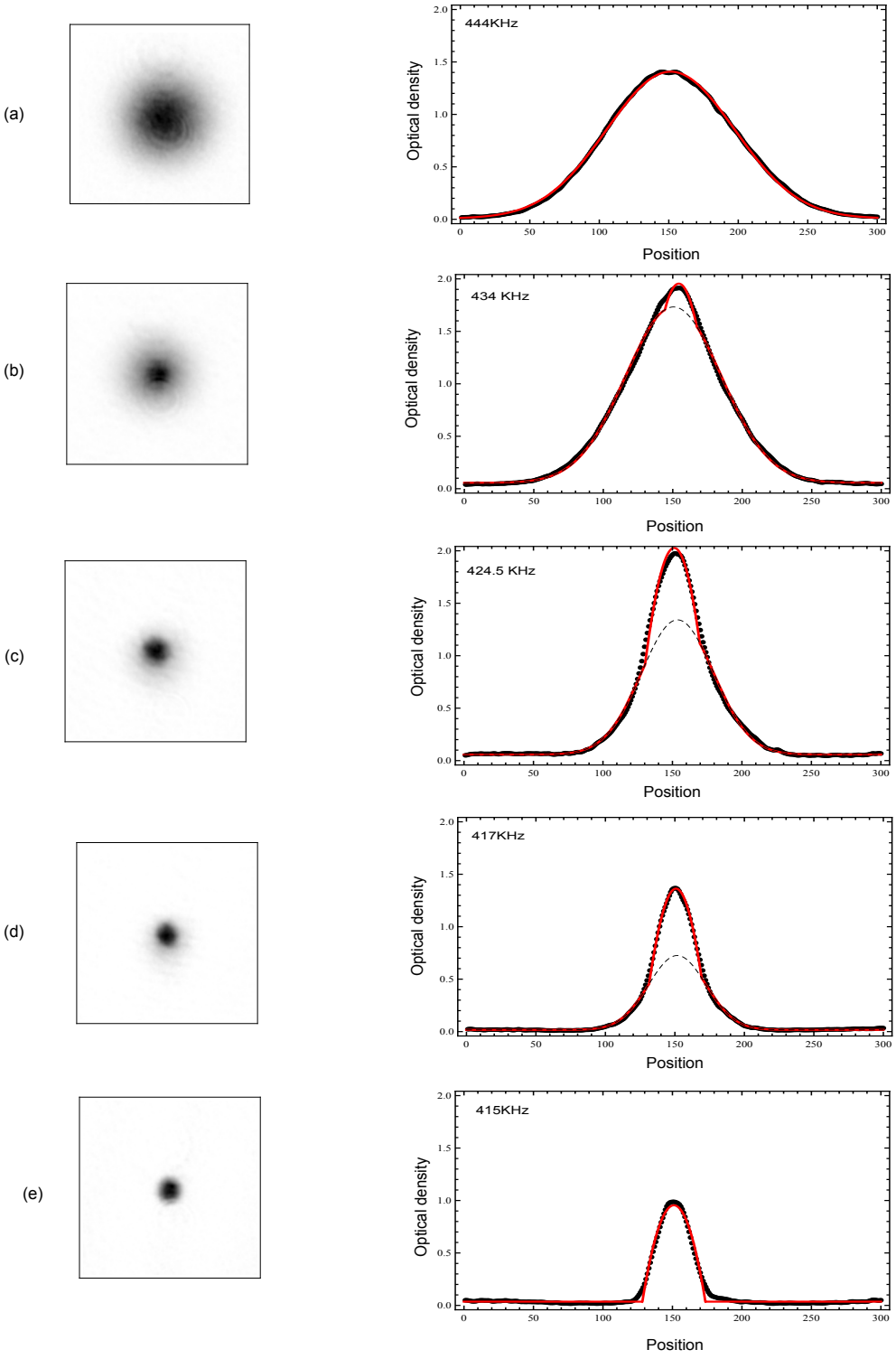

Figure 6.15: Absorption images and the corresponding density distribution of the trapped ^{87}Rb atom cloud when lowering the evaporative RF and then observing Bose-Einstein condensation. Left column: the absorption images of the atomic cloud after 20 ms expansion time. Right column: The density distribution of the trapped ^{87}Rb. (a) The cold thermal ^{87}Rb cloud fitted by a Gaussian function (the red curve). (b) The distribution is narrower than previous image. (c-d) Bi-modal distribution, which consists of two components: thermal and condensate distribution, fitted by a function which is a combination of a Gaussian function for the thermal cloud and a parabola function for the condensate. (e) Pure condensate of ^{87}Rb.

a MOPA system. This was an important step to increase the power of the cooling light to about 2 W immediately after the MOPA. Additional losses due to the shaping optics and an optical isolator limited the power coupled into an optical fibre to 800 mW, and a power of 500 mW was available after the optical fibre. Due to the observation of some long term fluctuations of the MOPA power output, the design was improved. The new design was also described in this chapter. The imaging system was also improved. This was done by using an optical fibre to transmit the imaging beam so to obtain a clean Gaussian beam profile. A new CCD camera was set up, as described in the imaging system section. The QUIC trap configuration that was used in our setup to achieve a Bose-Einstein condensate was described in the following section. After a description of the evaporative cooling sequence, data for the final cooling stage before the phase transition and an example measurement of the temperature are presented. Finally, a data set of absorption images displaying the cloud after expansion shows the transition from a thermal Gaussian velocity distribution to a parabolic one as obtained by reducing the final radio frequency of the evaporation sweep. This change in velocity distribution marks the phase transition from a thermal cloud to a pure Bose-Einstein condensate of ^{87}Rb atoms.

Chapter 7

Conclusion and Outlook

7.1 Conclusion

The field of ratchets has sparked lot of interest in the last twenty years. A remarkable number of theoretical works was followed by experimental research to understand the ratchet phenomenon. Nowadays, this field has led to many applications, such as particle separation devices and electron pumps. During my study, two ratchet experiments were conducted. The first examined an intriguing feature in a ratchet, the so-called current reversals. The second experiment investigated vibrational resonance and optical potential renormalisation. Then a number of changes were accomplished to prepare the setup for ultra-cold atom studies, which pave the way for Bose-Einstein Condensation. In this chapter, I am going to give a brief overview of the important achievements and the results obtained during my PhD study.

First, the vacuum was improved by upgrading the system apparatus from a single MOT into a double MOT system. This step provided an ultra-high vacuum below 10^{-10} mbar so to decrease the collisions with the background vapour, and obtain a sufficient vacuum environment for producing a Bose-Einstein condensate. The laser power had to be increased in order to supply both MOTs with the required power, so to increase the number of ^{87}Rb atoms in the trap. Thus, a Master Oscillator Power Amplifier system was assembled. This is an amplifier injected by a normal diode laser. The maximum output power after the amplifier is about 1.8 W. After being injected into a polarisation maintaining optical fibre,

the output power became about 500 mW. The transmitted light from the fibre was distributed for the MOTs and the imaging beam.
The first experiment on current reversals in a rocking ratchet was carried out in a driven dissipative optical lattice. This was done by observing the atomic current as a function of the driving frequency for different force strengths. This work generalised the previous study by our group concerning the link between current reversals and symmetry-breaking mechanisms. Since only the weakly damped regime can be accessed experimentally, the Hamiltonian and overdamped regimes were investigated numerically by our collaborator David Cubero.
The second experiment investigated the vibrational resonance phenomenon in dissipative optical lattices. The experimental scheme was implemented by applying a high frequency field, whose frequency is larger than any other frequency in the system. The experiment demonstrated the possibility of controlling the optical potential depth. These results can be applied to any system (e.g. solid state system) consisting of particles in a periodic potential. Two detection methods were used to probe the potential renormalisation: observation of directed transport and measurement of diffusion properties.
In the last experiment, we produced a Bose-Einstein condensate by RF evaporation in a QUIC trap. The trap life time in the magnetic trap was optimised and measured to be about 60 s. Then, atoms in the trap were cooled by ramping the radio frequency down. Bose-Einstein condensation was observed.

7.2 Outlook

Producing a Bose-Einstein condensate in a dipole trap is the next step of the experiment. The dipole trap will be created with a fibre amplifier which is designed to operate in combination with a narrow linewidth seed laser. The amplifier produces a maximum of 50 W power at a wavelength of 1064 nm. The system is then set out to study transport phenomena in optical lattices, such as the ratchet effect. But, in contrast to the work presented in this thesis, it will be in a Hamiltonian regime using a macroscopic quantum system, instead of thermal atoms in a dissipative

optical lattice.

Bibliography

[1] M. H. Anderson, J. R. Ensher, M. R. Matthews, C. E. Wieman, and E. A. Cornell. Observation of Bose-Einstein condensation in a dilute atomic vapor. *Science*, pages 198–201, 1995.

[2] V. S. Bagnato, G. P. Lafyatis, A. G. Martin, E. L. Raab, R. N. Ahmad-Bitar, and D. E. Pritchard. Continuous stopping and trapping of neutral atoms. *Phys. Rev. Lett.*, 58:2194–2197, May 1987.

[3] M. Barbi and M. Salerno. Phase locking effect and current reversals in deterministic underdamped ratchets. *Phys. Rev. E*, 62:1988–1994, Aug 2000.

[4] R. Bartussek, P. Hänggi, and J. G. Kissner. Periodically Rocked Thermal Ratchets. *Europhys. Lett.*, 28:459–464, Dec. 1994.

[5] J. E. Bjorkholm, R. R. Freeman, A. Ashkin, and D. B. Pearson. Observation of focusing of neutral atoms by the dipole forces of resonance-radiation pressure. *Phys. Rev. Lett.*, 41:1361–1364, Nov 1978.

[6] C. C. Bradley, C. A. Sackett, and R. G. Hulet. Bose-einstein condensation of lithium: Observation of limited condensate number. *Phys. Rev. Lett.*, 78:985–989, Feb 1997.

[7] C. C. Bradley, C. A. Sackett, J. J. Tollett, and R. G. Hulet. Evidence of Bose-Einstein condensation in an atomic gas with attractive interactions. *Phys. Rev. Lett.*, 75:1687–1690, Aug 1995.

[8] T. M. Brzozowski, M. Maczynska, M. Zawada, J. Zachorowski, and W. Gawlik. Time-of-flight measurement of the temperature of cold

atoms for short trap-probe beam distances. *J. Opt. B: Quantum Semiclass. Opt.*, 4(1):62, 2002.

[9] J. Casado-Pascual. Effect of a high-frequency magnetic field on the resonant behaviour displayed by a spin-1/2 particle under the influence of a rotating magnetic field. *Chem. Phys.*, 375(23):170 – 179, 2010.

[10] Y. Castin and J. Dalibard. Quantization of atomic motion in optical molasses. *Europhys. Lett.*, 14(8):761, 1991.

[11] V. N. Chizhevsky, E. Smeu, and G. Giacomelli. Experimental evidence of vibrational resonance in an optical system. *Phys. Rev. Lett.*, 91:220602, Nov 2003.

[12] S. Chu, J. E. Bjorkholm, A. Ashkin, and A. Cable. Experimental observation of optically trapped atoms. *Phys. Rev. Lett.*, 57:314–318, July 1986.

[13] S. Chu, L. Hollberg, J. E. Bjorkholm, A. Cable, and A. Ashkin. Three-dimensional viscous confinement and cooling of atoms by resonance radiation pressure. *Phys. Rev. Lett.*, 55:48–51, Jul 1985.

[14] D. Cubero, V. Lebedev, and F. Renzoni. Current reversals in a rocking ratchet: Dynamical versus symmetry-breaking mechanisms. *Phys. Rev. E*, 82:041116, Oct 2010.

[15] J. Dalibard and C. Cohen-Tannoudji. Laser cooling below the doppler limit by polarization gradients: simple theoretical models. *J. Opt. Soc. Am. B*, 6(11):2023–2045, Nov 1989.

[16] K. Davis, M.-O. Mewes, and W. Ketterle. An analytical model for evaporative cooling of atoms. *App. Phys. B*, 60(2-3):155–159, 1995.

[17] K. B. Davis, M.-O. Mewes, M. A. Joffe, M. R. Andrews, and W. Ketterle. Evaporative cooling of sodium atoms. *Phys. Rev. Lett.*, 74:5202–5205, Jun 1995.

[18] S. Denisov and S. Flach. Symmetries and transport with quasiperiodic driving. *Acta Physica Polonica B*, 35:1437, Jan 2004.

[19] S. Denisov, S. Flach, A. Ovchinnikov, O. Yevtushenko, and Y. Zolotaryuk. Broken space-time symmetries and mechanisms of rectification of ac fields by nonlinear (non)adiabatic response. *Phys. Rev. E*, 66:041104, 2002.

[20] P. J. Douglas. *Atomic dynamics in optical traps: experiments with caesium atoms*. PhD thesis, University College London, 2009.

[21] T. Esslinger, I. Bloch, and T. W. Hänsch. Bose-Einstein condensation in a quadrupole-ioffe-configuration trap. *Phys. Rev. A*, 58:R2664–R2667, Oct 1998.

[22] R. Feynman, R. Leighton, and M. Sands. *The Feynman Lectures on Physics: Mainly mechanics, radiation, and heat*. Addison-Wesley world student series. Addison-Wesley, 1963.

[23] S. Flach, O. Yevtushenko, and Y. Zolotaryuk. Directed current due to broken time-space symmetry. *Phys. Rev. Lett.*, 84:2358–2361, Mar 2000.

[24] C. J. Foot. *Atomic Physics*. Oxford University Press, Oxford, 2009.

[25] R. Gommers. *Symmetry and transport in cold atom ratchets*. PhD thesis, University College London, 2007.

[26] R. Gommers, S. Bergamini, and F. Renzoni. Dissipation-induced symmetry breaking in a driven optical lattice. *Phys. Rev. Lett.*, 95:073003, Aug 2005.

[27] R. Gommers, S. Denisov, and F. Renzoni. Quasiperiodically driven ratchets for cold atoms. *Phys. Rev. Lett.*, 96:240604, Jun 2006.

[28] R. Gommers, P. Douglas, S. Bergamini, M. Goonasekera, P. H. Jones, and F. Renzoni. Resonant activation in a nonadiabatically driven optical lattice. *Phys. Rev. Lett.*, 94:143001, Apr 2005.

[29] R. Gommers, V. Lebedev, M. Brown, and F. Renzoni. Gating ratchet for cold atoms. *Phys. Rev. Lett.*, 100:040603, Jan 2008.

[30] R. Grimm, M. Weidemüller, and Y. B. Ovchinnikov. Optical dipole traps for neutral atoms. volume 42 of *Adv. At. Mol. Opt. Phys.*, pages 95 – 170. Academic Press, 2000.

[31] G. Grynberg and C. Robilliard. Cold atoms in dissipative optical lattices. *phys. Rep.*, 355:335–451, Dec. 2001.

[32] L. Guidoni and P. Verkerk. Optical lattices: cold atoms ordered by light. *J. Opt. B: Quantum Semiclass. Opt.*, 1(5):R23, 1999.

[33] D. T. Haar. *Collected papers of P.L. Kapitza: Pendulum with a vibrating suspension.* Pergamon, 1965.

[34] H. Hagman, C. M. Dion, P. Sjölund, S. J. H. Petra, and A. Kastberg. Influence of the lattice topography on a three-dimensional, controllable Brownian motor. *Europhys. Lett.*, 81:33001, Feb. 2008.

[35] P. Hänggi and F. Marchesoni. Artificial brownian motors: Controlling transport on the nanoscale. *Rev. Mod. Phys.*, 81:387–442, Mar 2009.

[36] T. W. Hänsch and A. L. Schawlow. Cooling of gases by laser radiation. *Opt. Commun.*, 13:68, Jan. 1975.

[37] H. F. Hess. Evaporative cooling of magnetically trapped and compressed spin-polarized hydrogen. *Phys. Rev. B*, 34:3476–3479, Sep 1986.

[38] H. F. Hess, G. P. Kochanski, J. M. Doyle, N. Masuhara, D. Kleppner, and T. J. Greytak. Magnetic trapping of spin-polarized atomic hydrogen. *Phys. Rev. Lett.*, 59:672–675, Aug 1987.

[39] T. W. Hodapp, C. Gerz, C. Furtlehner, C. I. Westbrook, W. D. Phillips, and J. Dalibard. Three-dimensional spatial diffusion in optical molasses. *App. Phys. B: Laser and optics*, 60:135–143, 1995. 10.1007/BF01135855.

[40] J. A. Hołyst and W. Wojciechowski. The effect of Kapitza pendulum and price equilibrium. *Physica A: Statistical Mechanics and its Applications*, 324(12):388 – 395, 2003. Proceedings of the International Econophysics Conference.

[41] P. S. Jessen, C. Gerz, P. D. Lett, W. D. Phillips, S. L. Rolston, R. J. C. Spreeuw, and C. I. Westbrook. Observation of quantized

motion of Rb atoms in an optical field. *Phys. Rev. Lett.*, 69:49–52, Jul 1992.

[42] P. H. Jones, M. Goonasekera, and F. Renzoni. Rectifying fluctuations in an optical lattice. *Phys. Rev. Lett.*, 93:073904, Aug 2004.

[43] P. Jung, J. G. Kissner, and P. Hänggi. Regular and Chaotic Transport in Asymmetric Periodic Potentials: Inertia Ratchets. *Phys. Rev. Lett.*, 76:3436–3439, Apr. 1996.

[44] K. I. Petsas, G. Grynberg, and J.-Y. Courtois. Semiclassical monte carlo approaches for realistic atoms in optical lattices. *Eur. Phys. J. D*, 6(1):29–47, 1999.

[45] H. Katori, S. Schlipf, and H. Walther. Anomalous dynamics of a single ion in an optical lattice. *Phys. Rev. Lett.*, 79:2221–2224, Sep 1997.

[46] A. Kenfack, S. M. Sweetnam, and A. K. Pattanayak. Bifurcations and sudden current change in ensembles of classically chaotic ratchets. *Phys. Rev. E*, 75:056215, May 2007.

[47] W. Ketterle. Nobel lecture: When atoms behave as waves: Bose-Einstein condensation and the atom laser. *Rev. Mod. Phys.*, 74:1131–1151, Nov 2002.

[48] W. Ketterle and N. van Druten. Evaporative cooling of trapped atoms. *Adv. At. Mol. Opt. Phys.*, 37:181–236, 1996.

[49] P. S. Landa and P. V. E. McClintock. Vibrational resonance. *J. Phys. A: Mathematical and General*, 33(45):L433, 2000.

[50] P. Lebedev. Untersuchungen über die Druckkräfte des Lichtes. *Annalen der Physik*, 311(11):433–458, 1901.

[51] V. Lebedev. *AC driven ratchets for cold atoms: beyond 1D rocking ratchets*. PhD thesis, University College London, 2010.

[52] V. S. Letokhov. *Laser control of atoms and molecules*. Oxford University press, New York, 2007.

[53] P. D. Lett, R. N. Watts, C. I. Westbrook, W. D. Phillips, P. L. Gould, and H. J. Metcalf. Observation of atoms laser cooled below the doppler limit. *Phys. Rev. Lett.*, 61:169–172, Jul 1988.

[54] R. Loudon. *The quantum theory of light*. Clarendon Press, Oxford, 1973.

[55] B. Lu and W. A. van Wijngaarden. Bose-Einstein condensation in a quic trap. *Can. J. Phys.*, 82:81–102, 2004.

[56] Z. T. Lu, K. L. Corwin, M. J. Renn, M. H. Anderson, E. A. Cornell, and C. E. Wieman. Low-velocity intense source of atoms from a magneto-optical trap. *Phys. Rev. Lett.*, 77:3331–3334, Oct 1996.

[57] M. O. Magnasco. Forced thermal ratchets. *Phys. Rev. Lett.*, 71:1477–1481, Sep 1993.

[58] F. Marchesoni. Harmonic mixing signal: Doubly dithered ring laser gyroscope. *Phys. Lett. A*, 119:221–224, Dec. 1986.

[59] S. Marksteiner, K. Ellinger, and P. Zoller. Anomalous diffusion and Lévy walks in optical lattices. *Phys. Rev. A*, 53:3409–3430, May 1996.

[60] A. G. Martin, K. Helmerson, V. S. Bagnato, G. P. Lafyatis, and D. E. Pritchard. RF spectroscopy of trapped neutral atoms. *Phys. Rev. Lett.*, 61:2431–2434, Nov 1988.

[61] J. L. Mateos. Chaotic transport and current reversal in deterministic ratchets. *Phys. Rev. Lett.*, 84:258–261, Jan 2000.

[62] J. C. Maxwell. *A treatise on electricity and magnetism*. Clarendon Press, Oxford, 1873.

[63] D. R. Meacher. Optical lattices-crystalline structures bound by light. *Contem. Phys.*, 39:329–350, May 1998.

[64] C. Mennerat-Robilliard, D. Lucas, S. Guibal, J. Tabosa, C. Jurczak, J.-Y. Courtois, and G. Grynberg. Ratchet for cold rubidium atoms: The asymmetric optical lattice. *Phys. Rev. Lett.*, 82:851–854, Jan 1999.

[65] H. J. Metcalf and P. van der Straten. *Laser cooling and trapping*. Springer Verlag, New York, 1999.

[66] A. L. Migdall, J. V. Prodan, W. D. Phillips, T. H. Bergeman, and H. J. Metcalf. First observation of magnetically trapped neutral atoms. *Phys. Rev. Lett.*, 54:2596–2599, Jun 1985.

[67] A. Millett-Sikking, I. G. Hughes, P. Tierney, and S. L. Cornish. Davll lineshapes in atomic rubidium. *J. Phys. B: At. Mol. Opt. Phys.*, 40(1):187, 2007.

[68] H. Müller. Fast high-voltage amplifiers for driving electro-optic modulators. *Review of Scientific Instruments*, 76(8):084701, 2005.

[69] W. Neuhauser, M. Hohenstatt, and P. Toschek. Optical-sideband cooling of visible atom cloud confined in parabolic well. *Phys. Rev. Lett.*, 41:233–237, Jul 1978.

[70] E. F. Nichols and G. F. Hull. A preliminary communication on the pressure of heat and light radiation. *Phys. Rev. (Series I)*, 13:307–320, Nov 1901.

[71] L. A. Orozco. Laser cooling and trapping of neutral atoms. *AIP Conference Proceedings*, 464(1):67–90, 1999.

[72] T. Petelski, M. Fattori, G. Lamporesi, J. Stuhler, and G. M. Tino. Doppler-free spectroscopy using magnetically induced dichroism of atomic vapor: a new scheme for laser frequency locking. *Eur. Phys. J. D - At. Mol. Opt. Plas. Phys.*, 22(2):279–283, Feb. 2003.

[73] C. J. Pethick and H. Smith. *Bose-Einstein Condensation in dilute gases*. Cambridge university press, Cambridge, 2004.

[74] W. Petrich, M. H. Anderson, J. R. Ensher, and E. A. Cornell. Behavior of atoms in a compressed magneto-optical trap. *J. Opt. Soc. Am. B*, 11(8):1332–1335, Aug 1994.

[75] W. Petrich, M. H. Anderson, J. R. Ensher, and E. A. Cornell. Stable, tightly confining magnetic trap for evaporative cooling of neutral atoms. *Phys. Rev. Lett.*, 74:3352–3355, Apr 1995.

[76] W. D. Phillips. Nobel lecture: Laser cooling and trapping of neutral atoms. *Rev. Mod. Phys.*, 70:721–741, Jul 1998.

[77] W. D. Phillips, P. L. Gould, and P. D. Lett. Cooling, stopping, and trapping atoms. *Science*, 239(4842):877–883, 1988.

[78] P. Phoonthong. *State-Insensitive Traps for Caesium Atoms.* PhD thesis, University College London, 2011.

[79] J.-L. Picqué and J.-L. Vialle. Atomic-beam deflection and broadening by recoils due to photon absorption or emission. *Opt. Commun.*, 5:402–406, Aug. 1972.

[80] N. R. Quintero, J. A. Cuesta, and R. Alvarez-Nodarse. Symmetries shape the current in ratchets induced by a biharmonic driving force. *Phys. Rev. E*, 81:030102, Mar 2010.

[81] E. Raab, M. Prentiss, A. Cable, S. Chu, and D. Pritchard. Trapping of neutral sodium atoms with radiation pressure. *Phys. Rev. Lett.*, 59:2632–2634, Jul 1987.

[82] P. Reimann. Supersymmetric Ratchets. *Phys. Rev. Lett.*, 86:4992–4995, May 2001.

[83] P. Reimann. Brownian motors: noisy transport far from equilibrium. *Phys. Rep.*, 361(24):57 – 265, 2002.

[84] P. Reimann, M. Grifoni, and P. Hänggi. Quantum ratchets. *Phys. Rev. Lett.*, 79:10–13, Jul 1997.

[85] L. Ricci, M. Weidemüller, T. Esslinger, A. Hemmerich, C. Zimmermann, V. Vuletić, W. König, and T. W. Hänsch. A compact grating-stabilized diode laser system for atomic physics. *Opt. Commun.*, 117(5-6):541 – 549, 1995.

[86] Rousselet J, Salome L, Ajdari A, Prost J. Directional motion of Brownian particles induced by a periodic asymmetric potential. *Nature*, 370:446–448, Aug 1994.

[87] C. Salomon, J. Dalibard, A. Aspect, H. Metcalf, and C. Cohen-noudji. Channeling atoms in a laser standing wave. *Phys. Rev. Lett.*, 59:1659–1662, Oct 1987.

[88] M. Schiavoni, L. Sanchez-Palencia, F. Renzoni, and G. Grynberg. Phase control of directed diffusion in a symmetric optical lattice. *Phys. Rev. Lett.*, 90:094101, Mar 2003.

[89] R. Schieder, H. Walther, and L. Wöste. Atomic beam deflection by the light of a tunable dye laser. *Opt. Commun.*, 5:337–340, Aug. 1972.

[90] J. Schoser, A. Batär, R. Löw, V. Schweikhard, A. Grabowski, Y. B. Ovchinnikov, and T. Pfau. Intense source of cold Rb atoms from a pure two-dimensional magneto-optical trap. *Phys. Rev. A*, 66:023410, Aug 2002.

[91] P. Sjölund, S. J. H. Petra, C. M. Dion, H. Hagman, S. Jonsell, and A. Kastberg. Characterisation of a three-dimensional Brownian motor in optical lattices. *Eur. Phys. J. D*, 44:381–388, Aug. 2007.

[92] A. M. Steane, M. Chowdhury, and C. J. Foot. Radiation force in the magneto-optical trap. *J. Opt. Soc. Am. B*, 9(12):2142–2158, Dec 1992.

[93] D. A. Steck. Rubidium 87 D line data. *available online at http://steck.us/alkalidata*, revision 2.0.1, May 2008.

[94] P. J. Ungar, D. S. Weiss, E. Riis, and S. Chu. Optical molasses and multilevel atoms: theory. *J. Opt. Soc. Am. B*, 6(11):2058–2071, Nov 1989.

[95] V. Serreli, C.-F. Lee, E. R. Kay, D. A. Leigh. A molecular information ratchet. *Nature*, 445:523–527, Feb 2007.

[96] R. van Roijen, J. J. Berkhout, S. Jaakkola, and J. T. M. Walraven. Experiments with atomic hydrogen in a magnetic trapping field. *Phys. Rev. Lett.*, 61:931–934, Aug 1988.

[97] A. Wickenbrock, D. Cubero, N. A. A. Wahab, P. Phoonthong, and F. Renzoni. Current reversals in a rocking ratchet: The frequency domain. *Phys. Rev. E*, 84:021127, Aug 2011.

[98] A. Wickenbrock, P. C. Holz, N. A. A. Wahab, P. Phoonthong, D. Cubero, and F. Renzoni. Vibrational mechanics in an optical

lattice: Controlling transport via potential renormalization. *Phys. Rev. Lett.*, 108:020603, Jan 2012.

[99] C. E. Wieman and L. Hollberg. Using diode lasers for atomic physics. *Review of Scientific Instruments*, 62(1):1–20, 1991.

[100] D. J. Wineland, R. E. Drullinger, and F. L. Walls. Radiation-pressure cooling of bound resonant absorbers. *Phys. Rev. Lett.*, 40:1639–1642, Jun 1978.

[101] W. Wing. On neutral particle trapping in quasistatic electromagnetic fields. *Progress in Quantum Electronics*, 8:181–199, 1984.

[102] W. Wonneberger. Harmonic mixing in the classical charge density wave model above threshold. *Zeitschrift für Physik B Condensed Matter*, 53(3):167–173, 1983.

[103] C. Ye. *Tunable External Cavity Diode Lasers*. World scientific Publishing Co. Pte. Ltd., Singapore, 2004.

[104] S. M. Yihan Xiong and J.L.Carlsten. Design and characteristics of tapered amplifier diode system by seeding with continuous-wave and mode-locked external cavity diode laser. *Opt. Eng*, 45:124205, 2006.